Three-Dimensional Porous Scaffolds for Bone Tissue Engineering and Cancer Research Applications

Stephen J. Florczyk

A dissertation
submitted in partial fulfillment of the
requirements for the degree of

Doctor of Philosophy

University of Washington
2012

Miqin Zhang, Chair
Rajendra Bordia
Brian Flinn

Program Authorized to Offer Degree:
Materials Science and Engineering

University of Washington

Abstract

Three-Dimensional Porous Scaffolds for Bone Tissue Engineering and Cancer Research Applications

Stephen J. Florczyk

Chair of the Supervisory Committee:
Professor Miqin Zhang
Materials Science and Engineering

Tissue engineering constructs (TEC) are comprised of cells, porous biomaterial scaffold, and growth factors to regenerate tissues. The biomaterial scaffold is an essential component of a TEC, substituting for extracellular matrix (ECM), allowing cell adhesion, and providing mechanical support. The drawbacks of scaffolds for tissue engineering include lack of resemblance to the native ECM, lack of mechanical properties, and poor cell delivery and distribution.

This dissertation presents the preparation and evaluation of three-dimensional (3D) porous biomaterial scaffolds for bone tissue engineering (BTE) applications. The use of alginate gel to enhance cell seeding of ceramic scaffolds was demonstrated. The alginate gel-seeded constructs had increased cell populations *in vitro* and enhanced osteogenesis *in vivo* compared to conventionally seeded samples. The processing of 3D porous chitosan–alginate (CA) scaffolds was examined by varying processing parameters. Solution viscosity had the greatest effect on pore morphology, and scaffolds with uniform pore morphology had the greatest compressive strength and osteoblast proliferation. Through process control, CA scaffolds of differing polymer concentration and pore size were prepared and evaluated with mechanical testing and osteoblast culture. These tests confirmed that the 4 wt% CA scaffolds provided the best combination of pore size and mechanical properties for BTE. The 3D porous CA scaffolds were evaluated in rat

calvarial defects for bone regeneration with different treatments and compared to untreated control defects. After 16 weeks, the CA scaffold samples all showed greater bone regeneration than did the control.

Additionally, CA scaffolds were investigated for cancer research applications. Tissue engineering approaches recently have been applied to cancer research. 3D cultures better recreate the native tumor microenvironment than do 2D tissue culture plates, which are predominantly used for cancer research. 3D porous CA scaffolds were evaluated for enrichment of cancer stem cell population of human glioblastoma cells and demonstrated greater enrichment than did control samples. 3D porous CA scaffolds were also evaluated for use as an *in vitro* platform for co-culturing prostate cancer cells with immune cells. The CA scaffolds demonstrated potential for *in vitro* testing of immunotherapies. The 3D porous CA scaffolds provide a good 3D environment for tissue engineering and cancer applications.

TABLE OF CONTENTS

Page

LIST OF FIGURES

Figure **Page**

LIST OF TABLES

Table Number **Page**

ACKNOWLEDGMENTS

I would like to thank God for the opportunity to work with everyone I have interacted with during my degree. I look forward to the rest of my journey.

I would like to thank my advisor, Miqin Zhang, for the opportunity to work in her research group and the guidance on the research projects. I have learned a lot and developed new skills during my time here. I would also like to thank my committee members, Rajendra Bordia, Brian Flinn, Richard Hopper, and Timothy Cox, for taking time to review my graduate work. Additionally, I would like to thank our collaborators, Richard Hopper, Jerry Huang, John Silber, Jennifer Wu, and Jim Park, who provided assistance with the research.

I would like to thank my colleagues in the Zhang Lab, especially Forrest Kievit, for their assistance with the work and the camaraderie during my time here. I would also like to thank the undergraduate students I have worked with during my degree.

I would like to thank the MSE department staff, especially Kathy Elkins and Bichtien Thach. I would also like to thank the lab managers who have assisted me in conducting different analyses, including Greg Martin, Stephanie Lara, Michele Black, and Wai Pang Chan.

I would like to thank my parents, Gary and Lorraine Florczyk, and my in-laws, Warren and Patty Goodnow, for their support during my degree. I would especially like to thank my wife, Sara Florczyk, for her love and support during my degree. She put up with me working long hours, gave me many rides to and from school, and made many meals for me.

I would like to acknowledge funding I received from the Egtvedt fellowship, which helped support this work. I would also like to acknowledge other funding sources, including Seattle Children's Hospital, University of Washington Technology Gap Innovation Fund (TGIF), NIH grants (R01CA134213, R01EB006043, T32CA138312), and NSF.

1. Introduction

As the population of the United States continues to age, medical issues become more prevalent and include the need for organ transplants, joint replacements, reconstruction of damaged tissues, and other treatments. The 2010 United States Census indicated that the population of Americans age 65 and over was 40.3 million and growing at a faster rate (15.1 percent) than the population under age 45 [1, 2]. The share of the overall United States population that is age 65 and over has increased steadily during the twentieth century, from 4.1 percent of the total population in 1900 to 13.0 percent in 2010 [2]. End-stage organ failure is a growing issue due to the aging population and requires organ transplantation, but the supply of available transplants is very limited. Even when transplants are available, they require the patient to remain on immunosuppressive therapy to prevent organ rejection [3–5]. Additionally, trauma will affect patients from this and other age ranges, requiring tissue replacement or reconstruction. Furthermore, patients may be afflicted by cancer. Cancer is the second leading cause of death in the United States behind heart disease, based on data from 2007 [6]. Additionally, estimated values for 2010 projected 1,529,560 new cases diagnosed and 569,490 deaths among all types of cancer [6]. The combination of an aging population and the incidence of cancer increase the burden on the medical system, requiring additional support from biomedical engineers and biomaterials.

Significant advances in medicine during the twentieth century have been attained through advances in surgical techniques and availability of improved technology including biomaterials. The use of biomaterials has long been part of human existence; sutures, which date back 32,000 years, are an example, as are dental implants [7, 8]. World War II stimulated the development of high-performance metals, ceramics, and polymers, which led to further advances in medical technology when they became available following the war [7]. Hip and knee prostheses, dental implants, intraocular lenses, vascular grafts, and other biomedical devices used the newly developed materials [7, 8]. These advances in materials and their further development, combined with advances in understanding of biology, have lead to the current biomaterials and biomedical devices.

While the use of biomaterials previously has focused on structural or functional support or incorporation into a biomedical device, the advent of tissue engineering allows the potential for more sophisticated treatments. Tissue engineering uses the advances in biomaterials and biology to prepare treatments that combine biomaterial scaffolds with biological factors, including cells and growth factors, selected for repair of the target tissue [9]. Despite the nearly two decades of research and great promise of tissue engineering, it has yet to deliver widely available clinical success. Some current clinical tissue engineering successes include tissue-engineered trachea and bladder [4, 5, 10]. The main drawbacks of tissue engineering include the inability of biomaterial scaffolds to match the mechanical properties and hierarchical structure of the native tissue and resemble the native extracellular matrix (ECM). These drawbacks prevent the replication of the native three-dimensional (3D) tissue environment. The tissue-engineered trachea and bladder have used decellularized allogenous grafts, which provide the exact tissue structure, but have disadvantages such as the need for collection and processing (decellularizing) of grafts, potential immunogenicity, and seeding cells with correct distribution. Despite the lack of widely available clinical successes, tissue engineering remains a continuously growing research area that combines engineering, biology, and medicine. Furthermore, the practices and materials developed for tissue engineering can be applied to cancer research to improve treatments for cancer patients [11].

This dissertation documents the use of 3D porous scaffolds for bone tissue engineering and cancer research applications. The research showed the use of alginate gel enhances cell seeding of porous ceramic scaffolds for *in vitro* and *in vivo* bone tissue engineering applications. Most of this research focuses on the processing control and use of 3D porous chitosan–alginate (CA) polyelectrolyte complex scaffolds. The processing of the 3D porous CA scaffolds was systematically evaluated with viscometry, scanning electron microscopy (SEM), and mechanical testing to optimize the scaffold production. 3D porous CA scaffolds of different concentration and pore size were produced using the optimized process and different freezing temperatures. The scaffolds were characterized for bone tissue engineering applications with mechanical testing, SEM, and *in vitro* trials. The scaffolds were then evaluated in a calvarial bone defect model and characterized with MicroCT, histology, and immunostaining for their ability to foster

bone defect repair. The 3D porous CA scaffolds were then used for two cancer research projects. The first project investigated the properties of glioma cells cultured on the CA scaffolds and the rapid enrichment of cancer stem cells, which were characterized through *in vitro* and *in vivo* trials, including SEM, flow cytometry, immunostaining, and tumor formation assays. The second project investigated the ability of the 3D porous CA scaffolds to support culture of prostate cancer cells and co-culture with immune cells for an *in vitro* model to screen potential immunotherapies.

The importance of this research is highlighted by the use of plentiful natural materials to perform biological research to regrow bone tissue and study the behavior of cancer cells and cancer stem cells *in vitro* and *in vivo*. The use of natural materials better replicates the native ECM structure compared to synthetic materials, providing enhanced cellular responses without incorporation of other factors. The natural polymers, chitosan and alginate, resemble the structure of glycosaminoglycans (GAGs), particularly hyaluronic acid, which comprise the native ECM. The combination of these natural polymers with the porous structure provides a 3D environment that is favorable for tissue engineering and cancer research applications, and is superior to synthetic polymers. The 3D porous CA scaffolds provide a platform for bone and other tissue engineering applications, along with improved *in vitro* models for cancer research applications, which allows the potential to enhance drug and immunotherapy discovery trials to produce more efficacious therapies for cancer. The ability to control scaffold properties through processing control allows customization of the scaffolds for various applications.

Organization of Dissertation

Chapter 1 provides a brief introduction to the dissertation, highlighting some of the societal issues addressed by biomaterials, tissue engineering, and cancer research.

Chapter 2 provides an introduction to tissue engineering, including general tissue structure, cell types, and methods to prepare tissue engineering scaffolds, with emphasis on three-dimensional (3D) porous scaffolds.

Chapter 3 discusses bone tissue engineering, providing background on bone biology, current clinical treatments for bone defects, and some of the different materials used in bone tissue engineering applications.

Chapter 4 provides an overview of cancer, cancer stem cells, the effects of the tumor microenvironment on cancer progression, and efforts to provide *in vitro* models of the native tumor microenvironment.

Chapter 5 describes the enhancement of cell seeding of osteoblasts and mesenchymal stem cells (MSCs) in β-tricalcium phosphate (β-TCP) ceramic scaffolds through the use of sodium alginate gel for *in vitro* and *in vivo* bone tissue engineering applications.

Chapter 6 describes the optimization of 3D porous chitosan–alginate (CA) scaffolds through control of processing conditions. This optimized CA scaffold process is used as a platform for the applications described in the remainder of the dissertation.

Chapter 7 presents the preparation and characterization of different concentration and pore size CA scaffolds using the optimized process and evaluation of the produced scaffolds for bone tissue engineering applications.

Chapter 8 evaluates the use of CA scaffolds for functional bone tissue engineering in the treatment of calvarial defects in Sprague-Dawley rats.

Chapter 9 presents the use of CA scaffolds for enrichment of cancer stem cells from human glioblastoma cell lines, indicating that the CA scaffold cultures produce more malignant cultures than do other culture conditions.

Chapter 10 describes the use of CA scaffolds to culture human prostate cancer cells and to screen their interaction with human peripheral blood lymphocytes (PBLs) to use as a platform for *in vitro* trials of immunotherapies.

Chapter 11 summarizes the results and conclusions presented in this dissertation.

2. Tissue Engineering

2.1. Background

The concept of tissue engineering was generally defined during the 1980s, achieving greater popularity and establishment as a distinct discipline in the biomedical sciences after the 1993 article by Robert Langer and Joseph Vacanti, which discussed the new concept of tissue engineering at length [9, 12]. This article sparked considerable research in the nascent field, which has dramatically expanded and matured in the nearly 20 years since. Tissue engineering is an interdisciplinary field that combines the principles of biology and engineering to develop biological substitutes that restore, maintain, or improve tissue function [9]. Tissue engineering strategies can involve three methods, including the application of isolated cells, introduction of growth factors or other molecules, and cells cultured on biomaterial matrices [9]. The use of biomaterials combined with cells and growth factors or the other mentioned treatments attempts to repair damaged tissues to restore function. Tissue engineering could eventually produce full replacement tissues and organs *ex vivo*, eliminating or significantly reducing the need for organ transplants and tissue grafts.

The field of tissue engineering has been bolstered by the discovery of multipotent stem cells, including embryonic stem cells (ESCs) [13], mesenchymal stem cells (MSCs) [14], hematopoietic stem cells [15], and adult stem cells from various tissues, including adipose [16], and others. ESCs can give rise to any tissue in the human body and could form a full human being, but many ethical issues accompany their collection and use [13]. Adult stem cells, including MSCs and other tissue-derived stem cells, possess multipotency and, with proper signaling, can give rise to many various tissue types useful for implantation in tissue engineering applications. Progenitor cells from the tissue of interest can also be used, but they are more difficult to harvest and expand in culture to obtain sufficient cell numbers for implantation.

2.2. General Tissue Structure

Tissues are comprised of cells and extracellular matrix (ECM). Extracellular matrix is a network of various proteins that provide structural support for organs and tissues and a platform for cell adhesion and growth [17]. These ECM proteins form three main classes of molecules—collagen, proteoglycans, and glycoproteins [18]. Collagen is the most widely found ECM molecule in the body; the proteoglycans and glycoproteins are less widely found, but have more specialized functions. These molecules have different properties due to their composition of varying domains (amino acid sequences) and the degree of crosslinking and interaction with other ECM proteins.

The varied tissues in the human body have different functional properties, particularly mechanical ones. The mechanical properties vary greatly based on application, with tissues such as bone and teeth having high compressive strength and toughness, while brain tissue has low compressive strength. Cells respond to the mechanical properties of their substrates [19] and have the greatest biological response to the mechanical properties of their native tissue. The presence of multipotent cells on substrates with different mechanical properties will lead to differentiation into different cell types [19].

Many tissues are formed and maintained by mesenchymal stem cells (MSCs), which are a precursor to the mature phenotype cells found in that tissue [14]. These cells will differentiate into cell lineages based on culture conditions *in vitro* or the chemical and other signals present *in vivo* [14]. As these MSCs differentiate to lineages of mesenchymal tissues, including bone, cartilage, fat, tendon, muscle, and marrow stroma [14], they secrete ECM for the respective lineage and populate the ECM. These cells will differentiate into the mature phenotype as conditions allow, enhancing the development of the tissue. The native ECM will support cell adhesion and growth, along with differentiation to mature phenotype of the cells in the tissue.

2.3. Tissue Engineering Basics

The goal of tissue engineering is to generate biologic substitutes for regeneration of diseased or damaged tissue. Tissue engineering aims to culture living tissue *ex vivo* for

implantation as an alternative for grafts and transplants. Cell-based tissue engineering typically involves the use of a multi-component tissue engineering construct (TEC), which consists of a porous biomaterial scaffold, cells, and growth factors [9, 20]. In its idealized form, tissue engineering would harvest cells (MSCs, other stem cells, or progenitor cells) from the patient, which would be expanded *in vitro*, cultured on a biomaterial scaffold, and differentiated through control of culture conditions into the desired tissue, then implanted into the patient. The idealized form of this therapy would provide personalized treatment and eliminate the immunological risks associated with transplants and grafts from other sources. The ideal biomaterial scaffold should: 1) have a three-dimensional structure with high porosity and an interconnected pore network; 2) support cell attachment, proliferation, and differentiation; 3) bioresorbability with a controlled resorption rate to match tissue growth *in vivo*; 4) induce functional tissue formation via controlled mechanical and biological stimuli; 5) withstand the *in vivo* environment; and 6) provide mechanical support to the defect site [21, 22].

2.4. Porous Scaffolds for Tissue Engineering

Unlike monolithic biomaterials, porous scaffolds are widely used for tissue engineering applications. Porous scaffolds provide openings of various sizes, with mono-dispersed or varied pore sizes, allowing for penetration of cells and blood vessels into and throughout the scaffold. Porous scaffolds also allow for the incorporation of cells and growth factors into the tissue engineering construct (TEC) prior to implantation for delivery to the defect site. Monolithic bioinert or biocompatible biomaterials were used in some of the initial biomaterial trials and were relatively successful, but lacked enhanced interaction with the native tissues. Selection of biocompatible and bioactive materials and the introduction of pores to the materials can achieve greater biological activity. One principle drawback to the use of porous biomaterial scaffolds for tissue engineering applications is the reduction in mechanical properties compared with solid, monolithic biomaterials due to the added porosity. However, the material properties of the porous scaffold are important; researchers have indicated that scaffolds differing in porosity and pore size remain consistent in mechanical properties when porosity is normalized by pore

volume [12]. As polymers are the most widely used biomaterials for tissue engineering, our discussion of processing methods for preparing biomaterial scaffolds will focus on polymeric scaffolds. Porous polymer scaffolds for tissue engineering can be formed by many methods that will be discussed in the next section.

2.4.1. Methods for Forming Porous Polymer Scaffolds

Various methods for forming porous polymer scaffolds for tissue engineering applications have been reported in the literature. They include particle leaching, carbon dioxide foaming, rapid prototyping, and freeze drying, among others. These methods will be described briefly.

Particle leaching is perhaps the most commonly used method to form porous scaffolds for tissue engineering applications. Salt particles or other porogens at defined pore sizes are dispersed in a liquid, particulate, or powder-based material, which is then solidified by crosslinking, or compacted using temperature and pressure [23]. The polymer is soaked in water or other solvent to remove the porogens. The liquid polymer solutions are prepared in an organic solvent. This method is simple and versatile, allowing the production of scaffolds with controlled pore size and geometry, but drawbacks include difficulty fully removing the organic solvents, uneven distribution of porogens, and limited thickness of the produced scaffolds [23, 24].

High-pressure carbon dioxide (CO_2) can be used to form pores in polymers. This method allows for the formation of pores without other chemical additives. The polymer is incubated in high-pressure CO_2 for hours or days to achieve saturation, then the pressure is released, causing the nucleation and formation of pores in the polymer. Disadvantages of this method include limited thicknesses of scaffolds produced, unconnected porosity, and the need for high-pressure chambers [24].

Rapid-prototyping or solid free-form fabrication (SFF) is another method to produce porous scaffolds. It offers the capability to precisely control pore size, pore geometry, pore interconnectivity, and spatial distribution of pores, which are not possible with other scaffold synthesis methods [25–27]. The SFF method is a bottom-up approach where material is deposited layer by layer to form complex open pore structures based on computer-designed

structures [25–27]. Several different approaches are possible with two main synthesis techniques—melt dissolution and particle bonding. The melt-dissolution technique involves deposition of extruded material to create layers that solidify as it cools and fixes to the previous layer [25, 27]. The particle-bonding technique involves selective bonding of particles in a bed of powder to form a thin layer of powder material; then thin 2D layers are produced and bonded to form a complex 3D solid object [25, 27]. While SFF approaches have advantages in control of porosity, several drawbacks include its higher cost compared to other techniques and technical difficulties such as limited accuracy, low mechanical properties, and poor raw material availability [25–27].

Freeze drying is another widely used method to form porous scaffolds for tissue engineering applications. This method involves the preparation of a polymer solution in an aqueous solvent, which is then frozen and lyophilized. The porous structure is formed by the exclusion of the polymer from the freezing solvent, causing the polymer to collect in the interstices between ice crystals. The pore size and porosity are controlled by the polymer composition (solids loading), freezing temperature, and rate of freezing [23].

3. Bone Tissue Engineering

3.1. Bone

Bone is one of the most well-known tissues and it performs many functions in the body. In addition to providing structure as the skeleton, mechanical support for muscles, and allowing motion, bones serve as a warehouse for various trace elements. These elements can be incorporated into bone mineral and sequestered or released as needed to maintain homeostasis through the action of bone cells. The two types of bone tissue are cortical (compact) bone and cancellous (spongy) bone. Cortical bone comprises ~80% of total bone mass, with cancellous bone found primarily at the ends of long bones [28]. Cortical bone forms the tough exterior of bones, while cancellous bone is mainly designed to provide structure within the marrow cavities of long bones and to minimize total bone weight due to their porous structure. If bones were wholly comprised of cortical bone, our skeletons would be considerably heavier, limiting motion.

Bone is a composite of biomineral and biopolymer. The biomineral is hydroxyapatite, $Ca_{10}(PO_4)_6OH_2$, in the form of platelets (30–45-nm long and 5-nm thick) oriented with their *c* axes parallel to one another along collagen fibrils [29]. While hydroxyapatite (HA) is the commonly used name for bone mineral, biologic apatites contain minor and trace elements and should be considered as carbonate hydroxyapatite (CHA) approximated by the formula $(Ca, Na, Mg)_{10}(PO_4, HPO_4, CO_3)_6(OH, Cl, F)_2$ [29]. The biopolymer, or bone matrix, is predominantly type I collagen (>90%) along with non-collagenous proteins, such as osteopontin, osteocalcin, osteonectin, and bone sialoprotein [30, 31]. Secreted non-collagenous proteins regulate the process of bone mineralization, controlling where bone is deposited and determining the biomechanical properties of the mineralized matrix produced [31]. Type I collagen is present as triple helix bundles in fibrils and CHA platelets are oriented along the fibrils [29]. The intimate interaction between the biomineral and biopolymer phases leads to a composite material with enhanced properties compared to the separate phases. The mechanical properties of bone vary by bone density and type, with cortical bone having Young's modulus of 7–30 GPa and

compressive strength of 100–230 MPa, while cancellous bone has Young's modulus of 0.05–0.5 GPa and compressive strength of 2–12 MPa [12]. The composite material provides the enhanced toughness of bone compared to a calcium phosphate ceramic and enhanced compressive strength versus collagen fibrils.

3.2. Bone Cells

Three specific cells populate bone: osteoblasts, osteoclasts, and osteocytes. The osteoblasts are derived from MSCs [14] and secrete osteoid, or unmineralized bone matrix [32, 33]. The secreted osteoid is mineralized after it is deposited, through processes controlled by the non-collagenous bone matrix proteins, which have specialized functions to promote nucleation of bone mineral (osteocalcin) or signals to stop mineral deposition (osteopontin) [31]. Osteoblasts also regulate osteoclast activity by promoting differentiation of osteoclast precursors, providing indirect control of bone resorption and calcium homeostasis [32, 33]. The osteoclasts are multinucleated cells that arise from hematopoietic stem cells and resorb bone mineral through a specialized structure known as a ruffled border [33]. The osteoclast seals onto a section of bone using the ruffled border and secretes acids and proteolytic enzymes, leading to the resorption of the bone under the ruffled border, releasing ions, bone matrix proteins, and growth factors [28]. The body uses these released ions and matrix proteins to produce additional bone or for other biological processes, including metabolism [34]. Depletion of ions in the body through exertion or malnutrition can lead to the resorption of bone in an attempt to maintain homeostasis. Osteocytes are osteoblasts that have differentiated after becoming surrounded by bone [32, 33]. Osteocytes have long processes known as cannaliculi that extend throughout bone structure, allowing the osteocytes to sense microcracks and changes in mechanical loading and direct osteoblast and osteoclast activity [33]. Osteoclasts and osteoblasts communicate through cell–cell contact, diffusible paracrine factors, and cell–bone matrix interaction [33]. These three cell types form a bone multicellular unit (BMU) that is responsible for bone maintenance and remodeling. Despite the static appearance of bone, it is continuously recycled and replaced through a process known as bone remodeling.

3.3. Bone Remodeling

Bone remodeling occurs continuously throughout an animal's life; the complete human skeleton is fully replaced over the course of approximately ten years. Bone remodeling is a complex phenomenon that requires the interaction of the BMU, particularly the osteoblasts and osteoclasts [32, 33, 35–38]. This process involves communication between osteoblasts and osteoclasts to balance bone resorption and bone deposition, while maintaining homeostasis in response to mechanical loading, altered serum calcium levels, and in response to a wide range of paracrine and endocrine factors [34, 38]. Bone remodeling occurs continuously throughout the skeleton at discrete sites. The remodeling cycle begins with the initiation of osteoclast formation, osteoclast-mediated bone resorption, a reversal period, and then a long period of bone matrix formation mediated by osteoblasts, followed by mineralization of the matrix [38]. Bone remodeling also occurs after fractures and this process repairs most bone fractures without the need for surgical intervention [37]. Bone remodeling during fracture healing occurs in four stages: inflammation, soft callus formation, hard callus formation, and bone remodeling [37]. The fracture-healing model is instructive for bone tissue engineering as it presents a sequence of cellular events that lead to bone repair.

3.4. Clinical Treatment of Bone Defects

Bone defects occur through trauma and congenital defects, among other causes. While some bone defects can be repaired by bone remodeling, defects that are too large (critical-sized defects) cannot be repaired without surgical intervention. A critical size defect is the smallest bone defect that will not spontaneously reossify during the lifetime of the patient, resulting in the formation of fibrous connective tissue instead of bone [39, 40]. The current gold-standard treatment for bone defects is autogenous bone graft, but disadvantages are limited graft availability, need for additional surgical sites with risk of donor site morbidity, unpredictable bone resorption, and difficulty molding to the defect [41, 42]. Allogenic bone grafts, from another member of the same species, may also be used, but present greater potential drawbacks,

including disease transmission and potential for immune response, along with lack of osteogenesis and artifacts introduced from graft processing [43]. The limited supply and other drawbacks associated with bone grafts provide motivation to produce an engineered solution.

Alloplast biomaterials, such as polymethylmethacrylate (PMMA) and titanium, can be used to fill the structural bone defects, but these materials are bioinert or have limited interaction with the native bone and pose risk of infection or other complications [41, 44]. Many biomaterials have been investigated as potential alternatives to autogenous bone grafts for bone defect repair, including ceramics, bioactive glass, demineralized bone matrix, and polymers [28, 41, 45, 46]. Despite numerous biomaterials evaluated for bone defect repair, there is no ideal biomaterial for every bone repair application, and different biomaterials are limited by drawbacks such as bioinert or non-resorbable behavior, lack of cell recognition sites and acidic degradation byproducts of synthetic polymers, and potential for brittle failure of bulk ceramic materials [28, 41, 46, 47].

Scaffold-based bone tissue engineering aims to provide a template for bone regeneration while avoiding the drawbacks of bone grafts. For bone tissue engineering applications, scaffolds with an interconnected porous structure and a pore size diameter in the range of 50–1000 μm are required, with the 100-μm pores favored for *in vitro* applications, while pore sizes >300 μm are favored for *in vivo* applications to allow for better vascularization [12, 25, 48].

3.5. Materials Selection for Bone Tissue Engineering

Many materials, including metals, ceramics, and polymers are used in orthopedic applications for bone defect repair, joint replacements, and other applications. The materials can be classified based on their interaction with bone tissue and cells as bioinert or bioactive materials. Bioinert materials do not stimulate bone formation, but instead lead to formation of fibrous tissue and do not bond directly to bone [29]. The use of bioactive materials, which stimulate bone tissue formation and bond with bone, are preferred over bioinert materials for tissue engineering applications [29]. Metals and ceramics, such as alumina (Al_2O_3), have limited interaction with bone tissue, allowing for bone ingrowth and some bonding with bone; however,

they provide limited support for bone cells. Additionally, biodegradable materials are preferred, so that the material is removed after repair of the bone defect. Without the use of biodegradable materials, the implant would remain in the defect site, similar to alloplast materials, for the remainder of a patient's life or require revision surgery to remove it. If the biomaterial remains in the defect site, any differences in mechanical behavior (i.e., stress shielding or potential of brittle fracture with ceramics) may lead to future complications. Consequently, materials used for bone tissue engineering applications typically involve bioactive materials, primarily ceramics and polymers. These two classes of materials for bone tissue engineering applications will be discussed at length in the following sections.

3.5.1. Ceramics

Ceramic materials are a logical choice for bone tissue engineering applications, as bone is comprised of calcium phosphate mineral. Considerable research has focused on the calcium phosphate ceramic system for its application to bone defect repair. Calcium phosphate biomaterials are desirable for bone tissue engineering applications due to the similarities to bone in composition and some properties, including biodegradability, bioactivity, and osteoconductivity [29]. Several calcium phosphate compositions between a Ca/P ratio of 1.0 to 2.0 include tricalcium phosphate, hydroxyapatite, tetracalcium phosphate, and octacalcium phosphate, which all have potential for bone tissue engineering applications. The properties of these calcium phosphate ceramics are primarily governed by the Ca/P ratio, with lower Ca/P ratio typically indicating lower mechanical strength and higher dissolution rate. The most commonly used calcium phosphate ceramics in bone tissue engineering applications are hydroxyapatite (HA) and β-tricalcium phosphate (β-TCP), which have Ca/P ratios of 1.67 and 1.5, respectively, and support culture of osteoblasts and bond with bone. The osteoinductivity of the TCP scaffolds is due to dissolution behavior, which is influenced by calcium phosphate phase and materials properties, including crystallinity, grain size, porosity, and specific surface area [29, 49]. Despite the beneficial properties for bone tissue engineering applications, the low fracture strength and brittle fracture mode of calcium phosphate biomaterials limits them to non-load-bearing areas [29].

A variety of 3D porous ceramic scaffolds for bone tissue engineering applications are commercially available, in addition to the other material structures. An *in vitro* comparison study of six different scaffolds with different calcium phosphate compositions (α-TCP, β-TCP, silicate-substituted HA, bovine HA ceramic, and processed human cancellous allograft), porosity (50–92%), and pore sizes (ranges, 1–1000 μm) were evaluated with human mesenchymal stem cells [50]. The results of this study indicated that the processed human allograft had the greatest cell adhesion and osteogenic gene expression compared with the other materials [50]. This result is instructive for preparing other ceramic materials for bone tissue engineering applications.

Methods to improve ceramic scaffolds for bone tissue engineering applications include increasing the microporosity (pores <10 μm) and improving the mechanical properties. The control of microporosity and grain size in β-TCP and biphasic (HA and β-TCP) scaffolds created scaffolds that were osteoinductive *in vivo*, promoting bone regrowth over similar scaffolds with less microporosity [49]. This induced osteoinductivity in the scaffolds will lead to greater osteogenesis *in vivo* when implanted with other osteogenic factors, further enhancing treatment efficacy. Our group has developed a novel casting method (gel-sponge) to prepare porous ceramic scaffolds with greater mechanical properties than typical porous ceramic scaffolds [51, 52]. This method was used to prepare HA scaffolds and β-TCP scaffolds reinforced with HA nanoparticles [51, 52]. The biphasic scaffolds prepared had compressive strength (9.8 MPa) comparable to the high end of cancellous bone due to the strengthening of the scaffolds with HA nanofibers [52].

The use of HA porous scaffolds in clinical trials for large segmental bone defects was initially reported, followed by report of the long-term follow up after 6 to 7 years [53, 54]. The implanted scaffolds were 100% HA with ~60% porosity (~80% porosity for 1 of 4 patients) and the scaffolds were prepared as cylinders with a hollow central canal [54]. Mesenchymal stem cells derived from the patient were expanded *in vitro*, then seeded on the scaffolds prior to implantation and the implants were held in place with external fixation [53]. The patients had fusion between bone and implant 5 to 7 months post-surgery, and after long-term follow-up, good integration of the implants was maintained with no fractures in the implant zone [54]. While these patients showed good outcomes in the pilot study, 100% HA is typically not used for

bone tissue engineering scaffolds as it does not readily resorb and other calcium phosphate phases, such as β-TCP or the use of biphasic materials, are favored.

3.5.2. Polymers

Polymers are another class of biomaterials commonly used for tissue engineering applications and of considerable interest for bone tissue. Polymers can be divided into two categories based on their origins—synthetic and natural polymers. Bone tissue engineering scaffolds have been described using various synthetic polymer materials, such as poly(L-lactic acid) (PLLA), poly(lactic-co-glycolic acid) (PLGA), poly(vinyl alcohol) (PVA), poly(ethylene glycol) (PEG), or natural polymer materials such as alginate, collagen, and chitosan [22, 47, 55-57]. Synthetic polymers offer greater uniformity in the material composition over natural polymers, but the main disadvantages of synthetic polymers are their lack of inherent biological properties, lack of molecules that support cell attachment, such as glycosaminoglycans (GAGs) and their acidic degradation products, which can affect the *in vivo* culture environment [21, 23, 58]. Natural polymers have greater biological properties than do synthetic polymers due to their glycosaminoglycan (GAG) or GAG-like structures that enhance cell adhesion [23]. Natural polymers are limited by the lack of mechanical properties, the possibility of immunogenicity in animal-derived polymers, and the variation in materials properties due to variation in material sources, which may have varied composition based on the organism the polymer is harvested from and the harvesting procedure [59].

A variety of synthetic polymers, including PLLA, PLGA, PVA, PEG, and PPF, among others, have been used for bone tissue engineering applications [60, 61]. The polymers have been formed into various scaffold structures for the applications. Since the synthetic materials have limited bioactivity, they are often combined with other polymers and growth factors to promote bone regeneration; other have reviewed the use of these composite scaffolds for bone tissue engineering [28, 60].

Natural polymers that have been used for bone tissue engineering include collagen, chitosan, alginate, and silk fibroin [59, 62, 63]. These materials resemble the bone matrix structure and have been evaluated in different forms, including sponges, gels, nanofibers, and

other structures. Collagen, particularly type I collagen, is commonly used in bone tissue engineering applications, since it is the primary component of bone matrix. Type I collagen supports cell adhesion and proliferation and enhances osteogenic differentiation of mesenchymal stem cells [64]. Type I collagen has also been used for delivery of growth factors, particularly BMP-2, as described in the next section. While type I collagen supports mineralization *in vitro* and *in vivo*, it has immunogenicity concerns since it is commonly obtained from animal sources [65]. Type I collagen is also used in composites, often with HA [58, 66]. The use of collagen–HA scaffolds supported *in vitro* culture and differentiation of mesenchymal stem cells with a seeding concentration dependent effect [66].

Chitin is derived from crustacean shells and is the second most common natural polymer on the planet, after cellulose. Chitin is the fully acetylated form of chitosan (chitosan is deacetylated chitin) and consequently, has limited solubility. The lack of solubility limits the applications of chitin, but it has greater mechanical properties than does chitosan. Chitosan is a widely used natural polymeric biomaterial derived from crab and shrimp shells and composed of units of β(1-4) D-glucosamine and β(1-4) N-acetyl-D-glucosamine [59, 62, 67]. Features of chitosan as a biomaterial include cationic character, biocompatibility, biodegradability, hydrophilic character, antibacterial activity, minimal immunogenic response *in vivo*; it bears the proxy structure of glycosaminoglycans (GAGs), a main component of the *in vivo* extracellular matrix [59, 67]. Additionally, due to the cationic behavior of chitosan, it has ability to form complexes with inorganic and biochemical substances, which favor biomineralization and growth factor concentration and retention, respectively [64]. Chitosan has beneficial properties for bone tissue engineering in that it promotes osteoblast growth and mineralized matrix deposition *in vitro*, allows osteoconduction, and promotes osteogenic precursor recruitment, facilitating bone formation *in vivo* [67, 68]. One of the main drawbacks of chitosan is its mechanical weakness, which has led researchers to alter processing methods to enhance the strength or to combine chitosan with other polymeric molecules, such as alginate [23, 68]. Others have reviewed various methods to form responsive and *in situ*-forming chitosan scaffolds for bone tissue engineering applications [69].

Alginate is another widely used natural polymeric biomaterial; it is a linear block copolymer derived from brown seaweed and composed of 1,4-linked β-D-mannuronic acid and α-L-guluronic acid present in varying amounts. Characteristics of alginate as a biomaterial include biocompatibility, immunogenicity, anionic character, thickening character, and gel-forming ability in presence of multivalent counterions [59]. Alginate gels with adhesion peptides (RGD) loaded with growth factors were evaluated in segmental bone defects and demonstrated improved bone healing compared to controls, but the scaffolds degraded slowly and the growth factor dose needed optimization [70]. While alginate is widely used in biomaterial applications, its use in bone tissue engineering applications is limited due to its typically hydrogel structure, unless it is combined with other materials in a composite.

3.6. Growth Factors for Bone Tissue Engineering

Growth factors and other biologic signaling molecules are present *in vivo* with carefully controlled delivery to conduct the numerous processes that occur within the human body. Many growth factors are sequestered in the ECM and released during binding or cleaving of ECM molecules during biological processes [17]. Growth factors used in tissue engineering attempt to replicate the natural delivery of growth factors in the development of the tissue of interest. The use of growth factors in bone tissue engineering enhances osteogenesis and the osteoinductivity of biomaterial scaffolds. Several growth factors, including bone morphogenetic protein-2 (BMP-2), vascular endothelial growth factor (VEGF), and fibroblast growth factor-2 (FGF-2), among others, have been evaluated for use in bone tissue engineering applications [71, 72]. Bone morphogenetic proteins (BMPs) are the most widely used growth factors in bone tissue engineering applications. In 1965 Urist discovered that the BMP protein mix was the active compound responsible for bone regeneration [73]. More than 30 growth factors within the BMP family have varied osteogenic capabilities; BMP-2, BMP-4, BMP-6, BMP-7, and BMP-9 have clearly observed bone-inducing roles [72, 73]. BMP-2 is the most widely used BMP growth factor in bone tissue engineering applications. The FDA has approved the use of recombinant BMPs, specifically rhBMP-2 and rhBMP-7, in adsorbable collagen carriers for spinal fusion and

long bone non-unions [73–75]. While BMPs stimulate osteogenesis, studies have shown that a combination of growth factors may be more effective than a single factor [72]. VEGF stimulates angiogenesis and act synergistically with BMP-2 and BMP-4 [76]. By controlling the concentration of these factors *in vitro* and *in vivo*, osteogenesis can be modulated [71].

Despite the utility of growth factors in enabling tissue development and maturation, it is challenging to deliver sufficient quantities of protein over a sustained period [72, 75]. High doses of BMPs are needed to produce adequate bone formation response, consequently many clinical and preclinical trials of BMPs *in vivo* use supraphysiological doses that are a million times greater than its normal concentration in bone, raising concerns over safety and cost [72]. One potential remedy to this challenge is the use of gene therapy, where genetic sequences encoding for growth factors can be transferred to cells seeded at the defect site, resulting in the production of osteogenic proteins in a localized, sustained, and physiological manner [72, 77–81]. Despite the efficacy demonstrated by gene therapy, disadvantages include the need for vectors that can result in immune response and the use of constitutively active promoters that need regulation to control growth factor production [72]. While gene therapy is promising, many hurdles prevent its clinical application.

Alternatively, growth factor proteins, particularly BMPs, can be combined with a biomaterial carrier to enhance growth factor delivery and retention at the defect site [74, 75]. The FDA-approved BMP-2 and BMP-7 products use a type I collagen sponge to deliver the growth factor to the defect site [72, 74, 75]. A wide variety of synthetic polymers, natural polymers, and ceramics have been investigated for BMP delivery [74].

4. Cancer

4.1. Background

Cancer is a disease that plagues modern society and affects many organs and tissues of the body. Cancer occurs through an evolutionary progression resulting from mutations, or genetic changes, to cells as a result of carcinogens, disorders with genetic maintenance, exposure to radiation, or other causes. DNA replication occurs during cell division with very high fidelity, limiting the occurrence of mutations; when they do occur, typically the cells produced have reduced viability and are eliminated by the immune system. However, when these genetic changes provide the mutated cells with greater survival advantages compared to their healthy neighbors in a tissue, a neoplasm will begin to form. Mutated cells gain survival advantages through either oncogenes, which confer dominant gain of function, or tumor suppressor genes, which have recessive loss of function, both of which may lead to the re-activation of developmental pathways [82].

While there is significant variation among cancers of different tissues and even among cancers of the same tissue and type, common traits, or hallmarks have been defined by Hanahan and Weinberg in 2000 and revisited in 2011. The six hallmarks of cancer include proliferative signaling, evading growth suppressors, resisting cell death, enabling replicative immortality, inducing angiogenesis, and activating invasion and metastasis [82, 83]. Recent progress in cancer research has identified four additional factors of the disease including reprogramming energy metabolism, evading immune destruction, genome instability and mutation, and tumor-promoting inflammation [83]. Many of these hallmarks are deregulated controls of normal cells and tissues, allowing cancer cells gaining evolutionary benefits through the loss of systemic control.

Cancer can begin from a single mutated cell, which forms a neoplasm as it divides. When the neoplasm begins to form, it is either a benign tumor or a malignant tumor. A benign tumor is characterized by slow growth, enclosure in a fibrous capsule, non-invasiveness, and morphologically resembles its cellular precursor, while a malignant tumor grows rapidly, rarely

encapsulates, invades local tissues, does not resemble morphology of its cellular precursor, and metastasizes [84]. While benign tumors are typically cured if treated soon after they are detected, they can become malignant tumors with the accumulation of more genetic instability.

This multistep process of cancer development from transformation of the initial mutated cell to a metastatic cancer occurs through the invasion–metastasis cascade. This process includes growth of neoplastic cells, vascularization of the tumor, invasion of the host tissue stroma, intravasation into local vasculature, transport through the vasculature, arrest in capillary beds, followed by extravasation from the vasculature into distant tissues, formation of micrometastases, and growth of micrometastatic lesions into macroscopic tumors [84–86]. These sequential steps are interrelated and rate limiting, as the entire process can stop at any step, and the outcome of the process depends on both the intrinsic properties of the tumor cells and the responses of the host [86]. Vascularization of the tumor and secretion of angiogenic factors are necessary for the tumor to grow beyond 1–2 mm due to diffusional limitations, and this vasculature provides an initial entry point to the circulatory system.

Once a tumor has begun emitting invasive, metastatic cells, the success of these cells in forming a metastasis in another tissue depends on the suitability of the microenvironment. The tumor emits large numbers of cells daily, but the success rate of establishing a metastasis is very low (0.01%) [86]. The cells may arrest in capillary beds of various organs, but they will only extravasate when they find a favorable tissue microenvironment. Stephen Paget in 1889 proposed this “seed and soil” hypothesis, where the cancer cells or “seeds” enter the vasculature and travel throughout the body until they find suitable “soil” in another tissue with hospitable properties and metastases form only when the seed and soil are compatible [86]. Ewing discredited this theory in 1929, and proposed that mechanical factors of the vascular system anatomy explained the locations of metastases. This concept was disproved and Paget’s hypothesis was confirmed in the 1970s with *in vivo* experiments and review of clinical data [86]. When metastases spread throughout the body, the cancer has progressed significantly and a patient’s chance for survival is greatly diminished, due to the difficulties in treating metastases. Unfortunately in many instances, the initial cancer diagnosis occurs after the dissemination of metastases, limiting the patient’s chance for survival [86].

4.2. Tumor Microenvironment

Tumors are far more complex than the initial model of a homogenous tumor comprised solely of cancer cells. Recent research has lead to consideration of tumors as organs whose complexity approaches and may even exceed that of normal healthy tissues [83, 87]. Tumor complexity is due to the heterogeneous cell population found in the tumor microenvironment, including cancer cells, cancer stem cells, endothelial cells, pericytes, immune inflammatory cells, cancer-associated fibroblasts, and even mesenchymal stem and progenitor cells recruited from the bone marrow [83]. Even the cancer cells comprising the tumor are heterogeneous and vary in degrees of malignancy and metastatic potential [84, 86]. These various cells comprising the tumor microenvironment along with the native ECM contribute to the progression and evolution of the neoplasms into primary tumors and metastatic tumors.

The tumor microenvironment is the physical compartment where cells are exposed to distinct environmental factors from the surrounding tissue; it promotes cancer progression through several mechanisms, including stiffening of native ECM, chronic inflammation, and angiogenesis [88]. Changes to the stroma—which consists of fibroblasts, vasculature, immune cells, and ECM—include increases in ECM stiffness and changes in epithelial cell behavior, which are associated with aging and create a more permissive environment for cancer progression [87]. Inflammatory conditions in the tumor microenvironment can exist prior to tumor formation and contribute to tumor progression, or inflammatory cells can respond to signals from the tumor microenvironment [87]. The fibroblast populations associated with areas of inflammation or developing tumors can alter the properties of the ECM and contribute to cancer progression [87].

The immune system can detect and destroy these developing neoplasms, but if they are located in permissive microenvironments, they may be undetected and evolve unchecked. Even if the neoplasms are detected, some of the less malignant cells may escape immune detection and destruction and proliferate through a form of evolutionary selection known as immunoediting [89]. This process provides two principle methods for tumor cells to evade immune system

recognition and “escape” by either loss of tumor antigen expression or establishment of an immunosuppressive in the tumor microenvironment [89]. The immunoedited tumor cells have acquired mechanisms to evade immune system detection and can progress unchecked by the immune system until further mutations allow for immune detection.

4.3. Use of Biomaterials to Model the Tumor Microenvironment

The desire to cure cancer requires the development of drugs and other therapies to eliminate tumors. Typical drug development trials are conducted using two-dimensional (2D) cultures of homogenous cancer cell lines on tissue culture plastic (TCP), particularly for high throughput applications [87]. This approach identifies successful treatments *in vitro* and they proceed in the development pipeline to *in vivo* preclinical animal trials and clinical trials, where efficacy is typically lower than expected. The lower efficacy is due to the differences between the simplified *in vitro* representation and the complex *in vivo* tumor microenvironment. The two main problems with this 2D culture approach are the lack of three-dimensional (3D) organization and the culture of a single cell type. Despite the convenience of the 2D cultures cultivated on TCP, they lack many of the cues found in the native ECM and the 3D structure, affecting the cell responses compared to the *in vivo* environment, resulting in different responses than may be encountered clinically. The use of 3D cultures can better resemble the native ECM found *in vivo*. Cells behave in a more biologically relevant manner when cultured in 3D compared to 2D, with differences such as diffusion limitations, reduced proliferation, and changes in cell adherance and cytoskeletal organization, among other factors, in 3D cultures versus 2D monolayers [11, 90].

The greater understanding of the heterogeneity of *in vivo* tumors and the complexity of the tumor microenvironment, along with the differences between 2D and 3D *in vitro* cultures, has lead to interest in enhanced models and structures to study cancer and the tumor microenvironment. Ideally, *in vitro* models for cancer drug screening would include some or many of these cell types, such as stromal cells and immune cells, as co-cultures to better mimic the *in vivo* conditions. While some co-cultures of cells have been conducted on 2D surfaces *in*

vitro, they differ from 3D cultures for the reasons previously indicated. Providing the most meaningful data would require the use of 3D structures with several cell types. One method to create more representative *in vitro* culture samples is the use of 3D cultures and biomaterials that better replicate the native tumor microenvironment than do TCP.

The most prevalent 3D *in vitro* culture model in use is multicellular tumor spheroids (MCTS). These cultures often consist of freestanding clusters of tumor cells that self-assemble into spheroids or are induced through the use of materials or other techniques [91–93]. MCTS are most prevalent in cancer research because they are relatively easy to form in a variety of methods and do not require additional materials for culture, which may increase costs of the trial and add complexity to the sample analysis [92, 94]. MCTS recreate the hypoxic conditions within the tumor spheroid and present many of the cues that *in vivo* tumors demonstrate [91, 92]. These spheroids can be co-cultured with other cells from the tumor microenvironment, such as stromal cells, by various methods including mixed spheroids, tumor spheroids cultured on fibroblast monolayers, and tumor spheroids co-cultured with pre-established fibroblast spheroids [92]. While the MCTS do not use material to mimic the ECM, they provide an *in vitro* cancer model that better resembles *in vivo* tumors than do 2D monolayer cultures on TCP.

The use of porous biomaterial scaffolds is rather common for tissue engineering applications. A developing trend is to apply scaffolds and biomaterials developed for tissue engineering applications to cancer research applications to mimic the native tumor microenvironment [11]. The effect of the tumor microenvironment and changes to the tumor microenvironment on tumor progression and growth has been indicated; by using 3D tissue engineering scaffolds in an attempt to recreate the tumor microenvironment, the *in vitro* behavior of cancer cells on these 3D scaffolds can better model *in vivo* conditions than 2D cultures on TCP. Several researchers have begun investigating the tumor microenvironment by culturing cancer cells *in vitro* on various 3D biomaterials that have shown the ability to support culture of cancer cells and better resemble the native tumor microenvironment than does TCP. The following paragraphs briefly discuss use of these materials for *in vitro* tumor models.

Gel polymers are the most commonly used biomaterial structures for *in vitro* tumor models. The most widely used gel polymer for *in vitro* and *in vivo* cancer applications is

Matrigel [95, 96], a natural product prepared as an extract from Engelbreth-Holm Swarm mice tumors. It resembles basement membrane and gels at 37°C [95, 96]. Matrigel is commonly used for *in vitro* 3D cultures and in invasion assays, where invasive cells degrade the Matrigel matrix via protease cleavages and migrate through a porous filter, while the non-invasive cells will remain on top of the filter [95]. This assay can be used to sort and enrich invasive cell populations and to evaluate the efficacy of drugs to regulate invasion and metastasis [95]. Matrigel is also used to enhance tumorgraft (biopsy) and xenograft (cultured cells) "take" and growth *in vivo* as orthotopic tumors in immunocompromised mice, making it easier to establish cell lines from the tumor than directly from a patient biopsy [95].

Other gel polymers used for *in vitro* trials include type I collagen, poly(ethylene glycol) (PEG), and alginate. Type I collagen gel resembles the stroma and has been used for co-cultures of cancer cells and fibroblasts [97, 98]. These examples with adenocarcinomas and breast cancer have demonstrated better performance when co-cultured with fibroblasts, and use of type I collagen gel for both cell types provided an *in vitro* model to investigate the interactions of the co-cultured cells and the efficacy of drugs [97, 98]. The study with the breast cancer cells also investigated the combination of type I collagen gel with Matrigel, which had the best performance compared to the type I collagen gel alone [98]. Additionally, other gel polymers such as PEG and alginate have been used for 3D cultures after being conjugated with adhesion peptides (Arg–Gly–Asp [RGD] integrin-binding motif) [99, 100]. These studies showed that the hydrogels supported culture of oral squamous cell carcinoma and epithelial ovarian cancer cells and provide platforms for further studies with the ability to control matrix properties based on the desired trial conditions [99, 100].

Porous biomaterial scaffolds have also been used for 3D *in vitro* models, including synthetic and natural polymers. Porous poly(lactide-co-glycolide) (PLG) polymer scaffolds were seeded with oral squamous cell carcinoma cells to demonstrate a 3D model of human oral cancer [101]. These 3D scaffold cultured cells had greater malignant behavior *in vitro* and *in vivo* and demonstrated lower drug response *in vitro* compared to cells cultured in 2D [101]. Other research has demonstrated the application of bone tissue engineering scaffolds in a bone metastasis co-culture model [102]. Porous composite scaffolds (medical-grade

polycaprolactone–tricalcium phosphate [mPCL–TCP]) wrapped with human osteoblast cell sheets were then seeded with prostate cancer cells to mimic bone metastasis [102]. The prostate cancer cells showed enhanced expression of markers associated with *in vivo* prostate cancer metastasis, demonstrating the suitability of the model [102]. Research from our group using the 3D porous chitosan–alginate natural polymer scaffolds demonstrated greater malignancy of human glioma cells *in vitro* and *in vivo* and lower drug response *in vitro* with human hepatocellular carcinoma cells [103, 104]. These are just a few examples of the use of 3D porous scaffolds *in vitro* for recreating the *in vivo* tumor microenvironment.

Despite the current progress with improved *in vitro* cancer models, they do not completely replace preclinical *in vivo* trials. Models combining or enhancing the current *in vitro* 3D models are being developed. Combination of the MCTS method with porous scaffolds was demonstrated by incorporating U251 MCTS into porous polymeric scaffolds (collagen-coated poly(lactic-co-glycolic acid) [PLGA] scaffolds) with 500–1000-μm pore diameters [105]. The MCTS retained their spherical morphology for up to 4 days, when they had mostly reverted to behavior similar to the monolayer cultured cells seeded on the scaffold; the MCTS in polymer scaffold samples showed increased drug resistance compared to 2D monolayer cultures, 3D MCTS, and 3D porous scaffolds [105]. This combination method indicates room for improvement in the *in vitro* cancer models, even if the results were only viable for 4 days. Additionally, the incorporation of 3D gel polymer scaffolds with microfluidic devices has allowed for the formation of microengineered organs with co-cultures of cancer cells and stromal cells to evaluate various processes; these devices offer great promise to enhance *in vitro* testing, but many barriers must be overcome to scale up the process [106]. Even with development of drugs using 3D cultures and cutting-edge *in vitro* models, the treatments developed may have lower than expected clinical efficacy due to the many differences between preclinical *in vivo* mouse models and clinical application in humans, requiring the need for better preclinical models for progress against metastatic cancer [107]. While the differences in the preclinical animal models and clinical cases further highlight the gaps in the drug development screening, great progress has been made since 2D monolayer cultures were the only *in vitro* platform used.

5. Enhanced Bone Formation by Alginate Gel-Assisted Cell Seeding in Porous Ceramic Scaffolds and Sustained Release of Growth Factor

Increasing cell seeding efficiency in a tissue engineering construct can enhance cellular activity and tissue formation *in vivo*. Here, we demonstrate the use of alginate gel as a secondary phase material in 3D porous β-tricalcium phosphate scaffolds to improve cell seeding and provide controlled release of growth factors for bone tissue engineering. Cells were seeded in scaffolds in three ways: conventional seeding (CS), alginate gel-assisted seeding (GS), and alginate gel-assisted seeding with bone morphogenetic protein-2 (BMP-2, GSB). *In vitro* study with MG-63 cells showed that cell seeding efficiency and cell population one week after seeding were significantly elevated in GS and GSB samples compared to CS samples. The GSB system demonstrated a sustained, steady release of BMP-2 over two weeks. *In vivo*, scaffolds seeded with rat mesenchymal stem cells were implanted ectopically into Sprague-Dawley rats for eight weeks. GS and GSB samples exhibited improved osteogenic activity, with the GSB samples inducing the greatest osteocalcin and osteoid deposition. This study suggests that the alginate gel-assisted cell seeding increases seeding efficiency and allows for sustained release of growth factors. The use of the secondary phase polymer bolsters bone formation *in vivo* and has the potential to improve outcome in other tissue engineering applications.

5.1. Introduction

Bone defects occur from trauma, infection, and tumor resection and have further complications when load-bearing bones are affected. Autologous and allogenic bone grafts are the current gold-standard treatments for bone defects, but there is limited supply, potential for donor site morbidity, and risk of infection and immunogenic response from allogenic grafts [28, 108]. Three-dimensional (3D) porous biomaterial scaffolds are combined with cells and/or growth factors in a bone tissue engineering construct (TEC) as an alternative to bone grafts [12]. Various 3D porous scaffolds for bone tissue engineering applications have been prepared from polymers and ceramics including chitosan, poly(lactic acid) (PLA), poly(glycolic acid) (PGA),

poly(ethylene glycol) (PEG), poly(propylene fumarate) (PPF), and calcium phosphate ceramics [12, 28, 64, 109]. However, incorporating a large number of cells in a 3D porous scaffold can be challenging. To successfully replace bone grafts, it is crucial to develop a TEC that promotes osteoconductive and osteoinductive behavior while efficiently delivering cells, especially when primary cells are used.

Various methods to improve the cell seeding distribution in the porous scaffold and incorporate growth factors have been introduced to increase the osteogenic behavior of a TEC. The conventional static cell seeding by the drop-wise addition of a cell suspension to a scaffold is widely used, but the technique suffers from low cell-seeding efficiency and cell seeding gradients that lead to inhomogeneous bone regeneration [110, 111]. Alternative dynamic seeding methods such as centrifugal, magnetic field-, and perfusion-mediated seeding have been investigated; however, they have limitations such as the use of additional equipment, the potential of applied forces affecting cell viability and function, and magnetic nanoparticles altering cell function [110, 112-114]. Alternatively, hydrogels such as type I collagen or alginate have been used as a secondary material phase (scaffold is primary phase) to encapsulate cells to increase cell seeding in polymeric scaffolds, which has improved seeding and cellular response *in vitro* compared to statically seeded controls [113, 115, 116].

The incorporation of growth factors into a TEC provides necessary cytokine signaling to enhance tissue regeneration and can also be used to attract cells from the host for defect repair during *in vivo* culture. Bone morphogenetic proteins (BMPs) and other growth factors are released from the damaged bone tissue that increases mesenchymal stem cell (MSC) migration and invasion during fracture repair [37]. However, the incorporation of growth factors directly into the ceramic scaffold can be challenging. The growth factors cannot be directly incorporated into ceramic scaffolds during the processing due to the high temperature required to process ceramic material. Physical coating or chemical conjugation of growth factors on the sintered ceramics can lead to burst release or the compromised bioactivity of the growth factor due to chemical bonding [117–119]. On the other hand, a secondary material phase can provide the ability to both increase cell seeding and controlled release of growth factor.

In this study, we demonstrate the use of a polymer secondary phase with porous ceramic scaffolds in a bone TEC for improved cell seeding and controlled growth factor release. We previously developed a gel-sponge method to prepare 3D porous calcium phosphate ceramic scaffolds with a compressive strength comparable to cancellous bone [51, 52]. We have also previously demonstrated that alginate gel seeding immediately followed by crosslinking produced a uniform distribution of chondrocytes in 3D porous chitosan-alginate polymer scaffolds [116]. Here we develop a bone TEC that employs an alginate gel secondary phase that is crosslinked after a 4-hour cell seeding incubation to improve cell seeding in 3D porous β-tricalcium phosphate (β-TCP) ceramic scaffolds, provide controlled BMP-2 growth factor release *in vitro*, and enhance osteogenesis *in vivo*. Scaffolds seeded with MG-63 osteoblasts were analyzed *in vitro* for evaluation of seeding efficiency, cell population and osteogenic activity. Scaffolds seeded with MSCs were implanted in ectopic locations in Sprague-Dawley rats to assess their ability to induce bone formation.

5.2. Materials and Methods

5.2.1. Scaffold Preparation

Porous β-TCP (β-$Ca_3(PO_4)_2$) scaffolds were prepared via a gel-sponge method reported previously.[51, 52] Cast scaffolds were dried at 100°C overnight and sintered in a muffle furnace according to the following firing cycle: 1°C/min ramp rate to 600°C, dwell at temperature for 1 hour, 3°C/min ramp rate to 1275°C, dwell at temperature for 1 hour. Sintered scaffolds were cut to the desired size (5 × 5 × 5 mm) with a diamond saw. The scaffolds had a porosity of 55.58%, specific surface area of 0.110 m^2/g, and median pore diameter (volume) of 139.68 μm as determined by mercury porosimetry (Micromeritics AutoPore IV 9500).

5.2.2. Cell Seeding

MG-63 osteoblast-like cells (American Type Culture Collection) and MSCs (passage 1) were cultured to confluence in Dulbecco's modified Eagle medium (DMEM, Invitrogen) containing 10% fetal bovine serum (FBS) and 1% penicillin/streptomycin antibiotics. MSCs

were isolated from bone marrow aspirate harvested from Sprague-Dawley rats. β-TCP scaffolds were seeded with MG-63 (*in vitro* trials) or MSC (*in vivo* trials) cells by three methods: 1) conventional, freely diffusive seeding (CS), 2) alginate gel-assisted seeding (GS), and 3) alginate gel-assisted seeding plus BMP-2 growth factor (GSB). Each scaffold was seeded with 3×10^5 cells in a seeding volume of 50 μL in DMEM for CS samples or in a 1:1 ratio of DMEM and 1 wt% sodium alginate (Pronova VLVG sodium alginate, Novamatrix) solution for both GS and GSB samples. Homodimeric BMP-2 was prepared via recombinant *E. coli* synthesis and *in vitro* refolding as previously described [120]. Its efficacy was confirmed against commercial BMP-2 (R+D Systems) and BMP-2 was added at a dose of 50 ng/mL to the cell solution for GSB samples prior to cell seeding. The cell solutions were applied to scaffolds dropwise and the scaffolds were incubated for 4 hours. Following cell seeding incubation, the GS and GSB constructs were crosslinked in 0.2 M $CaCl_2$ for 10 minutes. After crosslinking, all *in vitro* samples were immersed in DMEM and incubated in a humidified environment at 37°C with 5% CO_2 for 7 days with regular media changes. Seeding efficiency, defined as the percentage of the seeded cells that remained in the scaffold after 4-hour seeding incubation, was determined for each group (n = 4) by counting unseeded cells with a hemacytometer and subtracting from total seeded cells (3×10^5).

5.2.3. Cell Proliferation

The cell number within the samples was assessed with the alamarBlue assay (Invitrogen) after 7 days *in vitro* [121]. Samples were incubated for 4 hours at 37°C in a 10% alamarBlue in Opti-MEM phenol red-free media (Invitrogen) and assayed in triplicate at A_{570} and A_{600} on a microplate reader (Molecular Devices) to calculate the percent reduction of the alamarBlue reagent. Standard calibration curves were generated for conventional seeding (CS) and gel-assisted seeding (GS and GSB) methods with known cell numbers to correct for the composition and structure of the scaffolds.

5.2.4. Scanning Electron Microscopy Analysis

Samples cultured *in vitro* for 7 days were fixed with Karnovsky's fixative, successively dehydrated in 50%, 70%, 90%, and 100% ethanol solutions for 15 minutes each and critical-point dried. The samples were mounted, sputter coated with platinum, and the top surfaces were imaged by scanning electron microscopy (SEM; JEOL JSM-7000).

5.2.5. BMP-2 Release Kinetics

Scaffolds were loaded with 1 μg BMP-2 in 50 μL solution volume consisting of a 1:1 ratio of DMEM and 1 wt% sodium alginate using the gel-assisted method and incubated in 10 mL DMEM at 37°C for 13 days. BMP-2 loading was selected based on the detection threshold of the ELISA assay. Supernatant was removed for sampling every other day beginning on day 3 and replaced with fresh medium. Release of BMP-2 was quantified by a sandwich ELISA BMP-2 immunoassay (Quantikine, DBP200), with samples prepared in quadruplicate.

5.2.6. In Vivo Trials of Ectopic Bone Formation

β-TCP scaffolds for *in vivo* trials were seeded by CS, GS, or GSB methods with undifferentiated primary mesenchymal stem cells harvested from rat bone marrow. The samples were seeded in the same manner as the *in vitro* trials, with 3×10^5 MSCs seeded per scaffold in 50 μL, BMP-2 added at 50 ng/mL per scaffold, and 4-hour cell seeding incubation at 37°C. After the incubation, the alginate-containing scaffolds were crosslinked with 0.2 M $CaCl_2$ for 10 minutes and then washed with PBS. Samples were implanted ectopically in an intramuscular pouch in the gluteus muscles on both sides of female Sprague-Dawley rats (n = 9). The implanted samples were divided as follows: 6 empty control scaffolds, 3 CS, 6 GS, and 3 GSB. Specifically, rats were anesthetized with Isoflurane, surgical site was shaved and swabbed with iodine, and a 10-mm incision was made along the hindquarters. An intramuscular pouch was created, a construct was placed in the pouch, and then the pouch and the skin were closed with nylon sutures, with two scaffolds implanted per animal, paired so that the samples were from different sample groups. After 8 weeks, the samples were harvested, fixed in 4 wt% paraformaldehyde, and prepared for histological evaluation. The procedure was approved by and

conducted according to University of Washington IACUC procedures. NIH guidelines for the care and use of laboratory animals (NIH Publication #85-23 Rev. 1985) have been observed.

5.2.7. Histology and Immunohistochemistry

The fixed *in vivo* samples were embedded, decalcified, and sectioned following the common histology practices. The sections were stained with hematoxylin and eosin (H&E) or Masson's trichrome. Osteocalcin protein production was assayed via immunofluorescent staining 8 weeks after *in vivo* implantation. Histological sections were probed with mouse anti-human osteocalcin primary antibody (Abcam, 1:500 dilution) and FITC conjugated goat anti-mouse IgG secondary antibody (Abcam, 1:1000 dilution) following standard methods (Abcam). Cell nuclei were counterstained with 2 μg/mL DAPI nuclear dye (Sigma). Samples were imaged with a confocal laser scanning microscope (Zeiss 510 META LSM). The relative fluorescence intensity of the osteocalcin staining was determined by analyzing high-power fields (630× magnification) and quantitating the amount of fluorescence per field using Adobe Photoshop CS4 (Adobe).

5.2.8. Statistical Analysis

All the data were statistically analyzed to express the mean ± the standard deviation (SD) of the mean. The data were analyzed by one-sided analysis of variance (ANOVA), with post-hoc Tukey-Kramer multiple comparisons to test for statistical significance ($p < 0.01$).

5.3. Results

5.3.1. Cell Seeding Efficiency and Cell Number After One Week In Vitro Culture

We investigated the efficacy of secondary-phase alginate gel-assisted cell seeding in ceramic scaffolds. Figure 1a shows that seeding efficiency in gel-assisted seeding (GS) samples (95.7 ± 5.3%) and gel-assisted seeding plus BMP-2 (GSB) samples (95.3 ± 6.3%) was significantly higher ($p < 0.01$) than in conventionally seeded (CS) samples (59.4 ± 11.3%). Cell number in the sample groups (CS, GS, and GSB) was evaluated by alamarBlue assay after 7 days of culture. The cell number by sample group was 658,125 ± 74,433 for CS, 1,002,903 ± 114,210

for GS, and 1,019,070 ± 122,507 for GSB with significantly higher ($p < 0.01$) cell numbers in GS and GSB samples than in CS samples (Figure 1b). SEM images indicated that the MG-63 cells attached to the scaffold, and were not constrained by the alginate gel after 7 days of culture (Figure 2). Alginate gel is visible in the GS sample low-magnification image. Cells were more readily observed on GS and GSB samples than on CS samples.

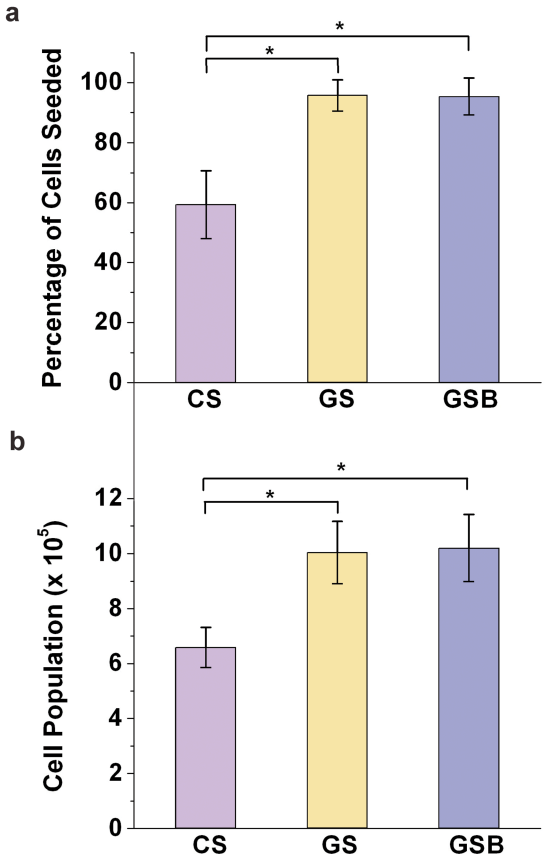

Figure 1. The effects of seeding methods on seeding efficiency and cell population. (a) MG-63 cell seeding efficiency and (b) cell number after 7 days of *in vitro* culture in β-TCP scaffolds. Error bars represent SD, and asterisks denote significant difference ($p < 0.01$, $n = 4$).

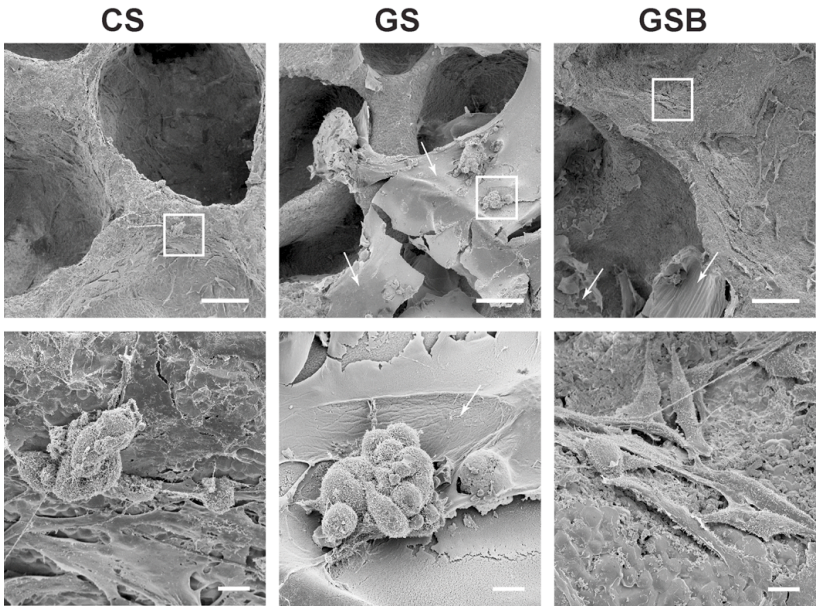

Figure 2. SEM images of MG-63 cells grown on β-TCP after 7 days *in vitro*. The images in the bottom row are enlargements of highlighted regions in the top row. Arrows denote the remnants of alginate gel. The scale bars represent 100 μm (top row) and 10 μm (bottom row), respectively.

5.3.2. BMP-2 Release Kinetics

BMP-2 release from the alginate gel secondary phase was evaluated *in vitro* to determine the release profile. As shown in Figure 3, the BMP-2 release rate remained relatively constant during the study, with the cumulative release profile exhibiting a linear trend. At day 3, only 13.5% (135 ng) of the BMP-2 load had been released. A total of 526 ng of 1 μg of BMP-2 loaded in the alginate gel was eluted by day 13, or 52.6% of the initial loading. The BMP-2 release from alginate gel showed a steady-state release, eluting ~5% of BMP-2 load per day.

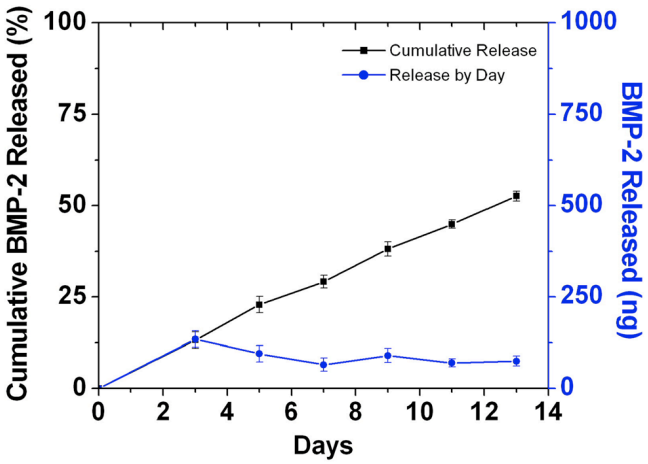

Figure 3. BMP-2 release characteristics of alginate gel in porous ceramic scaffolds, showing daily and cumulative release over a 13-day period, evaluated by monoclonal sandwich ELISA assay, with n = 4. Error bars represent ± SD.

5.3.3. Ectopic Bone Formation

In vivo trials were conducted to investigate the potential translation of enhanced cell seeding and controlled BMP-2 release demonstrated *in vitro* to foster *in vivo* bone development. The cell population and vascularization of the samples were assessed by H&E staining. Figure 4 shows that cells (nuclei, dark red dots) were found throughout all the samples. Visual inspection showed the lowest cell population in CS samples, followed by control, GS, and GSB samples, indicating that alginate gel-seeding method was effective in enhancing cell population within the scaffold. Blood vessels (BV in Figure 4) enclosing a cluster of erythrocytes were observed in all samples.

Osteoid formation *in vivo* was assessed with Masson's trichrome stain (Figure 5), which stains collagen in blue, denoting osteoid that is comprised of ~90% collagen [28]. Osteoid (O) was present in all samples including the control sample, indicating that the β-TCP scaffold had good osteogenic activity. GS and GSB samples showed greater collagen staining than the CS and control samples, indicating that alginate gel-assisted seeding promoted osteoid production.

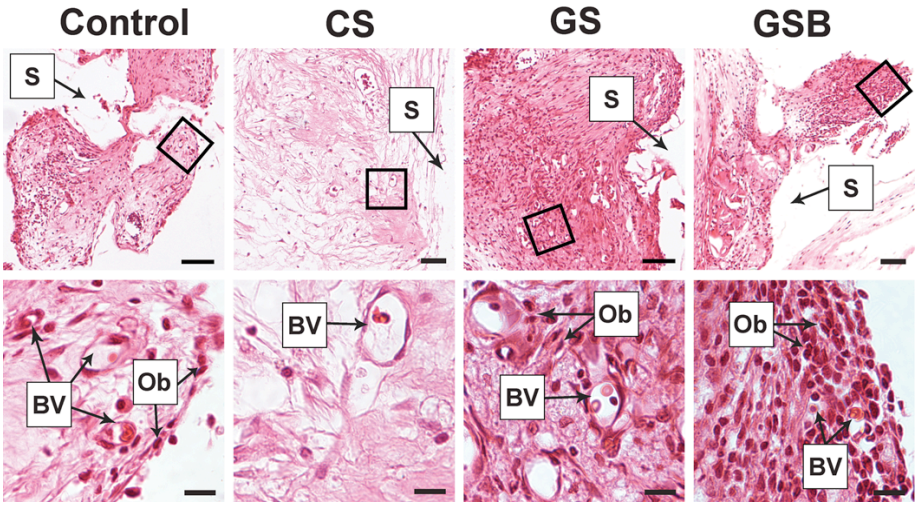

Figure 4. Histological analysis of β-TCP scaffolds with H&E staining. The images in the bottom row are enlargements of highlighted regions in the top row. Blood vessels (BV), osteoblasts (Ob), and scaffold (S) are labeled. Scale bars are 100 μm (top row) and 50 μm (bottom row).

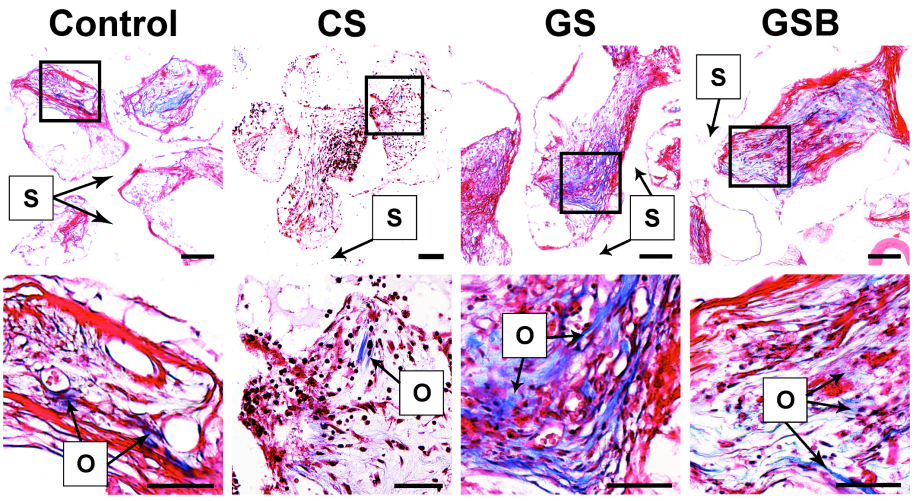

Figure 5. Histological analysis of β-TCP scaffold with Masson's trichrome staining. The images in the bottom row are enlargements of highlighted regions in the top row. Osteoid (O) and scaffold (S) are labeled. Scale bars are 100 μm (top row) and 50 μm (bottom row).

The osteogenic activity was further assessed by immunostaining osteocalcin (Figure 6a). The GS and GSB samples displayed osteocalcin (green) deposited throughout the samples, while the CS sample showed much less osteocalcin present. The osteocalcin protein production was quantified by fluorescence intensity measurements, normalized against the control sample (Figure 6b), which confirmed that the GSB samples had the greatest osteogenic activity,

followed by GS, control, and CS samples, with a statistically significant difference ($p < 0.01$) for all samples except control and CS.

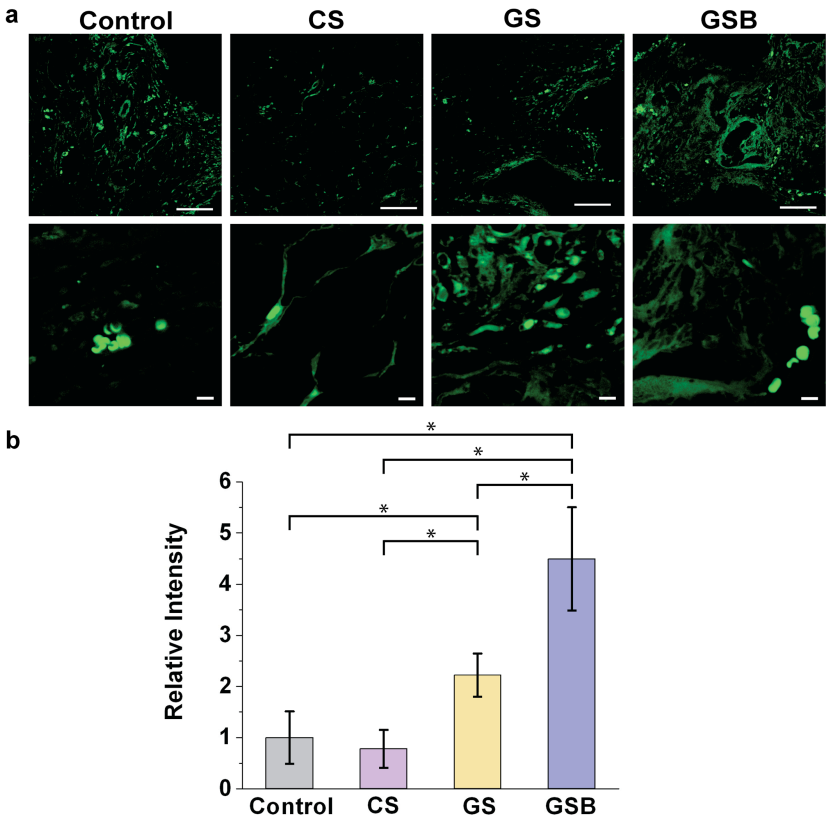

Figure 6. Immunohistochemistry analysis of β-TCP scaffold explants. (a) Confocal microscopy images of osteocalcin (green) immunostained samples; scale bars are 100 μm and 10 μm for top and bottom rows, respectively. (b) Fluorescence intensities of osteocalcin relative to the control sample. Error bars represent SD and asterisks denote significant difference ($p < 0.01$).

5.4. Discussion

Increasing cell seeding efficiency and uniformity in a scaffold will result in enhanced cell communication and behavior, maximizing the response from the seeded cells [122]. The difference in cell seeding efficiency observed between CS, GS, and GSB sample groups (Figure 1a) can be attributed to alginate in the gel-assisted samples (GS and GSB) that provided a structural lattice for cells. The cell and alginate solution in the GS and GSB samples was crosslinked following the 4-hour cell seeding incubation. The non-crosslinked alginate molecules

limited cell migration out of the scaffolds in the GS condition compared to the CS condition. The cells' retention in the gel-assisted samples is further improved after the alginate is crosslinked to form a hydrogel. The increase in cell number in GS and GSB samples after 7 days of culture correlated proportionally to the seeding efficiency, rather than due to increased rate of cell proliferation. The greater cell number in GS and GSB samples after 7 days of culture is likely due to the two-fold benefit of alginate gel-assisted seeding: 1) a greater number of cells are retained on the scaffolds during seeding, and 2) cells are able to proliferate freely within the alginate gel microenvironment. SEM imaging confirmed that GS and GSB samples had greater osteoblast population, with more osteoblasts observed per sample compared to the CS samples (Figure 2).

BMP-2 is on the nanometer scale (7 × 3.5 × 2.5 nm) [123], which allows for its release both through the gel porosity and via gel degradation. Researchers have shown that sustained release of BMP-2 is better for bone healing than a single bolus delivery [72, 79]. The predicted long-term BMP-2 release kinetics would be expected to follow the demonstrated trend during the *in vitro* trial, with complete BMP-2 release during 4 weeks. The BMP-2 release in future trials could be monitored *in vivo* using a chimeric form of recombinant BMP-2 with green fluorescent protein (GFP) added; however, this protein may not behave in the same manner as the native protein [74]. Studies using BMP-2 typically use supraphysiological levels, which may induce pathological bone formation in non-calcified tissues [20, 72, 74, 124]. This study used a small amount of BMP-2 (ng per scaffold as opposed to μg or mg) [74, 124, 125] and still obtained the desired results of enhanced osteogenesis.

The *in vivo* samples seeded with undifferentiated MSCs demonstrated a similar trend to the *in vitro* samples, in that alginate gel secondary phase enhanced cell activity, with GS and GSB samples having enhanced osteoid deposition compared to CS and control samples. The alginate seeding enhanced bone formation due to the improved cell seeding efficiency and uniformity of the scaffolds compared with the conventionally seeded samples. The alginate gel also provided a matrix for the cells that resembles native extracellular matrix [126]. Furthermore, in the GSB samples, the alginate gel provided controlled release of the BMP-2 growth factor, which likely initiated differentiation of the seeded MSCs. The MSCs seeded in the CS samples

likely did not differentiate as effectively to osteoblasts, leading to the reduced osteogenic behavior in the samples. No apparent signs of an inflammatory reaction or influx of macrophages were observed due to alginate degradation *in vivo*. Encouragingly, blood vessels were observed in all samples, as osteogenesis is dependent upon angiogenesis and bone is typically deposited near blood vessels [127]. Furthermore, the addition of BMP-2 to the alginate gel-assisted samples leads to increased osteogenesis. The ability to promote differentiation of MSCs *in vivo* into a desired cell type demonstrates another benefit of alginate gel-assisted seeding.

The control samples in the *in vivo* trial displayed deposited osteoid, indicating the β-TCP scaffolds were osteoinductive, in addition to being osteoconductive. The osteoinductivity of the β-TCP scaffolds is due to dissolution behavior, which is influenced by calcium phosphate phase and materials properties, including crystallinity, grain size, porosity, and specific surface area [29, 49]. The β-TCP scaffolds implanted with MSCs and BMP-2 in the GSB samples showed the best osteogenic performance of the evaluated samples, but it is unclear if the osteogenic activity was due to the osteoinductive effect of BMP-2 on host MSCs invading the construct. Therefore, CSB (conventional seeding with BMP-2) and BMP-2 (scaffold with BMP-2 and no cells) groups would be needed to evaluate whether the inductive effect of BMP-2 on host MSCs promoted osteogenic activity. In future experiments, labeling of the cells seeded on the implanted scaffolds with a fluorescent or other marker would allow a clear determination of which cells, implanted or host, contributed to osteogenesis.

In general, size limitations for TECs, particularly cell-seeded constructs, are restricted by diffusive flow of nutrients and wastes to and from the cells, which *in vivo* is found as 100-μm distance between cells and capillaries in bone tissue [127]. This factor alone would preclude using large construct sizes in TECs, however clinical reports of large (4–7 cm) TEC constructs seeded with MSCs have shown good results with long-term follow-up [54], while other reports in animal studies have indicated difficulties of producing uniform bone formation using TECs (12 x 7 x 3 mm) seeded with MSCs in orthotopic locations [128]. The ceramic scaffolds used in the long-term clinical study had a cylindrical shape with a central pore throughout the scaffold length, which may have contributed to the successful healing of the defects. The ceramic scaffolds used in this study have improved mechanical properties compared to other porous

ceramic scaffolds as demonstrated in our previous papers, which approaches the Young's modulus of cancellous bone [51, 52]. This makes the scaffolds more relevant than other porous ceramic scaffolds for load-bearing applications, and the use of alginate gel as a secondary phase would likely provide further improvements to mechanical properties; however, the mechanical properties of these gel–scaffold samples were not tested. The stronger ceramic scaffolds present promise for treating large load-bearing bone defects, but there are challenging design issues to overcome for the constructs to maximize blood flow and osteogenesis. Additionally, other methods such as using a TEC in combination with a vascularized, free fibular bone graft or other methods to enhance blood flow to the TEC would likely enhance the success rate of the constructs.

In summary, this study illustrated the efficacy of using alginate gel as a secondary phase material with porous ceramic scaffolds in a TEC for bone tissue engineering applications. Compared to conventional seeding, alginate gel-assisted seeding resulted in greater cell seeding efficiency, greater cell retention within the scaffold during culture, sustained release of BMP-2, and improved osteogenic activity *in vivo*. The advantages of uniform cell seeding and ability to serve as a carrier for sustained release of growth factors offer exciting potential for future applications in tissue engineering.

6. Influence of Processing Parameters on Pore Structures of 3D Porous Chitosan–Alginate Polyelectrolyte Complex Scaffolds

Fabrication of porous polymeric scaffolds with controlled structure can be challenging. In this study, we investigated the influence of key experimental parameters on the structures and mechanical properties of resultant porous chitosan–alginate (CA) polyelectrolyte complex (PEC) scaffolds, and on proliferation of MG-63 osteoblast-like cells, targeted at bone tissue engineering. We demonstrated that the porous structure is largely affected by the solution viscosity, which can be regulated by the acetic acid and alginate concentrations. We found that the CA PEC solutions with viscosity below 300 Pa*s yielded scaffolds of uniform pore structure and that more neutral pH promoted more complete complexation of chitosan and alginate, yielding stiffer scaffolds. CA PEC scaffolds produced from solutions with viscosities below 300 Pa*s also showed enhanced cell proliferation compared with other samples. By controlling the key experimental parameters identified in this study, CA PEC scaffolds of different structures can be made to suit various tissue engineering applications.

6.1. Introduction

Chitosan is a widely used natural polymeric biomaterial derived from crab and shrimp shells and composed of units of β(1-4) D-glucosamine and β(1-4) N-acetyl-D-glucosamine. The other features of chitosan as a biomaterial include cationic character, biocompatibility, biodegradability, hydrophilic character, and antibacterial activity [59, 67]. Alginate is another widely used natural polymeric biomaterial, a linear block copolymer derived from brown seaweed and composed of 1,4-linked β-D-mannuronic acid and α-L-guluronic acid present in varying amounts. The other characteristics of alginate as a biomaterial include biocompatibility, immunogenicity, anionic character, thickening character, and gel-forming ability in presence of multivalent counterions [59]. Although both chitosan and alginate are widely used biomaterials, chitosan is mechanically weak and prone to swelling, cells do not bind directly to alginates, and protein adsorption does not usually occur on the negatively charged alginate gel [59]. The

formation of a polyelectrolyte complex (PEC) between chitosan and alginate through ionic interaction between amine and carboxyl groups can enhance the properties of both materials, with each material minimizing the drawbacks of the other material [59, 129].

Chitosan-alginate (CA) PEC has been used to produce nanoparticles, films, and membranes [59, 130, 131]. We previously developed 3D porous CA PEC scaffolds that promoted cell adhesion and proliferation for various tissue engineering applications, including cartilage, bone, and culturing of embryonic stem cells [132–134]. Given this material's importance and potential widespread applicability in tissue engineering and regenerative medicine, we believe that an investigation into the fundamentals of how the processing conditions would lead to the CA materials of different properties would be beneficial to the future development of this material targeted at different tissue engineering applications. For bone tissue engineering applications, scaffolds with a porous structure are required and a pore size in the range of 100–500 μm is preferable [12, 48]. The pore structure of a 3D polymer scaffold depends on several processing parameters including freezing temperature [135, 136], molecular weight of polymer [136], and concentration of polymer solution [137]. These parameters regulate the shape and size of ice crystals formed during freezing and subsequently the scaffold pore size. It has been hypothesized, but not yet validated, that these parameters control the polymer solution viscosity, such that the lower viscosity yields a finer pore structure [135–137]. Both solution viscosity and PEC stability vary with polyelectrolyte ionization, which determines the conformation of the polyelectrolyte (coiled or linear) and is dependent upon pH, ionic strength, and temperature [59, 138].

This work demonstrates an approach to regulate and optimize the pore morphology of 3D porous CA PEC scaffolds by controlling processing parameters. The viscosity of CA PEC solutions were varied by changing acetic acid and alginate concentrations, and the influence of the solution viscosity on scaffold pore structure was investigated. Solution samples were characterized with pH and viscosity measurements, the porous structure was observed with scanning electron microscopy (SEM) imaging, and compressive testing was performed to determine the Young's modulus of the scaffold. In addition, CA PEC scaffolds made with different acetic acid concentrations were tested *in vitro* with MG-63 osteoblast-like cells for 7

days to examine cell proliferation. The evaluation of the effect of these processing parameters on the porous structure of the scaffold will define a more robust CA PEC scaffold process, allowing the scaffold to be tuned to meet the demands of various tissue engineering applications and providing insight to the development of other copolymer systems.

6.2. Materials and Methods

6.2.1. Preparation of Chitosan and Alginate Solutions

All chitosan (practical grade, > 75% deacetylated, MW = 190,000–375,000, Sigma-Aldrich) and alginate (alginic acid from brown seaweed, MW = 80,000–120,000, Sigma-Aldrich) solutions were prepared at 4 wt% polymer concentration unless otherwise noted. Chitosan solutions were prepared in deionized (DI) water with 1.25 wt% acetic acid, whereas alginate solutions were prepared in DI water. Both solutions were prepared by dissolving the raw material powder in the solvent and mixing with a Thinky mixer (ARM-300, Thinky) at 2000 rpm for several minutes. Care was taken to dissipate any excess heat in the mixer between samples to minimize the effect of mixing temperature on the solutions.

6.2.2. Preparation of Chitosan and Alginate Scaffolds

Porous CA scaffolds were prepared by combining equal amounts of chitosan and alginate solutions. The more viscous chitosan solution was added on top of the alginate solution, and the combined solutions were mixed with a Thinky mixer at 2000 rpm to form the CA PEC. After the mixing, the samples were cooled to 25°C for pH measurements, casted in molds, refrigerated at 4°C for 12 hours, and frozen at −20°C overnight. The frozen CA PEC sample was then lyophilized for 24 hours with a Labconco FreeZone 6Plus Freeze Drier (Labconco) under vacuum with collector temperature set at −89°C to sublimate the ice from the CA PEC scaffold.

6.2.3. Viscosity Measurements

The viscosity of the CA PEC solution was measured using a Haake Viscotester VT550 Rheometer (HAAKE) set up with a SV sensor system consisting of a SV cup with a SV2 rotor.

The sample was run at 25°C maintained by a circulating water bath (DC-10, HAAKE), and measured for 1000 seconds up to a shear rate of 100/s.

6.2.4. SEM Imaging

The samples were sectioned, mounted, sputter-coated with platinum, and imaged by scanning electron microscopy (SEM; JEOL JSM-7000F).

6.2.5. Compressive Mechanical Testing

CA PEC samples were cut to size of 8 mm × 4 mm × 4 mm and tested according to the guideline in ASTM D5024-07 standard. Samples were compressed at a rate of 7.0 mm/minute using a micro-mechanical tester with a 1-kg load cell. Young's modulus was determined from the sample compressive plots (n = 10 per condition).

6.2.6. Cell Culture

MG-63 osteoblast-like cells (American Type Culture Collection) were cultured to 80% confluency in Dulbecco's modified Eagle medium (DMEM, Invitrogen) containing 10% fetal bovine serum (FBS) and 1% penicillin/streptomycin antibiotics. Osteoblast-like MG-63 cell lines isolated from human osteosarcoma were selected because they express a number of characteristic features of osteoblasts. CA scaffolds were cut to 2-mm thickness and cross-linked in 0.2 M $CaCl_2$ solution for 10 minutes under vacuum. After crosslinking, the CA scaffolds were washed with excess DI water three times and sterilized in 70% ethanol overnight. The scaffolds were then washed three times with Dulbecco's phosphate-buffered saline (DPBS), immersed in 500 mL DPBS, and shaken on an orbital shaker at 100 rpm overnight to remove any remaining ethanol. Each CA scaffold was seeded with 100,000 MG-63 cells in 100 mL DMEM and incubated for 1 hour to allow cells to migrate through and adhere to the porous structure. The samples were immersed in DMEM and incubated at 37°C with 5% CO_2 for 7 days with regular media changes. The cell proliferation was assessed with the alamarBlue assay (Invitrogen) at several time points during the incubation. For the assessment, samples were incubated for 2 hours at 37°C in a 10% alamarBlue reagent solution in Opti-MEM phenol-free media (Invitrogen). The alamarBlue reagent for each sample was transferred to a 96-well plate and

fluorescence was measured using a microplate reader (Molecular Devices) at excitation wavelength of 570 nm and fluorescence emission read at 585 nm to calculate the percent reduction of the alamarBlue reagent.

6.2.7. Statistical Analysis

All the data were statistically analyzed to express the mean ± the standard deviation (SD) of the mean. The data were analyzed by one-sided analysis of variance (ANOVA), with *post-hoc* Tukey multiple comparisons to test for statistical significance ($p < 0.05$).

6.3. Results and Discussion

6.3.1. Control of Pore Morphology by Variation of Processing Conditions

Several factors influence the pore structure of 3D porous CA PEC scaffolds, including ionic concentration, pH, viscosity, and freezing temperature. Our scaffolds are prepared by a solution-based method that relies on solvent freezing to form the porous structure, so it is particularly sensitive to variations in solution properties. Figure 7 illustrates the contrast between segregated and isotropic CA PEC scaffold porous structures. As observed in the SEM images of sample cross-sections, the segregated sample (Figure 7a) has a locally uniform but exaggerated linear pore morphology, and non-uniform porosity throughout the scaffold, which is not conducive for bone tissue engineering applications due to the elongated rectangular pore shape. The CA PEC scaffold shown in Figure 7b has an equiaxial, relatively uniform pore structure, and was created by retaining a uniform solution temperature at freezing, which promotes the nucleation, rather than rapid growth, of ice crystals. It contrasts with the segregated structure, which is the result of rapid growth of ice crystals and typically occurs when the solution temperature is non-uniform at freezing or the presence of excess acetyl ions. The presence of excess acetyl ions or other ions alters the solvent freezing temperature, leading to different freezing speeds at a common freezing temperature.

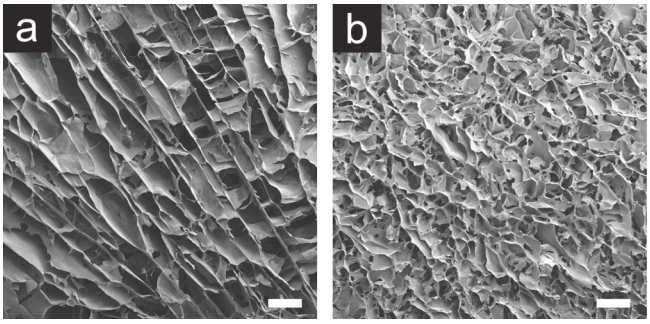

Figure 7. SEM images of (a) segregated and (b) isotropic CA PEC scaffolds made from solution of 4 wt% chitosan, 4 wt% alginate, and 1 wt% acetic acid. The scale bars are 500 μm.

In our previous studies, 3D porous CA scaffolds were prepared using a different procedure [132–134]: sodium alginate was dissolved in a 1 N NaOH solution rather than in DI water as reported here. The previous method also used longer processing times for the blending of the solution at 70°C, while the current method reduces the mixing time substantially by using a Thinky mixer. In either method, after mixing the chitosan and alginate solutions, the pH of the resultant solution can be adjusted to pH 7 to 7.4 by addition of 2 N acetic acid or 2 N NaOH if addition of biological or other factors directly to the scaffold solution is desired. Regardless of solution pH adjustment the CA scaffolds produced by both methods are at pH 7 to 7.4 after crosslinking and sterilizing, allowing cell seeding or modification of the scaffold with other biological factors.

Solution pH affects the ionization of polyelectrolytes (chitosan and alginate) and their interaction to form a PEC; therefore solution pH was measured over a range of acetic acid concentrations for chitosan and CA PEC solutions. The acetic acid concentration had a strong effect on solution pH, as shown in Figure 9. As expected, additional amounts of acetic acid decreased the pH of both solutions, with the CA PEC solution buffered by alginate. The chitosan solution had a linear pH response for acetic acid concentrations between 0.75 to 1.25 wt%, with the pH decreasing from 5.97 to 5.12, indicating the increased protonation of the chitosan molecules. At acetic acid concentrations greater than 1.25 wt%, the chitosan solution pH deviated from the linear trend because the chitosan molecules have been almost fully protonated and are present in an extended conformation. The CA PEC solution showed a similar trend; however, the

acetic acid concentration had less influence on the pH for CA PEC solution than for chitosan solution. Based on Figure 8, a process window for the formation of CA PEC can be defined, with the optimal pH behavior at acetic acid concentrations between 1.0 and 1.25 wt%, allowing for the dissolution of chitosan without altering the alginate behavior. The pH range of the processing window for these materials is limited by their pK values, as chitosan has a pK value of approximately 6 and alginate has a pK value of approximately 3 [59], with mixing at pH values outside this range leading to the precipitation of one of the polyelectrolytes and preventing CA PEC formation. The optimal processing window for CA PEC scaffolds can be further specified by examining the influence of solution viscosity.

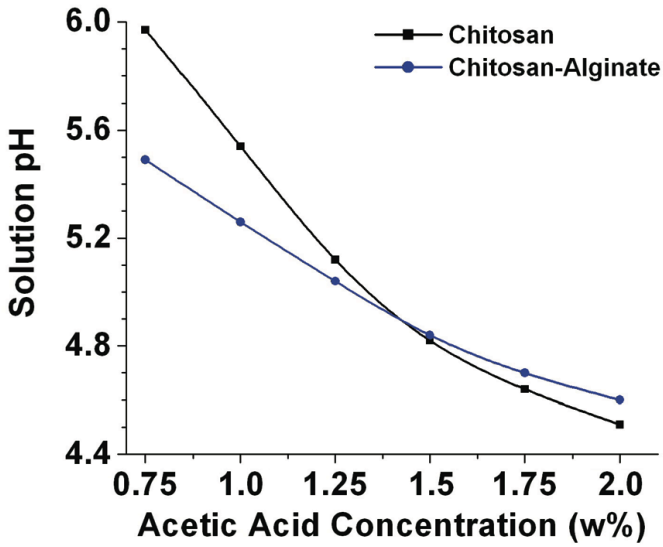

Figure 8. Influence of acetic acid concentration on pH of chitosan solution and chitosan–alginate solution (4 wt% chitosan and alginate solutions).

Solution viscosity is an essential parameter for controlling the CA PEC scaffold structure, and characterizing the changes in viscosity with solution composition (here, primarily the acetic acid and alginate concentrations) will help identify the optimal solution composition for production of ideal CA PEC scaffolds. Figure 9 shows the effect of two solution parameters, acetic acid concentration and alginate concentration, on the zero shear rate viscosity of CA PEC solution. Zero shear rate viscosities for each series were obtained from the viscosity plots

(Figures 10 and 11). The acetic acid concentration was varied over the same range as in the pH measurements (Figure 8) and demonstrated a strong influence on the solution viscosity, which increased from 122.8 to 511 Pa*s as the acetic acid concentration increased from 0.75 to 2.0 wt%. Similar to the pH trend (Figure 8), the solution viscosity increased in a nearly linear fashion in the acetic acid concentration range of 0.75 to 1.25 wt%, and then increased markedly at acetic acid concentrations greater than 1.25 wt%. The greater viscosity with increasing acetic acid concentration suggests the increased protonation of the chitosan. As the alginate concentration increased from 3.5 to 4.5 wt%, the CA PEC solution viscosity increased from 163.4 to 260.1 Pa*s. All CA PEC solutions tested in the alginate concentration trials were prepared with 4 wt% chitosan dissolved in 1 wt% acetic acid. CA PEC solution viscosity increased with the addition of alginate. The viscosity measurements indicated that acetic acid concentration has a more significant effect on CA PEC solution viscosity than does alginate concentration. Although the viscosity of all samples increased as the concentration increased, the samples had a considerably greater viscosity in the higher acid concentration. Furthermore, a threshold can be specified at a solution viscosity of ~300 Pa*s, which defines the borderline between production of isotropic and segregated scaffold morphologies.

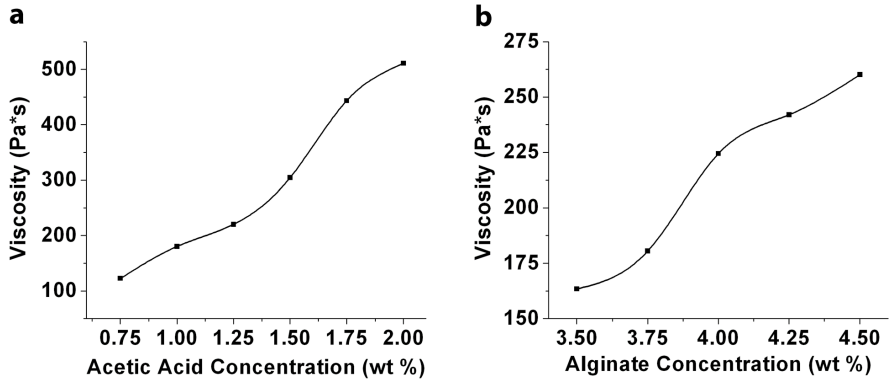

Figure 9. Influence of acetic acid concentration (a) and alginate concentration (b) on viscosity of CA PEC solution at zero shear rate. A 4 wt% chitosan solution and a 4 wt% alginate solution were used for the acetic acid trials, whereas a 4 wt% chitosan solution in 1 wt% acetic acid was used for the alginate trials.

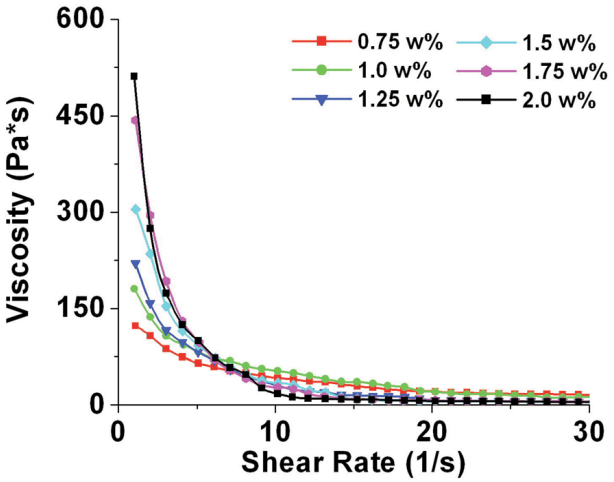

Figure 10. Influence of acetic acid concentration for CA scaffolds solutions on viscosity versus shear rate.

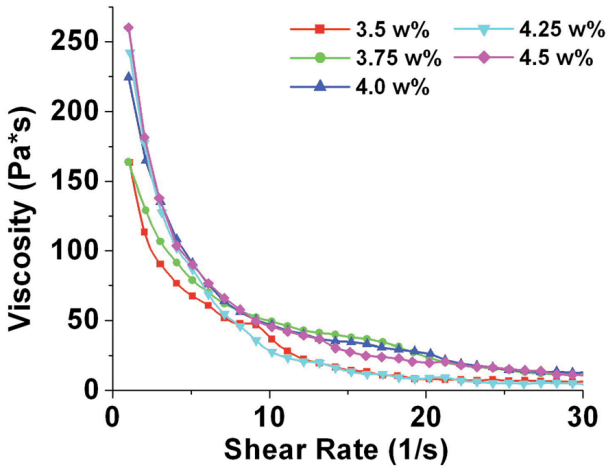

Figure 11. Influence of alginate concentration for CA scaffold solutions on viscosity versus shear rate.

The existence of such a viscosity borderline was confirmed by examining the resulting CA PEC scaffolds from CA solutions of the acetic acid concentration and alginate concentration series. SEM images of the cross-sections of the produced CA PEC scaffolds shown in Figure 12 demonstrate the effect of acetic acid concentration on the CA PEC scaffold pore structure, with the pore shape changing from equiaxed at lower acetic acid concentrations (Figures 12a–12c) to elongated rectangular at higher acetic acid concentrations (Figures 12d–12f). In addition, the scaffold pore morphology becomes more disordered as free acetyl ions in solution increase. This

change occurs as the number of scaffold interconnects (connections between plate-like features defining the pore structure, shown with arrows) decreases in the 1.5 to 2.0 wt% acetic acid samples (Figures 12d–12f), whereas the scaffold struts take on a more jagged appearance. Figure 14 illustrates the effect of increasing alginate concentration (from 3.5 to 4.5 wt%) on the porous structure of the CA PEC scaffold. All the CA PEC scaffolds had a uniform equiaxial porous structure over the range of alginate concentrations tested. The pore structure of CA PEC scaffolds in various alginate concentrations are similar to those of CA PEC scaffolds made from solutions of the lower acetic acid concentrations, and the solutions in both conditions have similar viscosities, all below the 300 Pa*s threshold. The SEM results shown in Figures 12 and 13 support the viscosity analysis shown in Figure 9. Among the scaffolds analyzed, those prepared from solutions with viscosities more than 300 Pa*s exhibited elongated pore structures (Figures 12d–12f), whereas the others have more uniform pore structures.

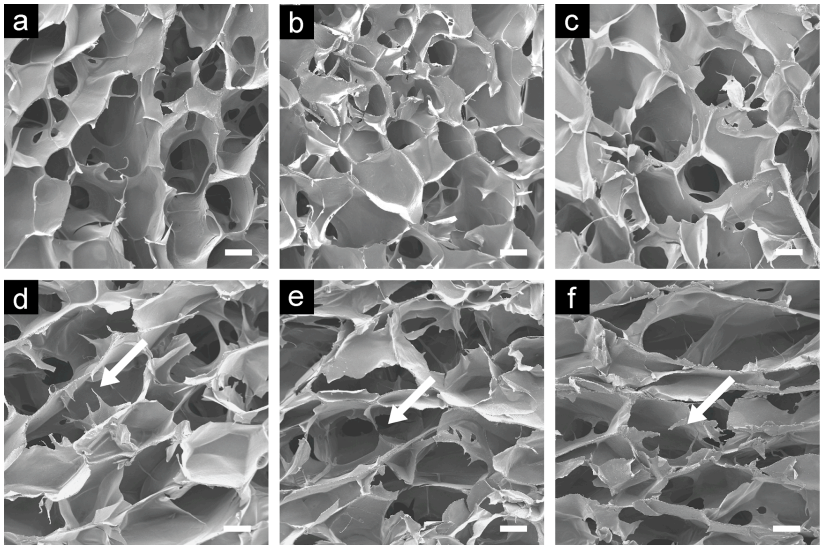

Figure 12. SEM images of the CA PEC scaffold pore structures made from CA solutions (4 wt% chitosan and 3.75 wt% alginate) with acetic acid concentrations of (a) 0.75 wt%, (b) 1.0 wt%, (c) 1.25 wt%, (d) 1.5 wt%, (e) 1.75 wt%, and (f) 2.0 wt%. The arrows indicate incomplete interconnects and scale bars are 100 μm.

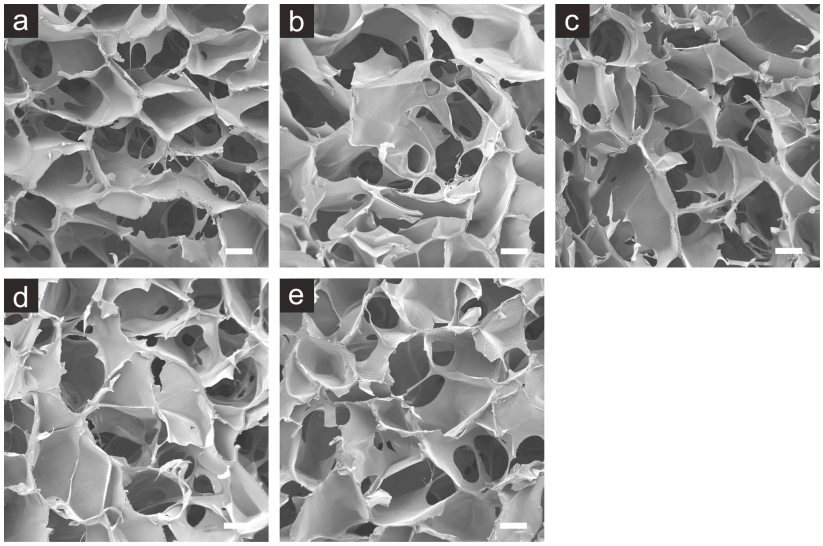

Figure 13. SEM images of the CA PEC scaffold pore structures prepared from CA solutions with a 4 wt% chitosan and 1 wt% acetic acid and alginate concentrations of (a) 3.5 wt%, (b) 3.75 wt%, (c) 4.0 wt%, (d) 4.25 wt%, and (e) 4.5 wt%. The scale bars are 100 μm.

The influence of viscosity on the pore structure can be explained by freezing kinetics of aqueous suspension. When the temperature is lowered to –20°C during the freezing process of the CA PEC suspension, the water is supercooled to a temperature well below its freezing point and ice crystals begin to create a lamellar microstructure by expelling the CA PEC entrapped within channels between the ice crystals. The growth of the crystals forms platelets, oriented in a direction parallel to the movement of the freezing front, with a high aspect ratio as a result of strong anisotropic growth kinetics depending on crystallographic orientation of the ice. As the crystals form, the heat released during the crystallization raises the temperature of the ice to its melting point, resulting in a mixture of ice and water [135] and the entrapment of a small fraction of polymer within the ice crystals in the form of dendrites. During the melting and recrystallization process, the CA PEC dendrites are likely to migrate to form the interconnection between adjacent walls, with the extent is determined by diffusion rate of the CA PEC. The mobility of CA PEC through the mixture of CA PEC and water can be described by the Stokes-Einstein equation of

$$D = k_B T/6\pi r\eta \qquad (1)$$

where D is the diffusion constant of a particle in a liquid, k_B is the Boltzmann's constant, T is the absolute temperature, r is the radius of the particle, and η is the viscosity of the liquid. The equation indicates that the lower the viscosity the better the mobility of CA PEC so that the dendrites, emanated from the walls of the ice crystals, interconnect to form a uniform pore structure after the ice is sublimated by freeze drying as shown in Figures 12a–12c. In the case of a suspension with a high viscosity, the migration becomes difficult and the ice crystals cannot be spanned by the polymer, leading to large irregular pores as shown in Figures 12d–12f. For the alginate concentration series samples, no such irregular pore morphology can be identified because the solution viscosity increases slightly but remains below the critical value of 300 Pa·s.

Furthermore, the influence of other experimental parameters on the CA PEC scaffold formation process was investigated. Figure 14 shows the effect of mixing temperature on CA PEC solution viscosity for a 1.0 wt% acetic acid, 4 wt% chitosan, and 3.75 wt% alginate solution. Increasing the mixing temperature decreases the CA PEC solution viscosity; at the mixing temperature of 40°C, the CA PEC solution had a zero shear rate viscosity 133.3 Pa*s less than the solution mixed at 32°C. The increased mixing temperature lowered the solution viscosity as a result of the reduced molecular chain interaction caused by phonon motion. Temperature has an effect on polyelectrolyte ionization, which determines the conformation of the polyelectrolyte (coiled or extended), leading to variations in solution viscosity and complex stability [59, 138]. Our previous studies showed differences in CA PEC solution viscosity with heat, so the mixer was allowed to cool between samples.

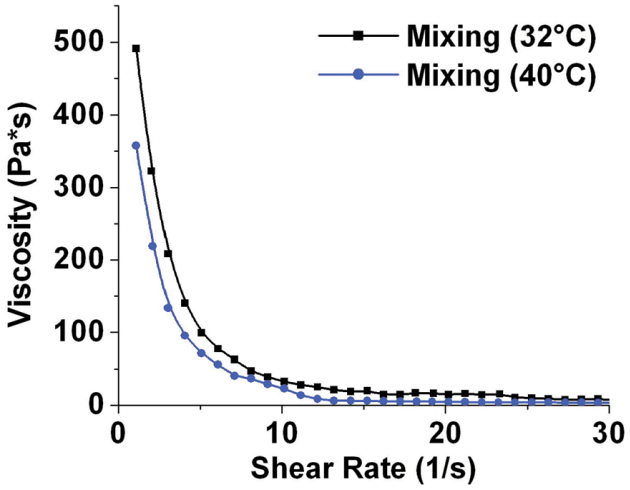

Figure 14. Influence of mixing temperature on viscosity of CA PEC solution (1.0 wt% acetic acid, 4 wt% chitosan, and 3.75 wt% alginate) at zero shear rate.

6.3.2. Compression Testing of CA PEC Scaffolds

The compressive properties of CA PEC scaffolds (4 wt% chitosan and 3.75 wt% alginate) produced with different acetic acid concentrations were evaluated using a micromechanical tester. Figure 15 shows that the compressive Young's moduli of CA PEC scaffolds ranged from 0.7937 MPa (2.0 wt% acetic acid sample) to 1.413 MPa (1.25 wt% acetic acid sample). The 1.0 and 1.25 wt% acetic acid CA PEC scaffolds had the greatest Young's moduli. These results indicate the degree of complexing for each sample, with the 1.0 and 1.25 w% samples having greater complexing than the other samples, because fully complexed polyelectrolytes have higher modulus [138]. The correlation of the highest Young's modulus CA PEC samples with the optimal pH window is not coincidental, because solution pH controls the ionization of polyelectrolytes and their interaction to form a PEC. The 1.0 and 1.25 wt% acetic acid solutions with a pH range of 5.0 to 5.3 were an ideal range for PEC formation with both chitosan and alginate molecules present in an extended conformation. In addition, the 1.0 and 1.25 wt% acetic acid samples had viscosities below 300 Pa*s and equiaxial pore morphology, further reinforcing the 300 Pa*s viscosity cutoff to yield high-quality, fully complexed CA PEC scaffolds.

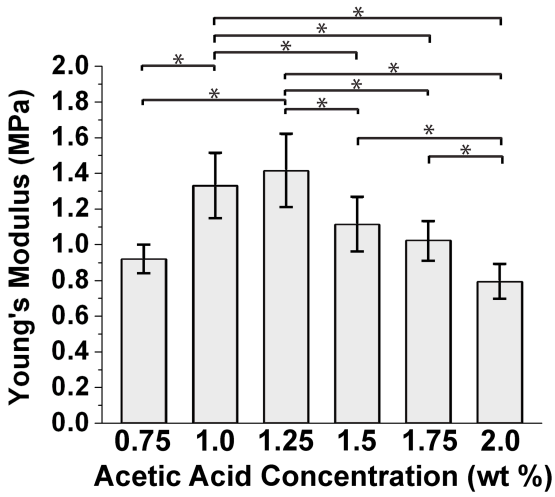

Figure 15. Compressive Young's moduli of CA PEC scaffolds prepared from CA solutions (4 wt% chitosan and 3.75 wt% alginate) with varying acetic acid concentrations. *The significant differences between the scaffold groups for the modulus measurements.

6.3.3. In Vitro Trials

In vitro cell proliferation trials were performed using MG-63 osteoblast-like cells cultured for 7 days on CA PEC scaffolds (Figure 16). The results indicate that MG-63 cells proliferate on all the CA PEC scaffolds, but proliferation is greatest on the scaffolds prepared from solutions with 1.25 and 1.5 wt% acetic acid concentrations. This increased proliferation relative to the other samples is likely due to the combined effect of isotropic scaffold pore structure and the increased polyelectrolyte complexation, as mentioned above. Samples used in the proliferation trials were also imaged with SEM to evaluate cell adhesion, but there was no quantifiable difference between the samples (data not shown). Previous studies have also shown that the Young's modulus of scaffolds influences the cell behavior, with different rigidities suitable for different cell types [19]. Stiffer materials favor interaction with osteoblasts as opposed to a softer material (e.g., a hydrogel). Here the stiffer CA PEC scaffolds show a greater cell number (Figure 16). The pore size and morphology also influence cell proliferation, although the effect is less defined.

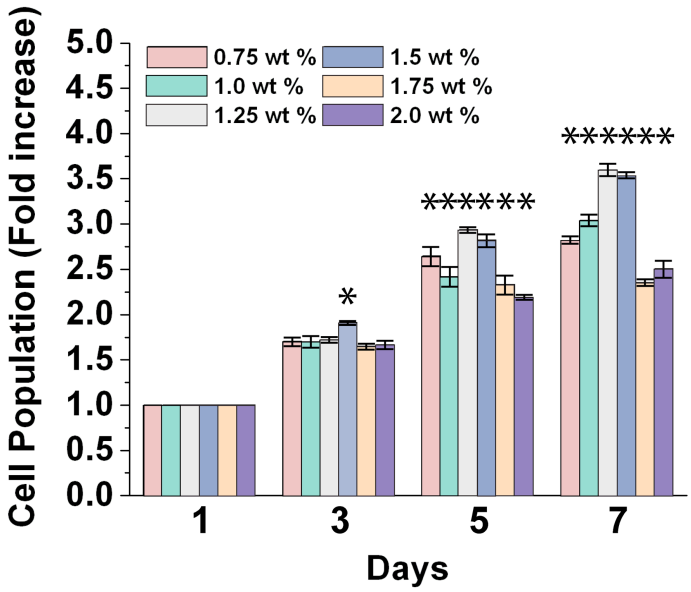

Figure 16. *In vitro* cell proliferation over a 7-day period in CA PEC scaffolds (4 wt% chitosan and 3.75 wt% alginate) prepared from solutions with varying acetic acid concentration. The cell population is normalized to the initial seeded cells. *The significant differences between scaffold groups for cell population.

6.4. Conclusions

We have evaluated the influence of chitosan and alginate solution properties on the pore structure of the resultant CA PEC 3D porous scaffolds. Solution viscosity is the main parameter that regulates the pore structure and mechanical properties. Our results showed that the solutions with viscosity below 300 Pa*s yielded the scaffolds with desired properties for bone tissue engineering applications. We also demonstrated that excess acetic acid would cause the degradation of the desired porous structure, leading to the formation of elongated pores rather than uniform equiaxial pores, whereas variation of alginate concentration had less influence on scaffold pore morphology. CA PEC scaffolds exhibited the greatest compressive Young's modulus at the highest degree of the complexation between chitosan and alginate. MG-63 cells showed greater proliferation on CA PEC scaffolds produced from solutions with viscosities below 300 Pa*s. This analysis enables control of the mechanical properties, cell response, and pore architecture for the scaffold by controlling solution properties. This research identified the

key parameters for CA scaffold synthesis that can be used to fine-tune the scaffold pore structure to meet the needs of different tissue engineering applications.

7. Preparation of Different Concentration and Pore Size Chitosan–Alginate Scaffolds for Bone Tissue Engineering Applications

The use of biodegradable polymers for bone tissue engineering scaffolds is a highly researched topic. The chitosan-alginate (CA) scaffold process developed by our group can produce highly porous scaffolds, with the ability to adjust the properties through processing control. This study demonstrated methods to manipulate the properties of the CA scaffolds by varying the polymer solution concentration and the freezing temperatures. We found that pore size was inversely proportional to the solution concentration and proportional to the freezing temperature. The mechanical properties of the scaffolds increased as the solution concentration increased, with little effect due to pore size. The scaffolds were evaluated *in vitro* with MG-63 cells and the cells proliferated on all the scaffolds, but many scaffolds did not promote cell penetration throughout the scaffold.

7.1. Introduction

Tissue engineering is a field that combines knowledge from the disciplines of medicine, biology, chemistry, and materials science and engineering [139]. Tissue engineering uses tissue engineering constructs (TEC), which combine a biomaterial scaffold with cells and growth factors, to repair damaged tissue. A biomaterial scaffold is a three-dimensional substrate that can serve as a temporary structure to promote tissue regeneration [140]. Many biomaterial scaffolds are investigated for use as TECs to repair bone defects, whose purpose is to promote the natural bone repair process while providing additional mechanical stability to the defect site [28, 139]. Large bone defects and non-union fractures will not heal without surgical intervention and can be challenging to repair [28], which can lead to loss of function in the limb and decrease in the quality of life for the patient [139]. While both autogenous and allogenic bone grafts and have been successfully used to repair bone defects, a synthetic scaffold reduces the risk of complications, decreases surgical procedures, and provides an endless supply of materials [28].

While no single scaffold is successful for every situation, in general tissue engineering scaffolds need to be biocompatible; biodegradable to allow ingrowth of natural tissue; favorable for cell attachment, proliferation, and differentiation; and able to mimic the structure and properties of the native tissue [28, 139]. Bone adapts to the applied load according to Wolff's Law [37], so if materials with greater strength than bone are present, stress shielding can occur, leading to a decrease in the strength of the bone surrounding the material [141]. Metals and ceramics have been used for implants and certain bone tissue engineering scaffolds, however these materials often have a higher strength than the surrounding bone, leading to stress shielding. The necessity for biodegradable materials has led to the use of synthetic and natural polymers for bone tissue engineering scaffolds.

Biodegradable polymers are ideal materials for tissue engineering applications due to adjustable mechanical properties [141], and varying the scaffold properties enables their use for an array of different applications. For instance, the stiffer scaffolds could be used for bone tissue engineering while the more compliant scaffolds could be used for muscle tissue regeneration [142]. The ability to tailor the properties of the polymeric scaffolds for specific applications has led to extensive research with various polymer materials. Two classes of polymers, natural and synthetic, have been researched in tissue engineering with each having advantages and disadvantages. Synthetic polymers are produced in a manner that allows reproducible mechanical and physical properties, including tensile strength, elastic modulus, porosity, and degradation rate [142]. The high degree of reproducibility is the main advantage of synthetic polymers, while the drawbacks are the acidic degradation byproducts and lack of cell-recognition sites [142], which increase the potential for a foreign body reaction when implanted. Natural polymer scaffolds have shown biodegradability and biocompatibility because their materials are similar in structure to native ECM. A disadvantage of natural polymers is low mechanical strength and stability [143, 144].

Polysaccharides are the most common type of natural polymers for biomedical application [143]. In particular, chitosan and alginate are of great interest due to their biological and chemical similarities to natural tissue [59, 129], and both polymers are renewable materials easily processed into different forms ranging from fibers to gels [59]. Chitosan is a derivative of

chitin, which is found in crab and shrimp shells and presents many advantages for tissue engineering use including biocompatibility, osteoconductivity, and surface properties that promote cell adhesion and growth [59]. Alginate is a natural polymer derived mainly from brown seaweed [59, 142]; its advantages for tissue engineering use include low immunogenicity, ease of chemical modification, wide availability, and biocompatibility [59, 143]. While both chitosan and alginate are mechanically weak and cells do not adhere to alginate, the combination of the polymers in a polyelectrolyte complex minimizes the drawbacks while increasing the advantages for a tissue engineering material [59, 133]. Our research group has developed three-dimensional porous chitosan–alginate (CA) scaffolds used for many applications including bone and cartilage regeneration [133], tumor microenvironment [103], and embryonic stem cell culture [134].

The purpose of this study is to demonstrate the preparation of CA scaffolds with different polymer concentrations and pore sizes. The effects of varying polymer concentration and freezing temperature was examined by measuring the mechanical properties, pore sizes, and the behavior of MG-63 osteoblast-like cells on the different scaffolds. The cell behavior was evaluated with the alamarBlue assay to determine the cell population and scanning electron microscopy (SEM) imaging to determine the cell morphology. The CA scaffolds are prepared from equal concentration chitosan and alginate solutions at 2, 4, 6, 8, and 10 wt%, and the scaffold pore size is varied by using different freezing temperatures. Our hypothesis is that the CA scaffold pore size will decrease as freezing temperature decreases and as concentration increases. The MG-63 population should increase as the polymer concentration increases, due to greater similarity to the mechanical properties of bone. Based on the results of these trials, an optimized CA scaffold composition can be chosen for use in other bone tissue engineering applications.

7.2. Materials and Methods

7.2.1. Preparation of Chitosan–Alginate Scaffolds

All of the chitosan and alginate solutions were made with practical-grade chitosan and brown seaweed alginate (Sigma-Aldrich). The solutions were prepared at several concentrations

(2, 4, 6, 8, and 10 wt%) with same concentration chitosan and alginate solutions combined. The chitosan solutions were prepared in deionized water with increasing acetic acid concentrations (0.5, 1.0, 1.5, 2.0, and 2.5 wt%) with respect to the increased chitosan concentrations to maintain a consistent chitosan–acetic acid ratio. Alginate solutions were prepared in deionized (DI) water. The solutions were prepared by dissolving the raw material powder into the solvent. Solutions were mixed in a THINKY mixer (ARM-300, THINKY USA) at 2000 rpm for 3 minutes, manually stirred and mixed for an additional 3 minutes. Once the solutions were completely dissolved, the chitosan solution was added to the alginate solution, then mixed with the THINKY mixer at 2000 rpm for 10 minutes. The combined solution was then transferred to a blender and blended for 5 minutes, then cast in 24-well cell culture plates. The cast samples were refrigerated for 12 hours then frozen. Three freezing methods were used to vary the pore sizes: 1) freezing at -20°C in a chest freezer; 2) freezing on an aluminum plate surrounded by isopropanol in a larger container surrounded by dry ice (-80°C); 3) freezing on an aluminum block in liquid nitrogen (LN_2, -200°C). All samples were thoroughly frozen, then were lyophilized (Labconco FreeZone 6Plus) for 24 hours. The chitosan–alginate scaffolds were sectioned into 2-mm thick samples, crosslinked with 0.2 M $CaCl_2$ under vacuum for 15 minutes, washed with DI water 3 times. The scaffolds were then sterilized under vacuum for 1 hour in 70% ethanol. The sterilized scaffolds were washed 3 times with Dulbecco's phosphate buffered saline (D-PBS), immersed in 500 mL D-PBS, and shaken at 100 rpm overnight on an orbital shaker to remove any remaining ethanol.

7.2.2. Pore Size Measurement

The scaffold samples were imaged with scanning electron microscopy (SEM) and the pore size was measured using the SEM images. Each image had 5 equal-length lines drawn across the image, in parallel, and pores the lines intersected were counted. The number was divided by the scaled line length (based on SEM image scale bar) and the pore size was generated. Several (≥ 3) images for each scaffold sample were used for the measurement.

7.2.3. Mechanical Testing

The mechanical properties were tested in compression with an Instron tester (4505 frame, 5500R) according to the guideline in ASTM D5024-07 standard. Samples were compressed at a rate of 5 mm/minute to 60% of initial height.

7.2.4. In Vitro Trials

MG-63 osteoblast-like cells were cultured in Dulbecco's modified Eagle medium (DMEM) containing 10% fetal bovine serum (FBS) and 1% antibiotics–antimytotic to 85% confluence. Each scaffold was seeded with 50,000 MG-63 cells in 100 μL DMEM and incubated for 1 hour, then 1.5 mL DMEM was added to the samples and they were cultured at 37°C with 5% CO_2 for 15 days with regular media changes.

7.2.5. Cell Proliferation

The cell proliferation was assessed with the alamarBlue assay at various points during the 15-day period. A 10% alamarBlue reagent solution in DMEM was prepared and the samples were incubated in 1 mL of alamarBlue solution for 1.5 hours at 37°C. The alamarBlue solution was then transferred to a black 96-well plate. Fluorescence measurements were taken with a microplate reader (Molecular Devices) at a fluorescence excitation wavelength of 570 nm and fluorescence emission read at 585 nm to calculate the percent reduction of the alamarBlue reagent. The cell population was determined by standard calibration curve.

7.2.6. Scanning Electron Microscopy Analysis

Samples for scanning electron microscopy (SEM) analysis were fixed with 2.5% gluteraldehyde in DMEM for 30 minutes at 37°C, then in 2.5% gluteraldehyde in 0.1 M sodium cacodylate buffer overnight at 4°C. The samples were dehydrated in a series of ethanol washes (0%, 30%, 50%, 70%, 85%, 95%, 100%), with each wash performed twice. The samples were critical-point dried, sectioned, mounted, and sputter coated with platinum, then imaged with a JSM-7000F SEM (JEOL).

7.3. Results and Discussion

7.3.1. Altering Scaffold Pore Morphology

Scaffold pore morphology affects the behavior of cultured cells in tissue engineering applications. Scanning electron microscopy (SEM) images were used to evaluate the pore morphology of the scaffolds. The CA scaffold pore morphology is controlled by the solution concentration and the freezing temperature, with pore sizes generally decreasing from the upper left to the bottom right (Figure 17). The pore sizes for the scaffolds are shown in Table I. The pore sizes range from 253.2 μm for 10 wt% -20°C to 21.8 μm for 10 wt% -200°C. The 10 wt% -20°C pore size may be an outlier due to the pore measuring method or the difference in casting methods for the 8 and 10 wt% samples. If the 10 wt% -20°C sample is excluded, the next largest pore size sample in the series is 214.3 μm for 2 wt% -20°C. The CA scaffold pore size decreased as the weight concentration increased and the freezing temperature decreased.

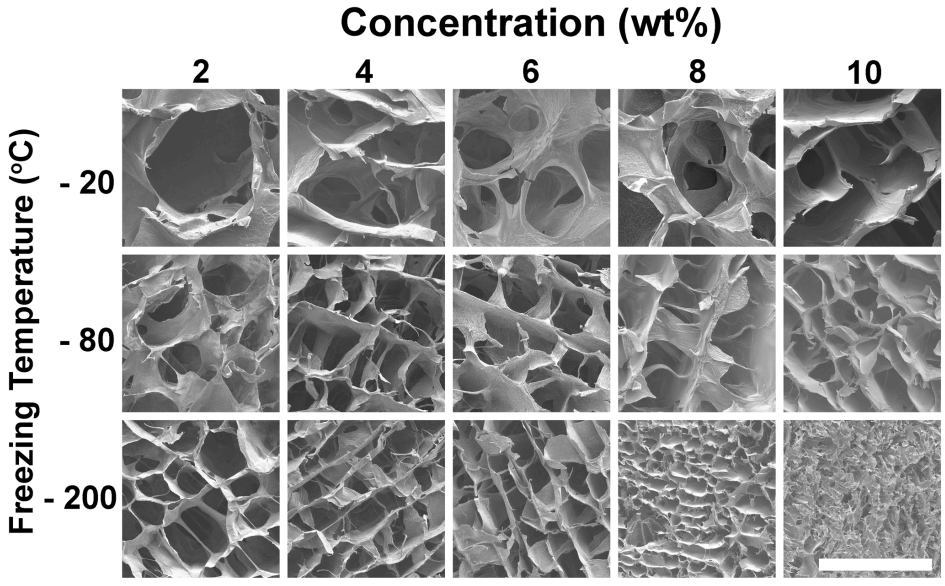

Figure 17. The CA scaffold pore morphology is influenced by polymer concentration and freezing temperature. SEM images of the scaffolds indicate representative pore morphology. The scale bar is 200 μm.

Table I. Pore sizes (μm ± standard deviation) for different concentration CA scaffolds.

	Concentration (wt%)				
Temperature	**2**	**4**	**6**	**8**	**10**
-20°C	214.3±37.7	137.6±29.0	129.0±22.8	124.0±18.9	253.1±118.1
-80°C	71.9±6.8	59.2±11.1	67.3±4.1	93.0±17.7	80.0±13.7
-200°C	61.9±7.8	46.4±5.8	42.7±5.3	25.5±3.3	21.8±2.1

7.3.2. Mechanical Testing

The mechanical properties of the CA scaffolds were evaluated in compression. The samples with increasing weight concentration frozen by the three freezing methods were compared (Figures 18 and 19). The compressive Young's moduli of the CA scaffolds increased as the concentration of polymer increased, from a low of 0.0936 MPa for 2 wt% frozen at -200°C to a maximum of 15.789 MPa for 10 wt% frozen at -20°C (Figure 18). This same increasing trend was also observed for the compressive strength of the scaffolds (Figure 19). Overall, the three freezing temperatures yielded comparable mechanical properties for each polymer concentration; however, the increasing strength of the scaffolds with increasing polymer concentration is a clear trend. As the freezing temperature decreased, the scaffolds experienced a greater increase in strength. Therefore the 10 wt% samples had the greatest strength of all the concentrations and the liquid-nitrogen-frozen 10 wt% samples have the highest strength of 2.908 MPa, while the standard freezer 10 wt% samples had the lowest of 1.56 MPa. This high compressive strength occurs in the liquid nitrogen frozen 10 wt% scaffolds despite their lower Young's modulus, which is likely due to greater amount of material and less void space. This difference in compressive strength and Young's modulus reflects the difference between behavior of the scaffold (Young's modulus) and the accumulation of material during compression (compressive strength).

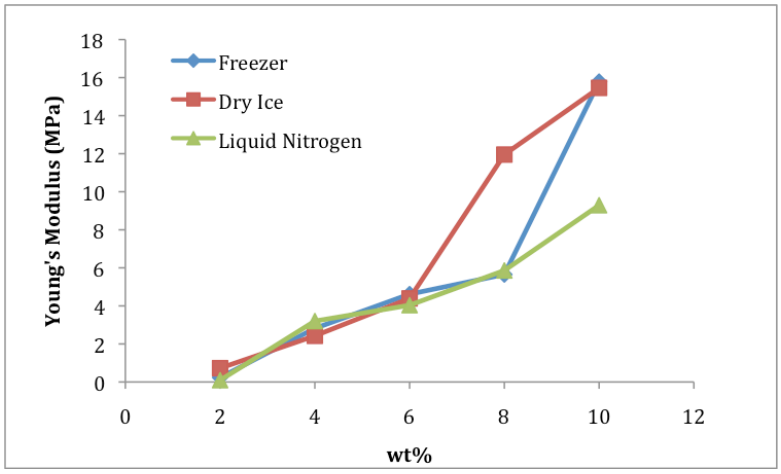

Figure 18. Young's modulus of the scaffolds with varying weight concentration and freezing temperature.

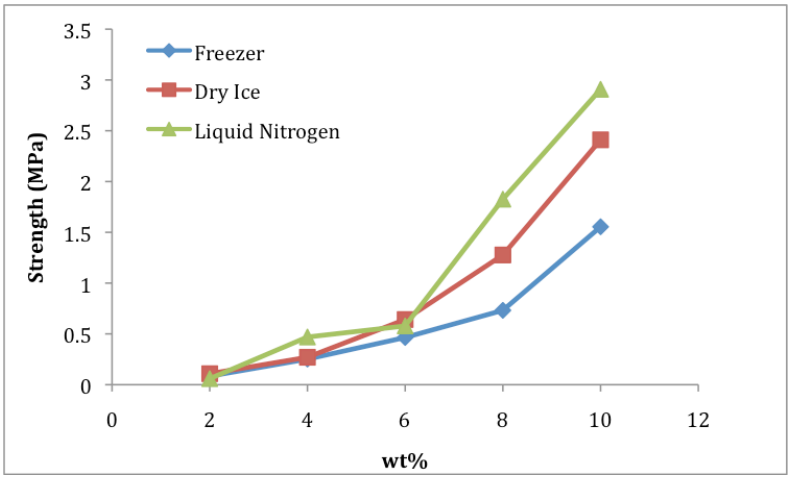

Figure 19. Compressive strength of the scaffolds with varying weight concentration and freezing temperature.

7.3.3. In Vitro Trials

The *in vitro* trials were performed with MG-63 osteoblast-like cells to determine the ability of the different scaffolds to support osteoblast culture for 15 days. The samples were assayed with alamarBlue every 5 days to determine cell population. The results indicated that MG-63 cell adhered and proliferated on all the varied concentrations of scaffolds at each of the

three freezing temperatures. The proliferation of MG-63 on the different concentration scaffolds with standard freezing method and the liquid nitrogen freezing method is shown in Figures 20 and 21, respectively. The two-dimensional well plate was used as a control for the 3D scaffolds and these 2D samples had the greatest cell numbers due to the lack of 3D structure, which creates diffusion limitations and causes the cells to behave in a more representative manner to *in vivo* conditions (Figure 20). Comparing all the different polymer concentration 3D scaffolds revealed the greatest cell proliferation for the 2 wt%, while the 10 wt% had the lowest for the -20°C samples. The samples frozen at -200°C showed a similar trend, with the 2 wt% scaffolds having the greatest cell population at day 15 and the 4 wt% scaffolds having the lowest cell population.

Only the 4 wt% and 6 wt% dry-ice-frozen (-80°C) CA scaffolds were tested in cell culture due to the larger number of samples. Testing the -20°C and -200°C samples for each concentration gave an indication of the effect of polymer concentration and pore size on the MG-63 cells. Testing the -80°C samples for 4 and 6 wt% concentrations provided a full set of data for two of the concentrations, while reducing the overall sample number in culture. Figure 22 compares the cell population for the 4 and 6 wt% CA scaffolds for each of the different freezing temperatures at day 15. The liquid nitrogen freezing method (-200°C) had the greatest cell population for both concentration scaffolds. The 4 wt% dry ice (-80°C) scaffolds also had a comparable cell population. The standard method with the freezer (-20°C) had lower cell populations than did the -200°C samples, but the 6 wt% -20°C scaffolds had a greater population than did the 6 wt% -80°C scaffolds. These results seemed to correlate with the previous proliferation data, where lower freezing temperature yielded greater cell population at day 15.

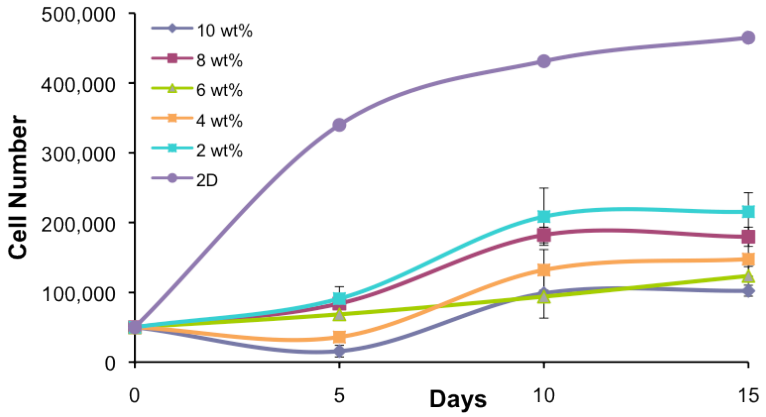

Figure 20. Cell population according to alamarBlue assay for the standard freezer samples (-20°C).

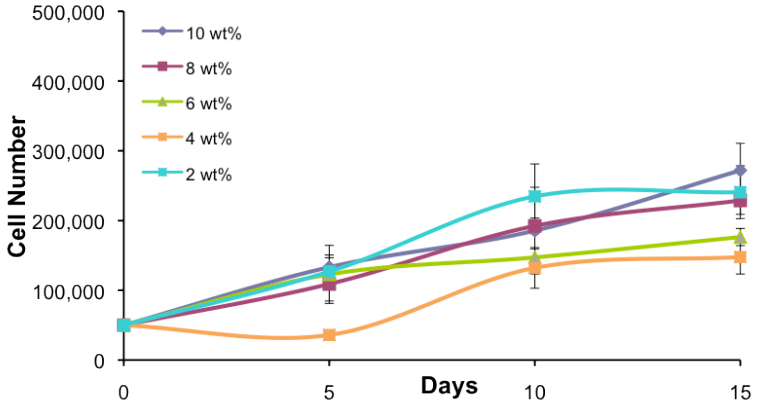

Figure 21. Cell population according to alamarBlue assay for the liquid nitrogen samples (-200°C).

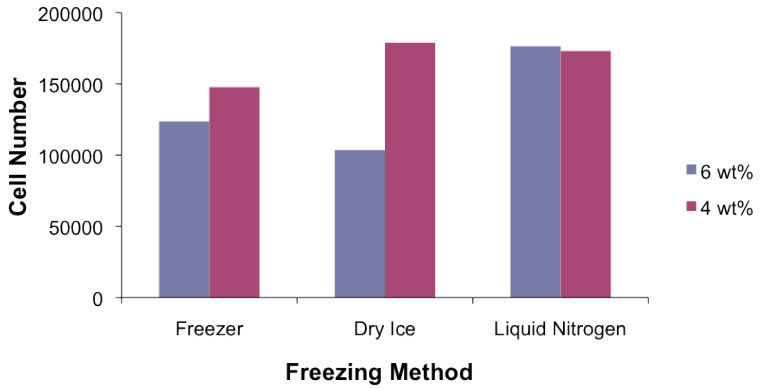

Figure 22. Day 15 cell population for three different freezing methods at two polymer concentrations.

The *in vitro* samples were imaged with SEM to evaluate the cell morphology at day 15. Cells were present on all the samples and the 10 wt% scaffolds had the apparent greatest cell population, as large masses of cells were seen in the -20°C and -200°C scaffolds (Figure 23). The different concentration (4–10 wt%) -200°C scaffolds with the fine pore sizes also showed large masses of cells on the scaffold surface. The masses of cells may indicate that the cells could not readily penetrate throughout the scaffold, especially with the -200°C scaffolds, where the pore size was under 50 μm (for 4–10 wt% scaffolds). These images provided additional data to explain the cell population numbers from the alamarBlue assay.

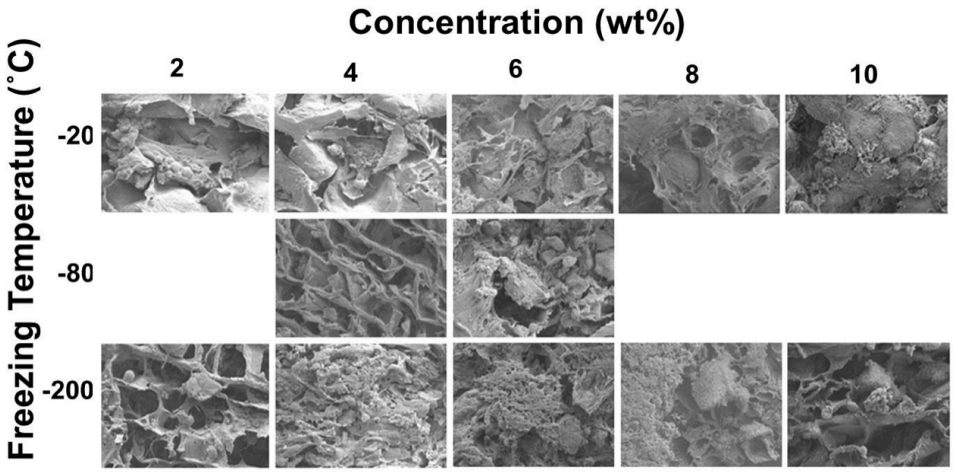

Figure 23. Cell morphology of MG-63 cells on different CA scaffolds at day 15.

We hypothesized that the higher concentration scaffolds would have the greatest cell population since stiffer materials favor osteoblast interaction compared to softer materials due to mechanical properties more comparable to bone. However, the alamarBlue results demonstrated an opposite trend. After examining the cell morphology with SEM imaging, it became clear that several factors were involved. Many of the samples, particularly the higher concentration, fine pore size scaffolds, caused cells to grow in groups on the scaffold surface instead of throughout the porous structure. These scaffolds had pore sizes under 50 μm, which likely contributed to this behavior. Pore sizes around 100 μm are favorable for *in vitro* bone tissue engineering

applications [12, 48]. The scaffolds with greater pore sizes, -20°C series and the 2 wt% concentration samples at all temperatures, had better apparent cell penetration into scaffolds based on SEM imaging. Sectioning the scaffolds and examining planes at different depths would give greater insight to the cell penetration into the scaffold. This study demonstrated the ability to prepare various polymer concentration and pore size scaffolds, but seemed to reinforce the pore size range that is favorable for bone tissue engineering *in vitro*, with pores below 50 μm leading to cell masses forming on the scaffold surface. Due to the conflicting data obtained from the alamarBlue assay and SEM imaging, it seems that the best choice for future experiments is the 4 wt% CA scaffold frozen at -20°C, which provides a good balance of mechanical properties and suitable pore size while using less raw material. Additional work could be performed to increase the pore size of the higher concentration scaffolds to increase the cell number throughout the scaffold.

7.4. Conclusions

This study produced a series of different polymer concentration and pore size CA scaffolds through processing control and the use of different freezing temperatures. The effects of polymer concentration and freezing temperature on the scaffold pore structure and mechanical properties were examined. It was determined that the Young's Modulus and the strength of the scaffolds increased as the polymer concentration increased. Both polymer concentration and freezing temperature influenced the CA scaffold pore structure. As the freezing temperature decreased, the pore size decreased, while as polymer concentration increased, the pore size decreased. The various CA scaffold samples were evaluated *in vitro* and the cell populations were not as expected. The results were better understood with SEM imaging, where it was seen that the cells were not penetrating into the scaffold porosity, especially for the fine-pore scaffolds. Consequently, the best option for future studies is to use the 4 wt% scaffolds frozen at -20°C, which have a good balance of mechanical properties, suitable pore size, while using less raw material.

8. Evaluation of 3D Porous Chitosan–Alginate Scaffolds in Rat Calvarial Defects for Bone Regeneration Applications

This study investigated the use of 3D porous chitosan–alginate (CA) scaffolds for critical size calvarial defect (5.0-mm diameter) repair in Sprague-Dawley rats. CA scaffolds have been used for *in vitro* culture of many cell types and demonstrated osteogenesis in ectopic locations *in vivo*, but have yet to be evaluated for functional bone tissue engineering applications. Results showed CA scaffolds supported culture of undifferentiated mesenchymal stem cells (MSCs) for 14 days *in vitro* and promoted spherical morphology. The treatments tested *in vivo* included CA scaffolds, CA scaffolds with undifferentiated MSCs, CA scaffolds with bone marrow aspirate, and CA scaffolds with bone morphogenetic protein-2 (BMP-2) growth factor, and an unfilled defect (control). The samples were analyzed with MicroCT, histology, and immunohistochemical staining at 4 and 16 weeks. Partial defect closure was observed in all experimental groups at 16 weeks, with the greatest defect closure (71.56 ± 19.74%) in the CA scaffolds with BMP-2 (CA+BMP-2) group. The experimental samples demonstrated osteogenesis in histology and immunohistochemical staining, with the CA+BMP-2 group showing the greatest osteogenesis. Tissue-engineered constructs with CA scaffolds may be a promising alternative in reconstruction of critical size bone defects.

8.1. Introduction

Bone defects arise through genetic disorders and trauma, require surgical intervention when they exceed critical size, and are particularly serious for pediatric patients as they are still developing, with complications of the defect repair potentially having life-long implications [28]. The current gold-standard treatment for bone defects are autogenous bone grafts; however, they have limited graft availability, require additional surgical sites with risk of donor site morbidity, have unpredictable bone resorption, and can be difficult to mold to the defect [41, 42]. The smaller skeleton of pediatric patients reduces the bone volume available for harvesting bone grafts, further limiting the use of autogenous bone grafts [145]. The use of biomaterials for bone

defect repair provides unlimited supply of material and eliminates the need for additional operative sites. A desirable biomaterial treatment for these delicate patients would foster bone repair while degrading with minimal byproducts and allowing growth of the patient.

Many biomaterials have been investigated as potential alternatives to autogenous bone grafts for bone defect repair, including ceramics, bioactive glass, demineralized bone matrix, and polymers [28, 41, 45, 46]. Despite numerous biomaterials evaluated for bone defect repair, no biomaterial is ideal for every bone repair application and different biomaterials are limited by drawbacks such as bioinert or non-resorbable behavior, lack of cell recognition sites and acidic degradation byproducts of synthetic polymers, and potential for brittle failure of bulk ceramic materials [28, 41, 46, 47]. Our research group has developed three-dimensional (3D) porous chitosan–alginate (CA) scaffolds for bone tissue engineering applications [133, 146]. Chitosan and alginate, two natural polymers, are biocompatible, biodegradable, induce minimal immunogenic response *in vivo*, and resemble the structure of glycosaminoglycans, a component of extracellular matrix (ECM) [59]. Chitosan is a natural cationic polysaccharide derived from crustacean shells composed of repeat units of β-1,4 linked N-acetyl-glucosamine and glucosamine that promotes osteoblast growth and mineralized matrix deposition *in vitro*, allows osteoconduction, and promotes osteogenic precursor recruitment, facilitating bone formation *in vivo* [67, 68]. Alginate is a natural anionic polysaccharide derived from brown algae composed of mannuronic and guluronic acids and forms a gel with divalent cations [59]. Individually, chitosan is susceptible to swelling and cells do not bind directly to the negatively charged alginate. Combining oppositely charged chitosan and alginate molecules in solution forms a polyelectrolyte complex through ionic interactions, ameliorating drawbacks of each material [59].

Bone tissue engineering combines biomaterial scaffolds with cells and/or growth factors in a tissue engineering construct (TEC) to enhance bone regeneration [28, 61]. Mesenchymal stem cells (MSCs) harvested from the patient and expanded *in vitro* provide a cell source with minimal complications [61]. Expanding MSCs *in vitro* without differentiation into mature cells (osteoblasts) reduces culture time. Undifferentiated MSCs are recruited to the defect site *in vivo* during the fracture repair process, therefore implanting undifferentiated MSCs should replicate

and potentially augment recruitment of host MSCs [147]. Growth factors, such as bone morphogenetic protein-2 (BMP-2), are commonly used in TECs to enhance bone regeneration [74]. In animal trials and clinical settings with adult patients BMP-2 is delivered in supraphysiological doses, which may cause side effects, such as heterotopic bone formation, undesirable bone growth, and antibody formation [74, 145]. Since the pediatric patient is developing during bone defect repair and many growth factors are present in developmental pathways, it is critical to minimize the use of growth factors in a TEC to the lowest possible level to still achieve a clinically viable outcome.

Here we evaluate the efficacy of 3D porous CA scaffolds for critical size calvarial defect repair. In previous studies, osteoblasts seeded on CA scaffolds proliferated and deposited mineral *in vitro* and CA scaffolds infused with bone marrow aspirate demonstrated bone deposition in ectopic locations *in vivo* [133]; however, they have yet to be evaluated in orthotopic defect sites. CA scaffolds were seeded with undifferentiated MSCs with and without alginate gel and evaluated *in vitro* for 14 days to demonstrate that CA scaffolds support MSCs culture. CA scaffolds were evaluated in critical size calvarial defects in female Sprague-Dawley rats and with treatments including bone marrow aspirate, undifferentiated MSCs in alginate gel, and BMP-2 in alginate gel, and compared to control (untreated defect). Our hypothesis was CA scaffolds would provide greater defect closure and bone deposition compared to untreated defects and other treatments (bone marrow aspirate, MSCs, and BMP-2) would augment defect closure and bone deposition. Our rationale is that an osteoconductive natural polymer scaffold will support bone deposition and alginate gels loaded in CA scaffolds will provide uniform cellular seeding [116] and controlled release of BMP-2 *in vitro*, enhancing defect closure. This study indicates the potential of 3D porous CA scaffolds for functional bone tissue engineering applications in an orthotopic defect site.

8.2. Materials and Methods

8.2.1. CA Scaffold Synthesis

CA scaffolds were prepared as previously reported [133, 146]. The scaffolds were sectioned into 1-mm thick, 7-mm diameter discs, then crosslinked with a 0.2 M $CaCl_2$ solution for 10 minutes under vacuum, washed 3 times with excess DI water to remove any remaining salt, and sterilized in 70 v% ethanol for 2 hours under vacuum. The scaffolds were then washed 3 times with Dulbecco's phosphate-buffered saline (DPBS, Invitrogen), immersed in 500 mL DPBS, and shaken on an orbital shaker at 100 rpm overnight to remove any remaining ethanol.

8.2.2. Cell Harvesting of Mesenchymal Stem Cells

Primary MSCs were harvested from the bone marrow of Sprague-Dawley rats. Specifically, the rat was euthanized and the femurs were removed, sectioned, and irrigated with DPBS to collect the bone marrow suspension and MSCs. Primary MSCs were cultured in fully supplemented Dulbecco's modified Eagle medium (DMEM, Invitrogen) with 1% antibiotic–antimycotic (A-A, Invitrogen) and 10% fetal bovine serum (FBS, Atlanta Biologicals) at 37°C with 5% CO_2 in a humidified incubator. After 48 hours, non-adherent cells were washed away and the MSCs were expanded *in vitro* until 85% confluence.

8.2.3. In Vitro Trials

MSCs (passage 2) were seeded onto 24-well plate wells (2D) and DPBS damp CA scaffolds in 24-well plates at 3×10^5 cells per sample in 20 μL fully supplemented media. CA scaffolds with alginate gel (CA+A) were seeded with 3×10^5 cells in 20 μL of a 1:1 ratio of DMEM and 1 wt% sodium alginate (Pronova VLVG sodium alginate, Novamatrix) solution. The samples were incubated at 37°C and 5% CO_2 in a fully humidified incubator to allow cell adhesion to the substrate for 1 hour. Following cell seeding incubation, the CA+A samples were crosslinked in 0.2 M $CaCl_2$ for 10 minutes. After crosslinking, 1 mL fully supplemented media was added to each well and all samples were incubated in a humidified environment at 37°C with 5% CO_2 for 14 days with regular media changes. CA scaffold samples were moved to a new

plate the day after seeding (d1) to exclude from further characterizations any cells not retained on the scaffold.

8.2.4. Scanning Electron Microscopy Analysis

Samples for scanning electron microscopy (SEM) analysis were fixed with 2.5% glutaraldehyde in fully supplemented media for 30 minutes at 37°C, then fixed in 2.5% glutaraldehyde in 0.1 M sodium cacodylate buffer overnight at 4°C. The samples were dehydrated in a graded ethanol series (0%, 30%, 50%, 75%, 95%, 100%). The samples were critical-point dried, sectioned, mounted, and sputter coated with platinum, then imaged with SEM (JEOL JSM-7000F).

8.2.5. Calvarial Defect Model

The experimental protocol for all animal care and use in this study was reviewed and approved by the University of Washington IACUC, and NIH guidelines for the care and use of laboratory animals (NIH Publication #85-23 Rev. 1985) have been observed. Healthy, 4-week-old female Sprague-Dawley rats were used for the procedures. The rats were anesthetized with Isoflurane prior to the procedure and remained anesthetized for the duration of the procedure. The surgical site was shaved and swabbed with iodine. An incision was made along the top of the skull, with full-thickness reflection of the skin and the periosteum, to expose the calvarium. Critical-size circular calvarial defects (5.0-mm diameter) were created using a surgical drill tool (Stryker) with 3.0-mm trephine burr and constant DPBS irrigation. The defects were measured laterally and longitudinally with calipers during surgery to ensure accurate and consistent circular defects. CA scaffolds were centered in the defect and implanted by tucking the edges of the scaffold (7-mm diameter) under the defect margins. The periosteum was reflected over the defect site, and the incision was closed with 5.0 nylon sutures. Buprenorphine (0.05 mg/kg) was administered subcutaneously postoperatively with an additional injection the day after surgery and as needed. Rats were given free access to food and water and were monitored daily during the postoperative period for any complications. The rats were sacrificed after 4 and 16 weeks according to the University of Washington IACUC procedures. Samples were harvested and

fixed in 4 wt% paraformaldehyde. All samples (entire head) were imaged with MicroCT. Following imaging, the calvarium was explanted for histological and immunohistochemical staining.

Rats (n=30) used for the trials were divided into five groups: (1) empty defect (control); (2) CA scaffolds (CA), (3) CA scaffolds with 3×10^5 undifferentiated rat MSCs in 0.5 w% alginate gel (15 μL total dose, CA+MSC); (4) CA scaffolds with bone marrow aspirate (20 μL total dose, CA+BM); and (5) CA scaffolds with BMP-2 (50 ng/mL concentration) in 0.5 w% alginate gel (15 μL total dose, 0.375 ng BMP-2 per scaffold, CA+BMP-2). Each group had 6 rats with 3 rats for a 4-week time point and 3 rats for a 16-week time point. MSCs for CA+MSC samples were prepared by combining 1 wt% high-guluronic residue alginate (Pronova VLVG sodium alginate, NovaMatrix) solution in a 1:1 ratio with cell solution (MSCs in DMEM media) for a total volume of 15 μL, then applied to the CA scaffold with a pipettor. The CA+BM samples were prepared by adding 20 μL of concentrated bone marrow aspirate to the scaffold with a pipettor. The CA+BMP-2 samples were prepared by combining 1 wt% alginate solution in a 1:1 ratio with BMP-2 in DPBS for a total volume of 15 μL, then were applied to the CA scaffold with a pipettor. Homodimeric BMP-2 was prepared via recombinant *E. coli* synthesis and *in vitro* refolding as previously described[120] and its efficacy was confirmed against commercial BMP-2 (R&D Systems). After loading cells or growth factor on scaffolds, the alginate solution was crosslinked with 0.2 M $CaCl_2$ solution for 10 minutes to form a gel. After crosslinking the scaffolds were washed with DPBS then implanted.

8.2.6. MicroCT Analysis

The samples were imaged using a SkyScan 1172 MicroCT scanner (SkyScan) at 70 KeV and 141 mA with 35-μm isotropic voxel size. Images were reconstructed using DicomCT (SkyScan) and 3D rendered using OsiriX. MicroCT images were used to visualize the samples and measure defect closure. Defects were measured lengthwise and widthwise on 3D-rendered samples in triplicate and percent defect closure was determined by subtracting the measured defect area from the initial defect (5.0-mm diameter) area and dividing by initial defect area, with the difference expressed as percent defect reduction.

8.2.7. Histology Samples

Harvested *in vivo* samples were fixed, decalcified, embedded, and sectioned with a microtome into 5-μm thick sections. Sections were stained with hematoxylin and eosin (H&E), Masson's trichrome, and Von Kossa. Sections for Von Kossa staining were prepared prior to decalcifying the samples. The samples were embedded and sectioned for Von Kossa, then were decalcified, embedded, and sectioned for H&E and Masson's trichrome. The slides were imaged with light microscopy. Percent mineralization of Von Kossa stained slides was semi-quantitatively determined by converting high-power fields (100× magnification) of the samples to black and white and analyzing the amount of black (mineralization) per field using Adobe Photoshop CS4 (Adobe). Fields were selected for analysis by focusing on the defect site, with one field used per sample (n=3 per sample group). The percentages reported were based on the entire field being black as 100% and the entire field being white as 0%.

Immunohistochemical analysis of osteocalcin and osteopontin protein deposits was performed on the 16-week samples to assess osteogenesis within the calvarial defects. Histological sections were probed with mouse anti-rat monoclonal osteocalcin primary antibody (1:100 dilution, Abcam) and rabbit anti-rat polyclonal osteopontin primary antibody (1:250 dilution, Abcam) following standard methods (Abcam). The primary antibodies were detected with Texas Red conjugated goat anti-mouse IgG secondary antibody (1:1000 dilution, Abcam) and FITC-conjugated goat anti-rabbit IgG secondary antibody (1:1000 dilution, Abcam). Cell nuclei were counterstained with DAPI (Prolong Gold with DAPI, Invitrogen). Samples were imaged with a confocal laser scanning microscope (Zeiss 510 META LSM). The relative fluorescence intensity of osteocalcin- and osteopontin-stained slides was semi-quantitatively determined by analyzing high-power fields (630× magnification), with one field used per sample (n=3 per sample group), and quantitating amount of fluorescence per field using Adobe Photoshop CS4.

8.2.8. Statistical Analysis

All the data were statistically analyzed to express the mean ± the standard deviation (SD) of the mean. The data were analyzed by one-sided analysis of variance (ANOVA), with post-hoc Tukey-Kramer multiple comparisons to test for statistical significance ($p \leq 0.05$).

8.3. Results and Discussions

8.3.1. Synthesis of Chitosan–Alginate Scaffolds

The 3D porous structure of the CA scaffolds is produced by a thermally induced phase separation method, followed by solvent sublimation through lyophilization. The as-prepared cylindrical scaffolds were cut into 7-mm diameter and 1-mm thickness sections for *in vitro* and *in vivo* studies (Figure 24a, section shown is 13-mm diameter and 2-mm thickness). The CA scaffolds have an interconnected porous structure (90% porosity) with an average pore size of ~100 μm as shown in the SEM image (Figure 24a inset). After crosslinking, CA scaffolds are flexible and resilient as shown in Figure 24b, allowing custom molding into bony defects. CA scaffolds could be cut in the operating room with sterile scalpel or scissors to produce the desired fit, allowing surgeons to easily customize the scaffold to fit the defect closely, which is not possible with sintered ceramic scaffolds. The overview of the cranial defect model is shown in Figure 24c with the position of the 5.0-mm diameter calvarial defect on the rat skull shown by MicroCT in Figure 24d.

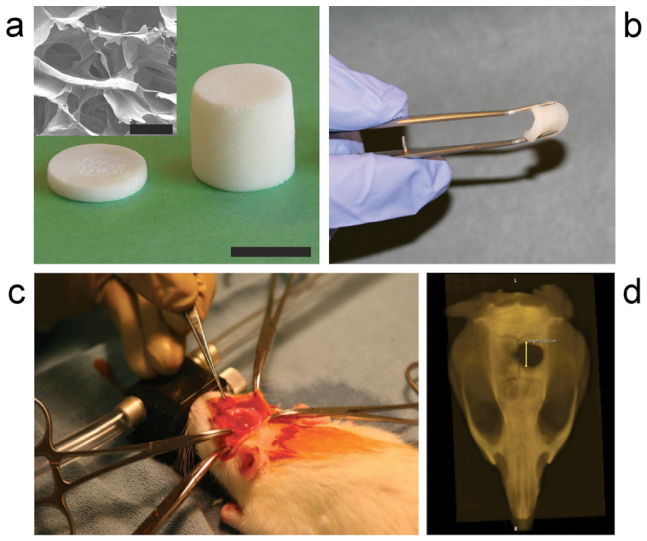

Figure 24. Use of chitosan–alginate (CA) scaffolds for cranial defect repair. (a) CA scaffolds are produced as cylinders and cut into slices (scale bar = 10 mm); (a, inset) SEM image of scaffold shows the pore morphology (scale bar = 100 μm); (b) crosslinked CA scaffolds are flexible and resilient; (c) cranial defect model is shown during procedure and (d) illustrated by MicroCT (line = 5.0 mm).

8.3.2. In Vitro Trials

The CA scaffolds seeded with MSCs were cultured *in vitro* for 2 weeks to verify that the scaffolds support MSCs culture. SEM imaging was used to observe the MSCs morphology on different culture surfaces (Figure 25). SEM images indicated that CA scaffolds (CA and CA+A) promoted spherical morphology of MSCs, which maintain multipotency and promote differentiation efficiency to osteogenic, chondrogenic, and adipogenic lineages [148, 149], while 2D samples had flat monolayers of cells.

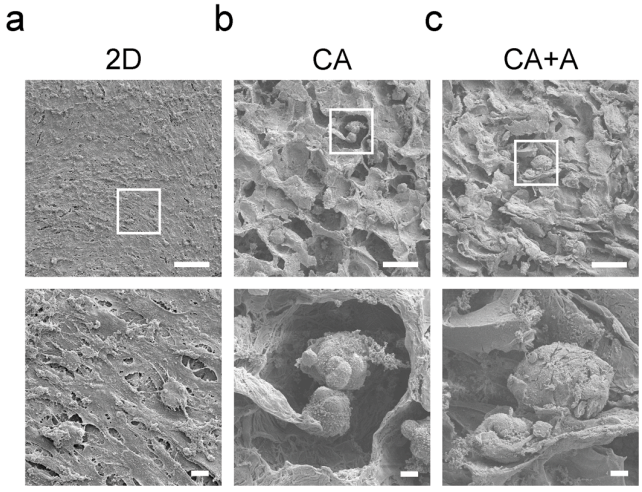

Figure 25. SEM images of MSCs cultured on different substrates. MSCs on 2D culture plates, CA scaffolds, and CA scaffolds + alginate gel (CA+A) at 7 days, scale bars are 100 μm and 10 μm. The bottom row shows magnified views of top row images.

8.3.3. Calvarial Defects

The efficacy of CA scaffolds for functional bone tissue engineering was evaluated in critical size calvarial defects in Sprague-Dawley rats. Different defect sizes (4, 5, and 8-mm diameter) have been indicated as critical-sized cranial defects in rats and we used a 5-mm diameter defect as it was the largest that could be placed entirely on one side of the calvarium. Harvested samples were evaluated with MicroCT to characterize defect closure (Fig. 26). At 4 weeks, MicroCT imaging demonstrated defect closure in the experimental groups with CA (25.65 ± 5.25%), CA+MSC (27.87 ± 18.88%), CA+BM (26.18 ± 14.99%), and CA+BMP-2 (48.08 ± 14.95%) samples compared to control defects (1.33 ± 2.31%) (Figure 26a-e), with a statistically significant difference ($p \leq 0.05$) between the CA+BMP-2 and control samples (Fig. 26f). At 16 weeks, MicroCT imaging demonstrated greater defect closure in the experimental samples than at 4 weeks (Fig. 26b-e), with CA+BMP-2 samples having the greatest defect reduction (71.56 ± 19.74%), followed by CA+MSC (57.92 ± 18.69%), CA+BM (39.60 ± 19.07%), CA (33.69 ± 11.71%), and control samples (2.00 ± 2.00%). There was a statistically significant difference ($p \leq 0.05$) between CA+BMP-2 and control samples and CA+MSC and control samples (Fig. 26g). The use of CA scaffolds both natively and supplemented with cells or

growth factors improved defect closure compared to empty defects. Use of live MicroCT imaging would allow the same samples to be imaged throughout the trial and provide defect closure data with less sample-to-sample variation.

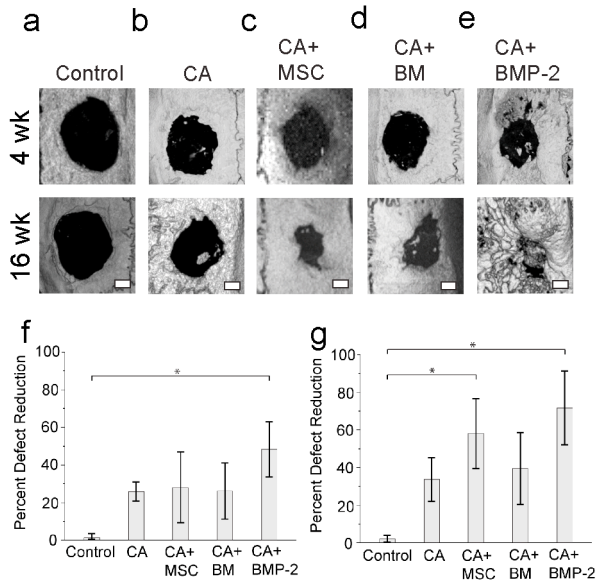

Figure 26. MicroCT 3D reconstruction images of *in vivo* samples at 4 and 16 weeks. Samples include: (a) control, (b) CA, (c) CA+MSC, (d) CA+BM, and (e) CA+BMP-2. Scale bars are 1 mm. (f) Percent defect reduction at 4 weeks and (g) 16 weeks, * denotes $p \leq 0.05$ statistically significant difference, n = 3.

Histologic analysis was performed on 16-week samples with H&E and Masson's trichrome staining. In the control group defects were filled with fibrous connective tissue with no evidence of osteoid formation (Figure 27a). In contrast, osteoblasts are seen with islands of osteoid in the experimental groups (CA, CA+MSC, CA+BM, and CA+BMP-2) (Figure 27b-e). Osteoblasts (Ob) were identified by their cuboidal morphology and lining regions of immature woven bone as well as bony ossicles (Figure 27b-e), although osteoblasts, osteoid, and bone should be verified by specific stains. In Masson's trichrome stain, blue staining is indicative of collagen, which is seen in both fibrous connective tissue and osteoid. Intramembraneous bone formation was observed in all experimental groups with clusters of osteoblasts surrounding osteoid tissue (Figure 28). Mature lamellar bone and bridging trabecula were only observed in

the CA+BMP-2 samples (Figures 27e and 28e), indicating the contribution of osteogenic growth factors.

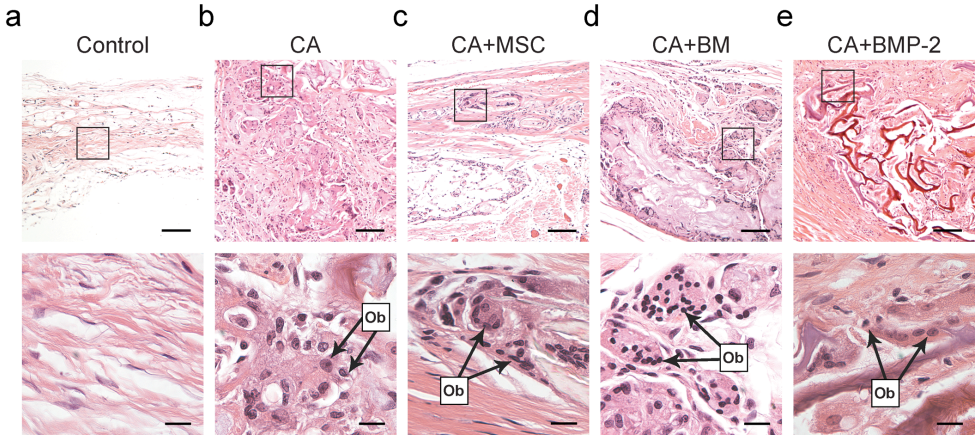

Figure 27. H+E staining of 16-week *in vivo* samples. Samples include: (a) control, (b) CA, (c) CA+MSC, (d) CA+BM, and (e) CA+BMP-2. Black stain denotes cell nuclei, with osteoblasts (Ob) labeled. Scale bars are 100 μm (top) and 10 μm (bottom).

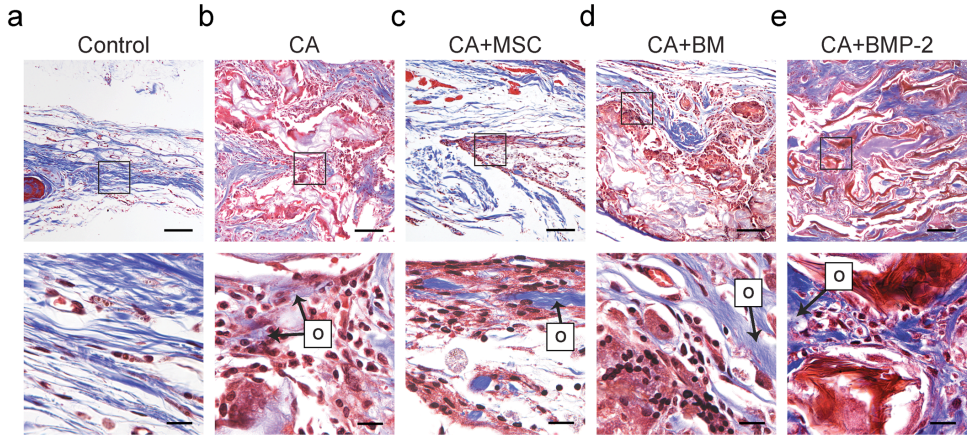

Figure 28. Masson's trichrome-stained 16-week *in vivo* samples. Samples include: (a) control, (b) CA, (c) CA+MSC, (d) CA+BM, and (e) CA+BMP-2. Black stain denotes cell nuclei and blue stain denotes collagen. Deposited osteoid (blue) is labeled with "O." Scale bars are 100 μm (top) and 10 μm (bottom).

Von Kossa staining was used to indicate mineralization (black) in the samples (Figure 29a-e). All samples had mineralization, with increasing mineral deposits in the experimental samples. The control samples showed isolated regions of mineralization among fibrous tissue. The presence of mineral deposits in the native CA scaffold indicates its osteo-conductivity. The CA+MSC and CA+BM samples showed considerably thicker and denser regions of

mineralization than did the CA samples. The CA+BMP-2 samples exhibited the greatest amount of mineralization characterized by large, dense mineral deposits, indicating the effect of BMP-2 in promoting osteogenesis. Semi-quantitative percent mineralization results (Figure 29f) indicated increasing mineralization among samples as follows: control, CA, CA+MSC, CA+BM, and CA+BMP-2 (3.19 ± 0.93%, 7.63 ± 0.45%, 11.01 ± 0.79%, 21.42 ± 4.01%, and 32.82 ± 3.71%, respectively). Statistically significant differences ($p \leq 0.05$) were reported between the CA+BM and CA+BMP-2 sample groups and the other groups (control, CA, and CA+MSC). Evaluation of mineralization corroborated the degree of defect closure observed in MicroCT analysis, except for CA+MSC samples, and illustrated how the treatments influenced the quality of defect repair.

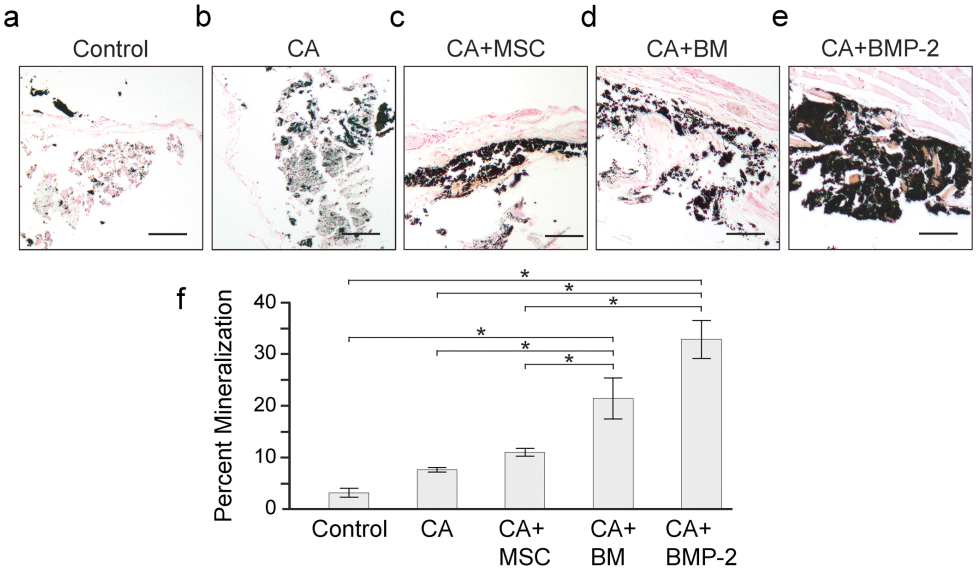

Figure 29. Von Kossa staining of 16-week *in vivo* samples. Samples include: (a) control, (b) CA, (c) CA+MSC, (d) CA+BM, and (e) CA+BMP-2; black stain denotes deposited bone mineral, scale bars are 100 μm. (f) Comparison of percent mineralization, * denotes $p \leq 0.05$ statistically significant difference, n = 3.

Osteocalcin and osteopontin, two non-collagenous osteoid proteins, are markers for the mature osteoblast phenotype and are involved in bone mineral deposition, with osteopontin found in both woven and lamellar bone, while osteocalcin is found specifically in lamellar bone [28, 30]. The co-localization (yellow color in Figure 30a-e) of osteocalcin (red) and osteopontin

(green) at 16 weeks *in vivo* confirms the presence of osteoid, indicated with the other histology stains. The control samples show very little osteocalcin and osteopontin deposits, while CA and CA+MSC samples show localized deposits, and CA+BM and CA+BMP-2 samples show greater deposits of osteocalcin and osteopontin, which correlates with the histological analysis. Relative fluorescence intensity for the samples based on a high-power field is shown in Figure 30f and 30g. Semi-quantitative analysis of osteocalcin expression (Figure 30f) indicates a statistically significant difference ($p \leq 0.05$) between CA+BMP-2 and control, CA, and CA+MSC samples. Differences in osteopontin expression (Figure 30g) were statistically significant ($p \leq 0.05$) between CA+BMP-2 and control, CA, and CA+MSC samples and also between CA+BM and control samples. Osteoid deposition was elevated compared to control by treatment with CA scaffolds, cells, and BMP-2. No trace of CA materials was visible, suggesting that CA scaffolds were degraded in 16 weeks.

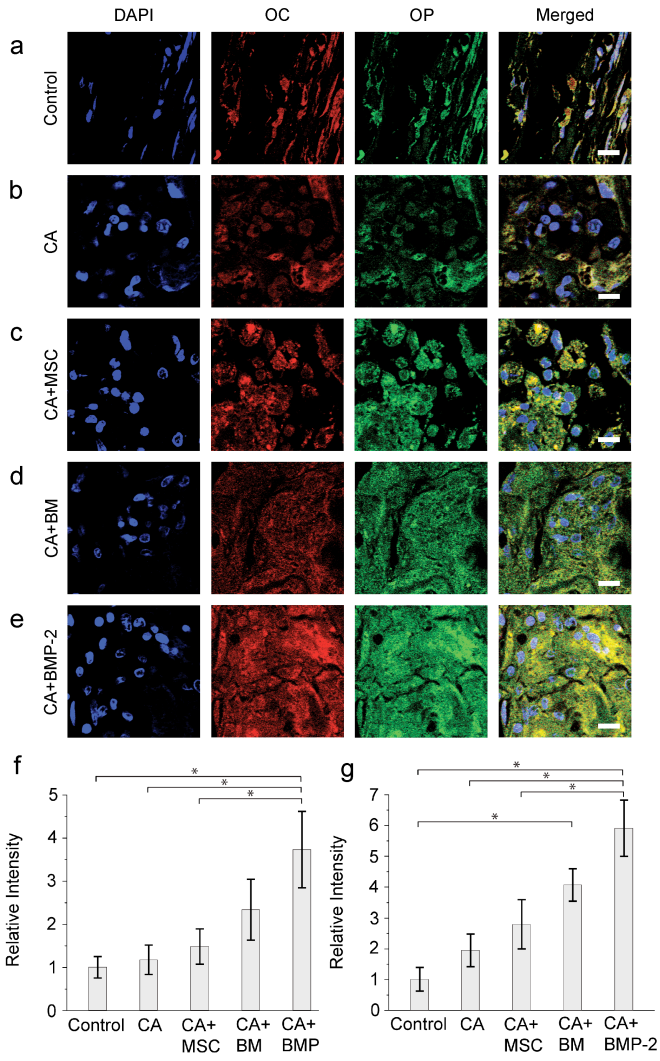

Figure 30. (a) Osteocalcin (OC, red) and osteopontin (OP, green) immunostained 16-week *in vivo* samples; DAPI counterstain indicates cell nuclei, yellow color indicates co-localized OC and OP. Samples include: (a) control, (b) CA, (c) CA+MSC, (d) CA+BM, and (e) CA+BMP-2, scale bars are 10 μm. Relative fluorescent intensity of osteocalcin (f) and osteopontin (g) samples; * denotes $p \leq 0.01$ statistically significant difference, n = 3.

Many studies have evaluated different biomaterial and biological treatments in calvarial defect models but often these results appear to be correlated to the amount of BMP-2 or other growth factors delivered to the defect site [47, 150, 151]. Use of a low dose of BMP-2 in an alginate gel provided the greatest defect closure among sample groups. The CA scaffold was osteoconductive, which is an improvement over synthetic polymeric scaffolds that are not osteoconductive nor osteoinductive [42]. While the study indicated that CA scaffolds and the

evaluated treatments promote osteogenesis, further optimization of sample conditions is needed for complete defect closure. Using greater BMP-2 doses (500 ng to 5 μg per scaffold) delivered by alginate gel could enhance defect closure. MSCs could be osteogenically differentiated prior to or after seeding on CA scaffolds *in vitro*. Viability of MSCs and bone marrow aspirate could be tested prior to implanting the scaffolds, especially if adding *in vitro* culture to the procedure. Implanting the scaffold in the defect plane instead of tucking it under defect margins could improve defect closure and bone formation. Use of differentiated MSCs, increased BMP-2 doses, or combination of MSCs and BMP-2 would enhance the scaffold's osteogenic potential, possibly leading to full calvarial defect repair.

8.4. Conclusions

In this study we demonstrated the use of 3D porous CA scaffolds for bone defect repair in a critical size rat calvarial defect model. *In vitro* trials demonstrated that CA scaffolds supported MSCs growth and promoted spherical morphology instead of monolayers. The native CA scaffold was osteoconductive and experimental treatments improved defect closure. This is the first use of a 3D porous CA scaffold in a calvarial defect model. The CA scaffold is readily shapeable to fit defect size before surgery, degradable in 16 weeks *in vivo*, can be produced in larger sizes to treat large bone defects, and at low cost in production. These results suggest that CA scaffolds could be used for repair of bone defects and functional bone tissue engineering applications, especially with pediatric patients. Further trials to optimize scaffold treatment conditions, including use of osteogenically differentiated MSCs, increased BMP-2 concentrations, and combination of MSCs and BMP-2 may further enhance osteogenesis.

9. 3D Porous Chitosan–Alginate Scaffolds for Enrichment of Cancer Stem Cell Population in Human Gliomas

Emerging evidence implicates cancer stem cells (CSCs) as primary determinants of the clinical behavior of human cancers. CSCs are difficult to propagate in vitro, greatly limiting the study of CSC biology. Here we report that growing cells from monolayer cultures of glioblastoma (GBM) cell lines on three-dimensional (3D), porous chitosan-alginate (CA) scaffolds promotes the proliferation of cells possessing the hallmarks of CSCs, including expression of neural stem cell markers. More importantly, scaffold-grown cells were more tumorigenic in nude mouse xenografts than were cells grown in monolayers. Preliminary results indicate that binding to CA scaffolds rapidly promotes expression of genes that participate in the epithelial-to-mesenchymal transition (EMT) and have been implicated in the genesis of CSCs. Our results indicate that CA scaffolds have utility as a simple and relatively inexpensive means to cultivate CSCs *in vitro* in support of studies to develop novel therapies that more effectively target CSCs.

9.1. Introduction

CSCs constitute a minority subpopulation of tumor cells characterized by the capacity for self-renewal and unlimited proliferation, and the ability to give rise to tumor cells with a more differentiated phenotype (Reviewed in [152-155]). Compared to the majority of cells in a tumor, CSCs are more malignant as evidenced by greater invasiveness, metastatic potential, and resistance to standard therapeutic interventions. These findings indicate that CSCs are primary determinants of tumor clinical behavior, making them attractive targets for novel, more efficacious treatments. Drugs that can eradicate the CSC population in a tumor would likely be a highly effective therapy. However, development of drugs specific for CSCs is hindered by the difficulty in isolating and propagating these cells *in vitro* since they represent such a small proportion of the total cells in tumor tissue and in monolayer cultures of tumor cell lines [156].

The most common method for isolating CSCs uses fluorescence-activated (FACS) or magnetic-activated (MACS) cell sorting of cells bound with antibodies specific for CSC surface

markers (e.g., $CD133^+$, prominin-1) [156]. This approach requires costly antibody and expensive, dedicated equipment, and yields low numbers of viable cells for subsequent study. CSCs can also be isolated and propagated *in vitro* using serum-free, defined media as suspension cultures of tumorspheres [155]. However, tumorsphere growth is slow, requires large volumes of expensive specialized media, and frequently is not successful due to the small percentage of CSC cells in the tumor of origin [155]. A major limitation of suspension cultures is the absence of a three-dimensional (3D) environment required for cell-extracellular matrix interactions that facilitate proliferation and promote malignancy [101]. Assays employing soft agar or agar microbeads have been used to grow isolated CSCs, but collection and subsequent analysis of cells is impaired by the high density and small pore sizes typical of polymerized agar [157].

We previously demonstrated that human glioblastoma (GBM) and hepatocellular carcinoma cell lines cultured on 3D CA scaffolds develop a more malignant phenotype, evidenced, in part, by increased tumorigenicity in nude mice, than do those cultured as monolayers. We attributed the greater malignant potential of scaffold-grown cells to the presence of local structures in the CA matrix that mimic *in vivo* CSCs niches [103, 104]. This conclusion is in accord with observations that the tumor microenvironment has a significant effect on the maintenance and self-renewal of CSCs [158], and with our previous report that CA scaffolds support the proliferation of human embryonic stem cells [134]. Here we investigated the ability of CA scaffolds to promote the isolation and proliferation of the CSCs from monolayer cultures of GBM cell lines. Notably, our results indicate that growth on scaffolds is accompanied by changes in gene expression, suggesting dedifferentiation to a more primitive phenotype characteristic of CSCs.

9.2. Materials and Methods

9.2.1.Cell Lines and Tissue Culture

The human cell lines U-87 MG and U-118 MG (glioblastoma), MDA-MB-231 (breast carcinoma), SK-Hep-1 (hepatocellular carcinoma), and the mouse prostate carcinoma line TRAMP-C2 were purchased from American Type Culture Collection, as was Minimum

Essential Media (MEM). Cells were maintained according to manufacturer's instructions in MEM containing 10% FBS (Atlanta Biologicals) and 1% antibiotic–antimycotic (Invitrogen) at 37°C and 5% CO_2 in a fully humidified incubator. Anti-human/mouse/rat CD133 primary antibodies (rabbit polyclonal to CD133) and FITC-conjugated goat polyclonal secondary antibodies to rabbit IgG were purchased from Abcam.

9.2.2. CA Scaffold Synthesis

Chitosan (practical grade, >75% deacetylated, MW = 190,000–375,000) and sodium alginate (alginic acid from brown seaweed) powders were purchased from Sigma-Aldrich and used without additional purification. CA scaffolds were prepared as previously reported [103, 104, 146]. Briefly, a solution of 4 wt% chitosan and 2 wt% acetic acid was mixed under constant stirring for 7 minutes to obtain a homogeneous solution. A 4 wt% alginate solution in deionized water was then added and mixed for 10 minutes, followed by constant mixing in a blender for 5 minutes to obtain a homogeneous CA solution. Approximately 3–4 ml of the CA solution was cast in 24-well cell culture plates and frozen at −20°C overnight. The samples were then lyophilized, sectioned into 2-mm thick, 13-mm diameter disks, then crosslinked with 0.2 M $CaCl_2$ for 10 minutes under vacuum, washed with deionized water several times to remove any excess salt, and sterilized in 70 v% ethanol for 2 hours under vacuum. The scaffolds were then washed three times with sterile PBS and placed on an orbital shaker for at least 12 hours to remove any excess ethanol.

9.2.3. Cell Seeding on Scaffolds

Cells were seeded onto PBS damp CA scaffolds in 12-well plates at 50,000 cells per scaffold in 50 μL of supplemented medium. Cells were allowed to attach to the scaffold for 1 hour before adding 1 mL of medium to each well. For PCL and PS scaffolds, 50,000 cells were seeded per scaffold following the manufacturer's protocol. For 2D cultures, 12-well plates were inoculated with 1 mL medium containing 50,000 cells. Medium were replaced every 2 days or as required.

9.2.4. Cell Proliferation Analysis

Cell proliferation was determined using the alamarBlue assay following the manufacturer's protocol. Briefly, cells were washed with PBS before adding 1 mL of alamarBlue solution (110 µg Resazurin per 1 mL medium) to each well. After continuing incubation for 1.5 hours, the solution was transferred to a black-bottom 96-well plate to measure fluorescence. The cell number was calculated based on standard curves created for each cell line grown as monolayers. For time course determinations, cells were washed with D-PBS to remove alamarBlue and returned to fresh medium

9.2.5. Scanning Electron Microscopy

Samples in medium were fixed with 2.5% glutaraldehyde for 30 minutes at 37°C, followed by incubation in 2.5% glutaraldehyde in 0.1 M sodium cacodylate buffer overnight at 4°C. After dehydration by serial washing in increasing ethanol concentrations (0%, 30%, 50%, 70%, 85%, 95%, 100%) with each wash performed twice, samples were critical-point dried, sectioned, mounted, and sputter coated with platinum before imaging with a JSM-7000 SEM (JEOL).

9.2.6. Flow Cytometry Analysis

Cells were detached from scaffolds with Versene and washed into FACS buffer (2% FBS in D-PBS) at 1 million cells per mL. Cells were incubated with primary antibody (1:50) for 1 hour on ice, washed thrice with FACS buffer, and incubated with FITC-conjugated secondary antibody (1:1000) for 30 minutes on ice and washed thrice with FACS buffer. Secondary-only stained cells were used as a background control. Cells were analyzed on a FACSCanto flow cytometer (Beckton Dickinson), and data processed using the FlowJo package (Tree Star).

9.2.7. Immunostaining

Cell-cultured scaffolds were fixed overnight in 4% formaldehyde, embedded in paraffin, sectioned into 15-µm sections, and affixed to slides. Slides were deparaffinized with xylenes and rehydrated followed by antigen retrieval using a double boiler and Tris-based antigen retrieval buffer. Slides were blocked with 10% BSA for 2 hours and incubated with primary antibody

(1:100) overnight at 4ºC. For immunofluorescence imaging slides were washed thrice with 10% BSA before incubation with FITC-conjugated secondary antibody for 2 hours at 4ºC (1:1000 dilution in 10% BSA). Slides were mounted using Prolong Gold anti-fade reagent containing DAPI as a counter stain to visualize cell nuclei. Images were obtained on an inverted fluorescent microscope (Nikon Instruments) with the appropriate filters using a Nikon Ri1 Color Cooled Camera System (Nikon Instruments) and 60× Oil Objective Lens (Nikon Instruments). For immunohistochemistry, slides were sequentially incubated with biotinylated secondary antibody, peroxidase-labeled avidin, and diaminobenzidine (DAB)/hydrogen peroxide chromogen substrate and counterstained with hematoxylin before mounting.

9.2.8. PCR

Cells were detached from samples with versene and cell pellets stored at -80ºC before RNA extraction using the Qiagen RNeasy kit (Qiagen) following the manufacturer's protocol. Following reverse transcription (iScript cDNA synthesis kit, Bio-Rad), DNA transcripts were probed using BioRad iQ SYBR Green Supermix with the primers listed in Table II. PCR used a BioRad CFX96 Real-Time Detection System and expression levels normalized to GAPDH.

Table II. Primers used for qPCR.

Target	Forward (5'-3')	Reverse (5'-3')	Product length (bp)
GAPDH	AAGGTCGGAGTCAACGGATTTGGT	ACAAAGTGGTCGTTGAGGGCAATG	911
CD133	TGGAGAACATTCTTCCGCATCCCT	AATCACGCGGCTGTACCACATAGA	395
NES	AGACACCTGTGCCAGCCTTTCTTA	CTGCTGCAAGCTGCTTACCACTTT	470
GFAP	CAGCAACATGCATGAAGCCGAAGA	AGAATAAAGCAGAGAGCCTGGCGT	903
FZD4	CTTGTTCATTGCCGCTGGACTTGT	CATGACGTCAAAGCCTGGCACAAT	701
GLI1	CACACAAGTGCACGTTTGAAGGGT	AGCATATCTTGCCCGAAGCAGGTA	884
HES1	TCTGAAGAAAGATAGCTCGCGGCA	ACCTGGAAGCCTCCAAACACCTTA	471
SNAI1	GCTCGAAAGGCCTTCAACTGCAAA	AGGCAGAGGACACAGAACCAGAAA	531
SNAI2	TTTCTGGGCTGGCCAAACATAAGC	TGCAAATGCTCTGTTGCAGTGAGG	251
TW1	AGCTGAGCAAGATTCAGACCCTCA	AGAATGCAGAGGTGTGAGGATGGT	452
TW1	GCAAGAAATCGAGCGAAGATGGCA	TTCCAGGCTTCCTCGAAACAGTCA	871
Notch1	AGATCAACCTGGATGACTGTGCCA	TCAATACACGTGCCCTGGTTCAGA	508
BMPR2	ACCATGAATGGTGTGGCAGGTAGA	ATGGTTGTAGCAGTGCCTCCTTCT	671
N-cadherin	ACAGATGTGGACAGGATTGTGGGT	GAGCCCAAATTGGTTTGCAGCCTA	743
E-cadherin	AGATGACACCCGGGACAACGTTTA	TCGGAACCACTGCCTTCGTAATCA	288
CD44	TCGAAGAAGGTGTGGGCAGAAGAA	ATTTCCTGAGACTTGCTGGCCTCT	111
FN1	AAACTTGCATCTGGAGGCAAACCC	TTCTCCTGCCGCAACTACTGTGAT	388
VIM	AGAACCTGCAGGAGGCAGAAGAAT	CTTCCATTTCACGCATCTGGCGTT	201
NANOG	CTTGCCTTGCTTTGAAGCATCCGA	TCTGTTTCTTGACCGGGACCTTGT	260

9.2.9. Tumorigenesis Assay

Cells cultured on CA scaffolds for 15 days were detached using Versene, and immunostained for CD133 as described above. $CD133^{+}$ and $CD133^{-}$ cells were sorted into PBS containing 2% FBS using an Aria flow cytometer (Beckton Dickinson). Cells (500 or 2000) were injected subcutaneously into the flanks of athymic nude mice (Charles River Labs) of 6 to 8 weeks of age. All animal experiments were conducted in accordance with UW Internal Animal Care and Use Committee approved protocols. For unsorted cell tumor growth studies, scaffolds containing cells cultured for 10 days were implanted into the flanks of athymic nude mice. Two-dimensional cultured cells were implanted with growth factor-reduced Matrigel at the same cell number as cells on CA scaffolds. Tumors were measured using calipers and the volume was calculated using previously established methods [103, 104].

9.3. Results and Discussion

Human U-118 MG GBM cells grown on CA scaffolds display pronounced differences in morphology and expression of CD133, a marker of GBM CSCs [159–161], compared to cells grown as monolayers. In accord with our earlier report (ref. [103]), scanning electron microscopy (SEM) revealed that growth on scaffolds produced aggregations of spherical- or ovoid-shaped cells while growth in monolayer yielded sheets of flat, epithelioid cells with numerous, extended processes (Figure 31a). Similar differences in cellular morphology were also observed for the human GBM line U-87 MG (Figure 37a; ref. [103]) and for human liver and breast and mouse prostate cancer cells (Figure 32). As illustrated in Figure 31b, growth on CA scaffolds for 15 days was accompanied by a 70-fold increase in the fraction of CD133 immunopositive U-118 MG cells. In contrast, the fraction of $CD133^{+}$ cells in monolayer cultures (~1%) was unchanged in this interval. Notably, CD133 mRNA abundance in U-87 MG was 12-fold higher in cells grown on scaffold compared to monolayers (Figure 31c), suggesting that scaffolds stimulate *de novo* CD133 gene expression rather than the acquisition of a spherical morphology exposing

occult CD133 protein on the cell surface. Comparable differences in CD133 immunopositivity and CD133 mRNA expression were also observed between scaffold- and monolayer-grown liver, breast, and prostate cancer cell lines indicative of the growth of CSCs from these lines [156, 162–165] (Figures 33 and 35). Moreover, scaffold-grown liver, breast, and prostate cancer cell lines displayed greater abundance of mRNA for *NANOG* (Fig. 34), a transcription factor essential for self-renewal expressed in undifferentiated embryonic stem cells and CSCs [166, 167]. Finally, examination of U-118 MG CD133 immunopositivity in fixed, paraffin-embedded sections of scaffold revealed that the intensity of immunostaining increased with the size of the tumor cell clusters (Figure 31d-g). As shown in Figure 31d, solitary cells expressed no detectable CD133 protein. However, the intensity of immunostaining of individual cells increased as clusters grew in size. Notably, a large majority of cells in the large clusters were CD133 immunopositive (Figure 31g), supporting our conclusion that growth on scaffolds enriches the proportion of $CD133^+$ CSCs.

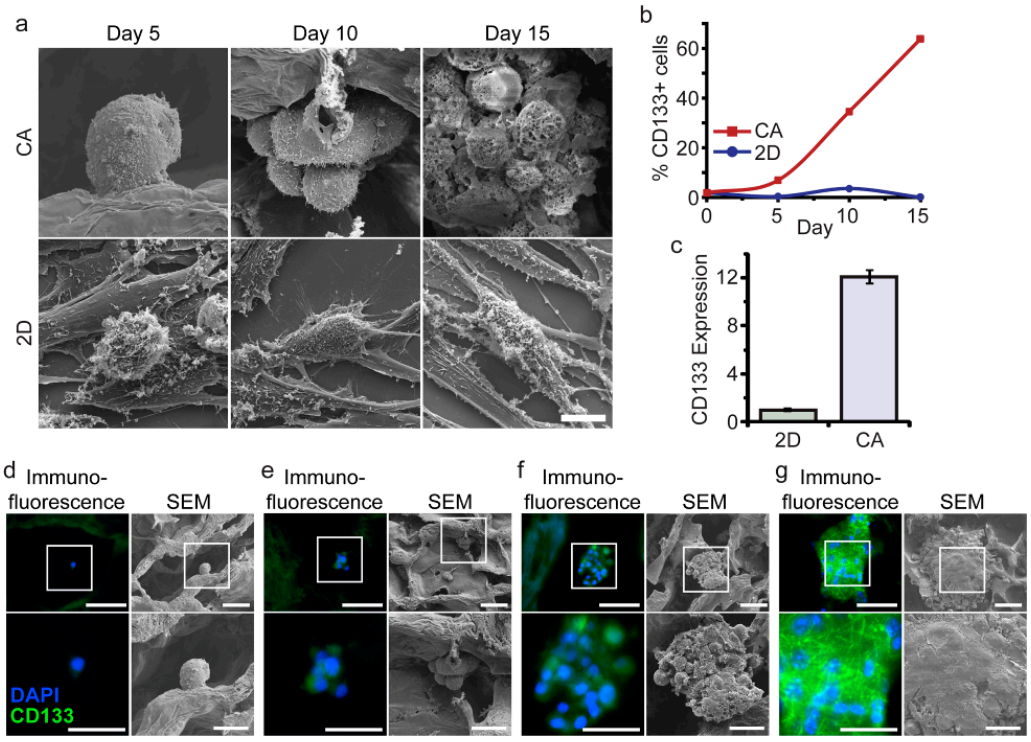

Figure 31. Growth of CD133· GBM cells on CA scaffolds. (a) SEM images comparing the morphology and proliferation of human U-118 MG GBM cells cultured on CA scaffolds or as monolayers. Scale bar corresponds to 10 µm. Cells were seeded directly in 6-well plates containing 22 × 22 mm cover slips (2D condition) or 12-well plates containing CA scaffolds (CA condition) at 50,000 cells per scaffold or per well using fully supplemented culture media. After 5, 10, and 15 days of culture, cells were fixed, dehydrated, and super-critically dried for SEM imaging. (b) Comparison of the change in fraction of CD133· U-118 MG cells grown for 15 days on CA scaffolds or as monolayers. Immunopositivity for CD133 was determined by flow cytometry. (c) CD133 mRNA content determined by real-time PCR in U-87 MG GBM cells grown for 10 days on CA scaffolds compared to that of monolayer cultures. CD133 mRNA content was normalized to the 2D condition. (d-g) Immunostaining for CD133 (green) and SEM imaging of CA scaffold-cultured human U-118 MG GBM cells at day 10. Blue color reflects DAPI counter-staining of nuclei. (d) Solitary U-118 MG cells generally showed no CD133 staining. (e) Small clusters of U-118 MG cells showed faint staining for CD133 staining. (f and g) Intensity of staining for CD133 increases as clusters of U-118 MG cells grow larger. The boxed regions in the top-row images correspond to the areas of the bottom images. Scale bars for panels d-g correspond to 50 µm for the upper row and 25 µm for the lower row.

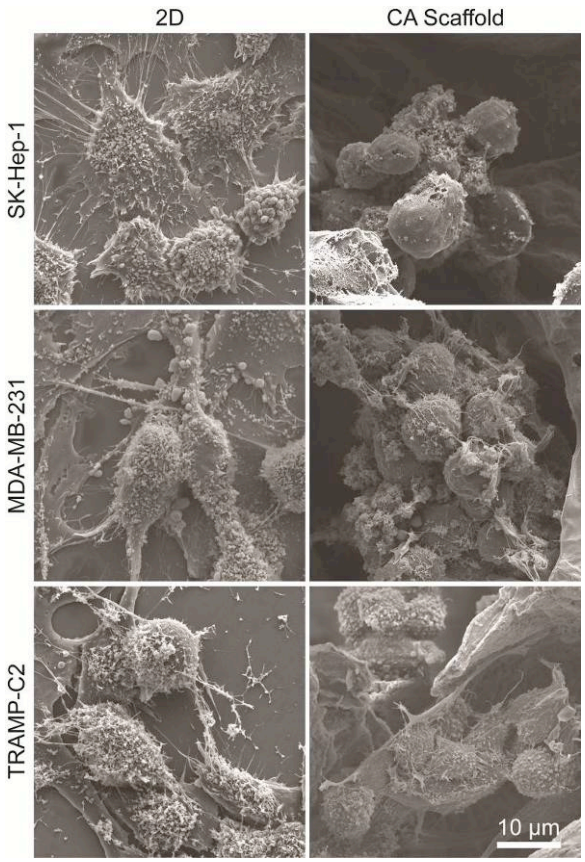

Figure 32. SEM images comparing the morphology of SK-Hep-1 (liver), MDA-MB-231 (breast), and TRAMP-C2 (prostate) cancer cells grown as monolayers or on CA scaffolds.

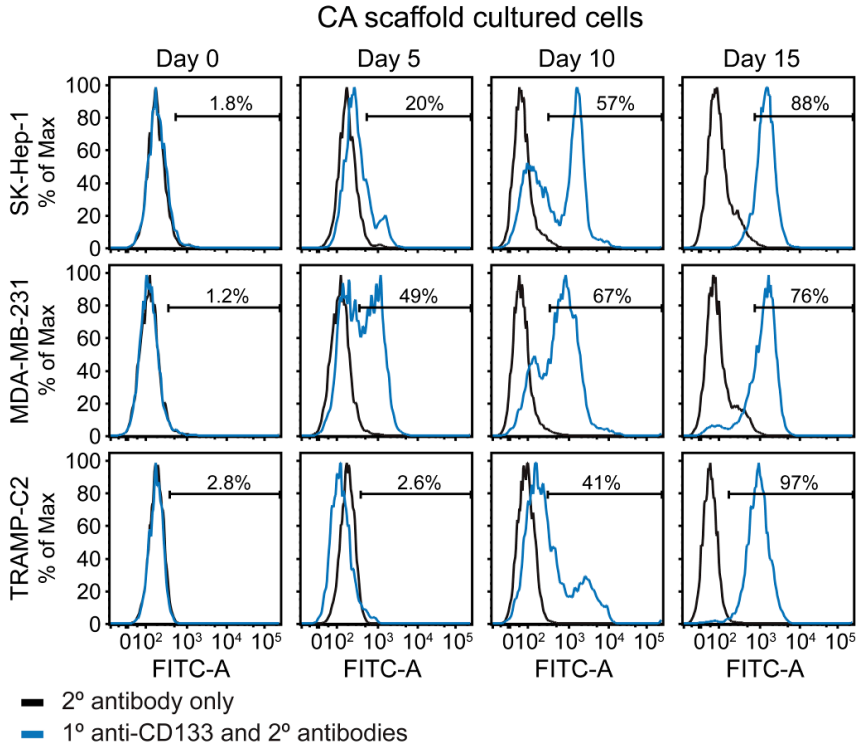

Figure 33. Flow cytometry histograms showing the increase in immunopositivity for CD133 of SK-Hep-1 (liver), MDA-MB-231 (breast), and TRAMP-C2 (prostate) cancer cells as they grow on CA scaffolds.

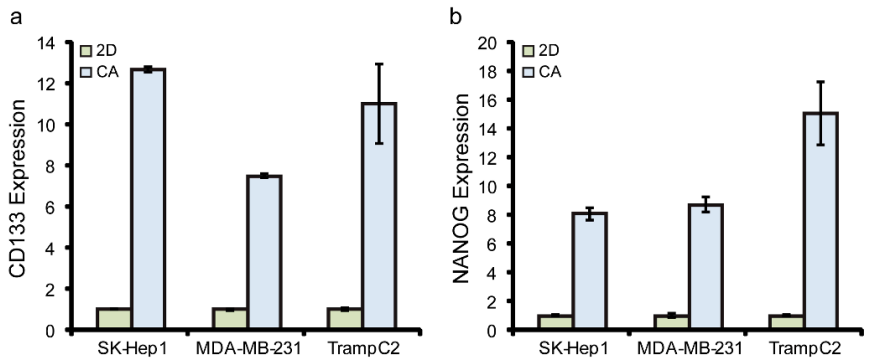

Figure 34. Greater expression of mRNA for the stem cell markers CD133 (a) and NANOG (b) in SK-HEP-1 (liver), MDA-MB-231 (breast), and Tramp-C2 (prostate) cancer cells grown for 10 days on CA scaffolds compared to cells grown as monolayers.

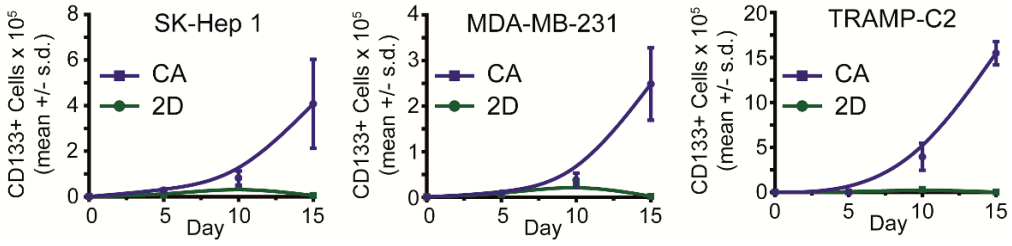

Figure 35. Comparison of growth of CD133- SK-Hep-1 (liver), MDA-MB-231 (breast), and TRAMP-C2 (prostate) cancer cells as monolayers (green) or on CA scaffolds (blue).

Considerable evidence indicates that transformation of normal neural stem cells underlies the genesis of GBM and is accompanied by the aberrant expression of genes that promote the normal development of neural cells [168]. We therefore compared the expression of mRNA for a panel of genes found in normal neural progenitor cells in scaffold and monolayer cultures of U-118 MG. Ten days after inoculation, cells harvested from scaffolds showed a 4-fold higher abundance of mRNA for nestin, a cytoskeletal protein specific to neural progenitor cells [168], compared to monolayer cells (Figure 36a). In contrast, scaffold-grown cells showed no increase in mRNA expression for GFAP, a cytoskeletal protein that replaces nestin as neural progenitors differentiate into mature glial cells [168]. As shown in Figure 36b, growth on scaffolds was accompanied by elevated expression of mRNA for other neural development genes that have been implicated in the genesis of GBM [169–172], including *Frizzled 4* of the WNT signaling pathway, *GLI* and *Snail* of the hedgehog pathway, *HES* of the Notch pathway. These data strongly indicate that growth of U-118 MG on scaffolds is accompanied by elevated expression of a host of genes characteristic of undifferentiated GBM CSCs.

CSCs are characterized by their ability to readily form tumors in nude mice [152–154]. As shown in Figure 36c, subcutaneous flank tumors were detectable earlier and grew to a larger size in animals inoculated with U-118 MG cells grown on scaffolds compared to those grown as monolayers. Notably, the tumors from scaffold-grown cells were also more likely to express CD133 (Figure 36d), indicating that the enhanced tumorigenicity of cells from scaffolds reflected expression and maintenance of the CSC phenotype. Notably, $CD133^+$ cells harvested from scaffolds readily formed tumors in all animals 9 weeks after injection with 500 or 2,000 cells, while animals injected with $CD133^-$ cells harvested from scaffolds formed no tumors

(Figure 36e and 36f). This more stringent test of tumorigenicity provides additional evidence that scaffold-grown CD133^{+} cells possess the hallmark properties of CSCs.

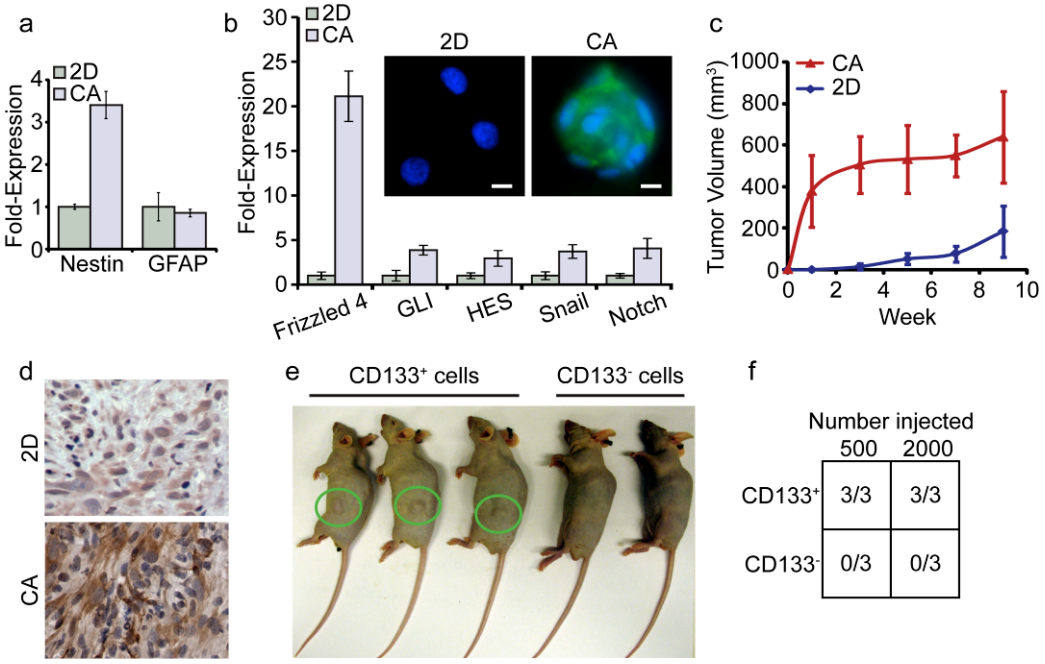

Figure 36. CA scaffold-grown U-118 MG GBM cells exhibit phenotypic characteristics of CSCs. (a) Determination of mRNA content by real-time PCR revealed that relative to monolayer cultures, cells grown on scaffolds show elevated expression of the neural progenitor intermediate filament nestin, while the level of mRNA for GFAP, the intermediate filament of mature glia, is unchanged. (b) Comparison of expression of mRNA of genes associated with normal neural cell development and the genesis of GBM in cells grown on scaffolds relative to cells grown as monolayers. Immunofluorescence images in inset show that enhanced protein expression (green) accompanied elevation of mRNA level for *frizzled-4*. Bar is 10 µm. (c) Size of flank tumors in nude mice injected subcutaneously with 50,000 cells grown on CA scaffolds or as monolayers. (d) Tumors from scaffold-grown cells display greater immunopositivity for CD133 (brown) than do tumors from monolayer cells. (e) Flank tumors in nude mice injected with 500 CD133^{+} or CD133^{-} U-118 MG glioblastoma cells sorted by FACS after culture in CA scaffolds. The tumors were evident only in mice injected with CD133^{+} cells. (f) Tumorigenicity in nude mice injected subcutaneously with either 500 or 2,000 FAC-isolated CD133^{+} or CD133^{-} cells grown on CA scaffolds for 10 days. Tumors grew only in all mice implanted with CD133^{+} cells.

To assess whether the enrichment of GBM CSCs is a consequence of growth on any 3D structure, we compared morphology and CD133 immunopositivity of the human glioma line U-87 MG cultured for 10 days on commercially available polycaprolactone (PCL) and polystyrene (PS) scaffolds with cells grown on CA scaffolds and as monolayers. As shown in Figure 37a, the morphology of U-87 MG cells grown on the commercial scaffolds differed little from that of

monolayer cells, in contrast to the clusters of spherical or ovoid cells on the CA scaffolds. Moreover, ~20% of cells on the CA scaffold were immunopositive for CD133 compared to 1% to 2% of cells grown on the other substrates (Figure 37b). The greater proliferation of U-87 MG CSCs grown on CA scaffolds compared to monolayer culture is illustrated in Figure 37c. After a delay of 5 days, U-87 MG CSCs grew rapidly on CA scaffolds through day 15. Comparable proliferation was also observed for CSCs from liver, breast, and prostate cell lines (Figure 35). By 15 days after inoculation the total number of U-87 MG $CD133^+$ CSCs increased 2000-fold while cells grown as monolayers showed negligible increase; comparable results were also observed for U-118 MG and for the liver, breast, and prostate cancer cell lines (Figure 38). These results indicate that the enrichment of $CD133^+$ cells on the CA scaffold reflects the chemistry of the substrate as well as its geometry and that culture on CA scaffolds is a facile method of producing large numbers of CSC for subsequent study.

The delay that precedes proliferation of $CD133^+$ CSCs observed above suggests that changes in gene expression are necessary for monolayer cancer cells to proliferate on CA scaffolds. Emerging evidence indicates that the pathway that mediates EMT in cancer can also promote reversion of non-CSC tumor cells to CSCs [173–175]. As illustrated in Figure 37e, EMT is mediated by signaling cascades induced by the interaction of the transmembrane glycoprotein CD44 with the extracellular matrix glycosaminoglycan hyaluronan (HA) [176, 177]. Activation of CD44 signaling is also associated with enhanced proliferation, invasion, and chemoresistance in cancer cells [177]. Importantly, HA is composed of alternating monomers of uronic acid and acetylglucosamine, the components of alginate and chitosan, respectively, and suggests that cancer cells grown on CA scaffolds may acquire a CSC phenotype via the EMT pathway. To address this question, we examined the expression of CD44 and other genes that participate in EMT in scaffold-grown U-87 MG cells. As shown in Figure 37f, CD44 mRNA content was elevated within a day of culture on scaffolds and remained elevated through day 6, although at a lower level than day 1. The decrease in CD44 expression after day 1 may be due to the formation of tumor spheres in which not every cell is in physical contact with the CA scaffold. Elevation of mRNA for *Twist2*, *Sna1* and *Sna2*, genes that participate in EMT [159, 173], was subsequently detected beginning at day 4, and was accompanied by increased expression of *CD133*. Another

hallmark of EMT, enhanced expression of the cell adhesion molecule N-cadherin accompanied by suppression of E-cadherin, occurred between days 5 and 10 (Fig. 37d). *In toto*, these findings strongly suggest that activation of at least some elements that participate in EMT accompany the increased proliferation of $CD133^+$ CSCs on CA scaffolds.

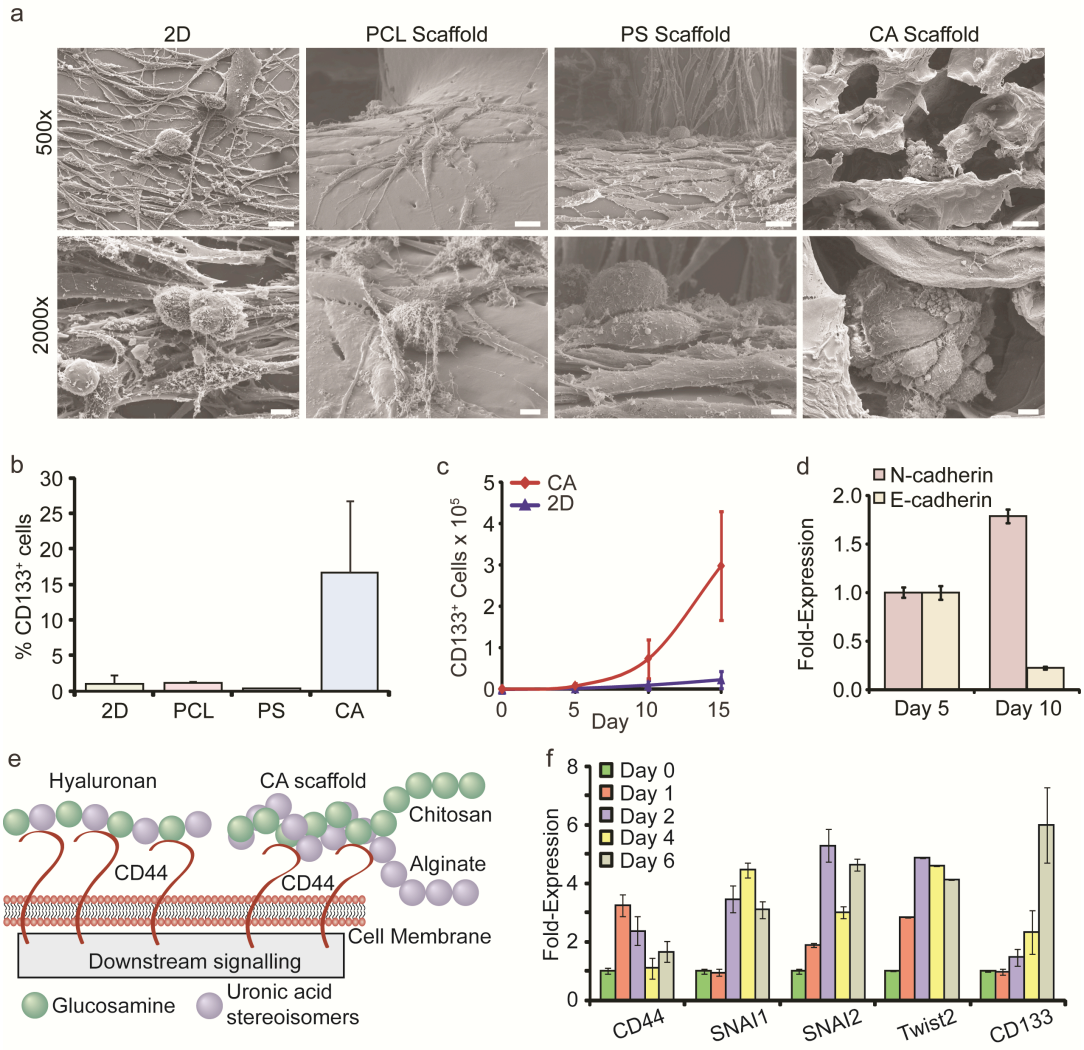

Figure 37. Proliferation of $CD133^+$ U-87 MG CSC GBM cells on CA scaffolds reflects expression of genes that mediate EMT. (a) SEM images of cells cultured in 2D plates, CA scaffolds, and commercially available polycaprolactone (PCL) and polystyrene (PS) scaffolds. Scale bars: 25 µm at 500× and 5 µm at 2000×. (b) Fraction of $CD133^+$ cells determined by flow cytometry after growth for 10 days as monolayers or on PCL, PS and CA scaffolds. (c) Growth curves for $CD133^+$ cells on CA scaffolds and in monolayer cultures. $CD133^+$ cell number was calculated by alamarBlue and flow cytometry. (d) Expression of N-cadherin and E-cadherin mRNA in scaffold-grown cell at day 5 and 10 determined by real-time PCR. (e) Putative mechanism for CSC enrichment in CA scaffolds. (f) Change in mRNA content for EMT-related genes and CD133 during growth on CA scaffolds for 6 days.

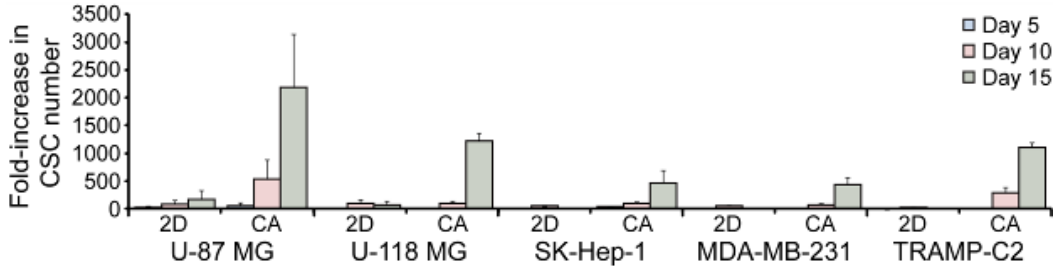

Figure 38. Fold-increase in CD133+ U-118 MG and U-87 MG (GBM), SK-Hep-1 (liver cancer), MDA-MB-231 (breast cancer), and Tramp-Cs (prostate cancer) cells grown as monolayers or on CA scaffolds.

In conclusion, we have shown that culturing GBM and other cancer cells previously grown as monolayers on CA scaffolds promotes the proliferation of cells expressing the hallmarks of CSCs. Acquisition of the CSC phenotype appears to be specific to the chemistry of CA and is mediated by expression of genes that mediate EMT. Significantly, this method rapidly produces large numbers of CSCs that can easily be collected for subsequent analysis without the use of defined media. CA scaffolds will facilitate the study of CSC biology and provide a new *in vitro* model for the discovery of more efficacious therapies targeting CSCs.

10. 3D Porous Chitosan–Alginate Scaffolds: New Matrix for Studying Prostate Cancer Cell–Lymphocyte Interactions In Vitro

The treatment of castration-resistant prostate cancer (CRPC) remains palliative. Immunotherapy offers a potentially effective therapy for CRPC; however, its advancement into the clinic has been slow, in part due to the lack of representative *in vitro* tumor models that resemble the *in vivo* tumor microenvironment for studying interactions of CRPC cells with immune cells and other potential therapeutics. This study evaluates the use of 3D porous chitosan–alginate (CA) scaffolds for culturing human prostate cancer (PCa) cells and studying tumor cell interaction with human peripheral blood lymphocytes (PBLs) *ex vivo*. CA scaffolds and Matrigel matrix samples supported *in vitro* tumor spheroid formation over 15 days of culture, and CA scaffolds supported live cell fluorescence imaging with confocal microscopy using stably transfected PCa cells for 55 days. PCa cells grown in Matrigel matrix and CA scaffolds for 15 days were co-cultured with PBLs for 2 and 6 days *in vitro* and evaluated with scanning electron microscopy (SEM), immunohistochemistry (IHC), and flow cytometry. Both the Matrigel matrix and CA scaffolds supported interaction of PBLs with PCa tumors, with CA scaffolds providing a more robust platform for subsequent analyses. This study demonstrates the use of 3D natural polymer scaffolds as a tissue culture model for supporting long-term analysis of interaction of prostate cancer tumor cells with immune cells, providing an *in vitro* platform for rapid immunotherapy development.

10.1. Introduction

Prostate cancer (PCa) is the most common and second deadliest cancer in men in the US with an estimated 217,730 new cases and 32,050 deaths in 2010 [6]. Castration-resistant prostate cancer (CRPC) represents the most deadly form of PCa; average survival is a dismal 2 to 3 years [178]. Even with front-line chemotherapy, disease progression occurs within 7 months for most patients [178]. Immunotherapy represents an ideal strategy for CRPC therapy since the body would use its natural defenses to actively destroy the cancer. Unfortunately, the rapid

development of effective immunotherapies has been hindered by the lack of *in vitro* tumor models that accurately mimic the human disease [179].

In cancer patients, the tumor escapes immunosurveillance-based cancer elimination through immunoediting [89, 180]. During this process, the cancer cells acquire mutations that allow them to evade recognition by immune cells and secrete signaling molecules into the tumor microenvironment and blood, which inactivate immune cells. In immunotherapy, the body's immune system is reactivated against antigens on the tumor cell surface either through immunological adjuvants or *ex vivo* activation of autologous peripheral blood lymphocytes (PBLs) that are injected back into the patient. Surprisingly, vaccine optimization usually occurs in small phase I/II clinical trials [181], which is likely due to the poor translation of *in vitro* efficacy to clinical response [179, 182, 183]. For example, sipuleucel-T (Provenge; Dendreon), the first autologous cellular immunotherapy for CRPC approved by the FDA, prolongs median survival of CRPC patients by only 4.1 months as compared to placebo [184]. The use of a representative model of the native tumor microenvironment *in vitro* will allow for better prediction of clinical response, which will reduce long-term costs associated with product development and generate higher quality therapeutics.

In vitro trials of activated PBL interaction with cancer cell suspensions or monolayers have shown high anti-cancer activity of immunotherapy. Activated PBLs show a high propensity for recognizing and eliminating target cancer cells. However, when the cancer cells are arranged in a three-dimensional architecture such as in tumor spheroids or 3D gel matrix, the activated PBLs show dramatically reduced affinity toward and cytotoxicity against target cancer cells [179, 182, 185–188]. Therefore, the development of 3D tissue culture models is expected to improve the relevance of *in vitro* immunotherapy results to clinical response by enhancing the ability to study the interaction of immune components with cancer cells and providing a platform for screening immunotherapies [179]. These *in vitro* trials using 3D tissue culture models could systematically identify tumor response to specific immune cells and reveal the components of the tumor microenvironment that aid in or inhibit immune therapies.

In this study, we investigated the use of 3D porous chitosan–alginate (CA) scaffolds to support the growth of PCa cells and formation of PCa tumor spheroids, and the feasibility of

using the 3D co-culture system to study the interaction between human PCa cells and PBLs. Chitosan and alginate are both natural polymers that are widely used in biomedical applications due to their excellent biological properties and limited immunogenicity [59]. Both chitosan and alginate have the proxy structure of glycosaminoglycans (GAGs) [59], a major component of the native extracellular matrix (ECM) [126]. The GAG hyaluronan, to which the CA complex is most chemically similar, makes up a significant portion of PCa ECM and promotes malignancy [189, 190]. The 3D porous CA scaffolds developed by our research group have served as an effective mimic of the tumor microenvironment for human glioblastoma and human hepatocellular carcinoma, and supported the culture of these cells with performance that better replicates the *in vivo* system compared to 2D and Matrigel cultures [103, 104].

Here human PCa cells (LNCaP, C4-2, and C4-2B) were seeded on Matrigel matrix and CA scaffolds and cultured *in vitro* for 15 days. The expansion of red fluorescent protein (RFP) expressing mouse PCa cells (TC2-RFP) in Matrigel matrix and CA scaffold samples was used to monitor *in situ* cell–cell interactions by confocal microscopy. After 15 days of *in vitro* culture, the Matrigel and CA scaffold human PCa samples were co-cultured with human PBLs for 2 and 6 days to observe the interaction of immune cells with PCa cells, and were characterized using SEM imaging, immunostaining, and flow cytometry.

10.2. Materials and Methods

10.2.1. Materials

All chemicals were purchased from Sigma-Aldrich unless otherwise indicated. Chitosan (practical grade, >75% deacetylated, MW = 190,000–375,000) and alginate (alginic acid from brown seaweed) were used as received. Reduced growth factor Matrigel matrix was purchased from BD Biosciences. RPMI Medium 1640, Dulbecco's Modified Eagle Medium (DMEM), antibiotic–antimycotic (AA), Dulbecco's phosphate-buffered saline (D-PBS), Versene and alamarBlue reagent were purchased from Invitrogen. Fetal bovine serum (FBS) was purchased from Atlanta Biologicals. LNCaP, C4-2, and C4-2B human PCa cell lines and TRAMP-C2 (TC2) mouse PCa cell lines were purchased from American Type Culture Collection. Human

PCa cells were maintained according to manufacturer's instruction in fully supplemented RPMI with 10% FBS and 1% AA at 37°C and 5% CO_2 in a fully humidified incubator. TC2 cells were transfected with pDsRed-Max-N1 (Addgene plasmid 21718, Addgene Inc.) plasmid using the Lipofectamine 2000 transfection reagent (Invitrogen) following the manufacturer's protocol. Cells stably expressing RFP were selected for neomycin resistance with G418 (1 mg mL^{-1}) in fully supplemented DMEM (10% FBS, 1% AA) for 2 weeks followed by FACS to obtain a pure population of TC2-RFP cells. TC2-RFP cells were maintained in fully supplemented DMEM containing 1 mg mL^{-1} G418 at 37°C and 5% CO_2 in a fully humidified incubator.

10.2.2. CA Scaffold Synthesis

CA scaffolds were prepared as previously reported [146]. Briefly, a 4 wt% chitosan solution was prepared by dissolving chitosan in 1 wt% acetic acid solution and a 4 wt% alginate solution was prepared by dissolving alginate in deionized (DI) water. Porous scaffolds were prepared by combining equal amounts of chitosan and alginate solutions and mixing for 10 minutes, followed by mixing under constant stirring for 5 minutes in a blender. The CA solution was cast in molds, refrigerated at 4°C for 12 hours, frozen at –20°C overnight, and lyophilized for 24 hours. The scaffolds were sectioned into 2-mm thick, 13-mm diameter discs, then crosslinked with a 0.2 M $CaCl_2$ solution for 10 minutes under vacuum, washed 3 times with excess DI water to remove any remaining salt, and sterilized in 70 v% ethanol for 2 hours under vacuum. The scaffolds were then washed 3 times with D-PBS, immersed in 500 mL D-PBS, and shaken on an orbital shaker at 100 rpm overnight to remove any remaining ethanol.

10.2.3. Cell Seeding on Scaffolds

PCa cells were seeded onto 12-well plate wells and D-PBS damp CA scaffolds in 12-well plates at 50,000 cells per sample in 100 μL fully supplemented media. The samples were incubated at 37°C and 5% CO_2 in a fully humidified incubator to allow cell adhesion to the substrate for 2 hours before 1.5 mL fully supplemented media was added to each well. For Matrigel cultured samples, 50,000 cells in 200 μL fully supplemented media were mixed with 200 μL Matrigel of reduced growth factor and added to 12-well plate wells. Samples were

incubated at 37°C and 5% CO_2 in a fully humidified incubator for 2 hours to allow the Matrigel matrix to gel before 1.5 mL fully supplemented media was added to each well. Matrigel and CA scaffold samples were cultured for 15 days with regular media changes. The RFP transfected cells (TC2-RFP) were seeded on CA scaffolds in the same manner shown above. The TC2-RFP Matrigel samples were seeded at a concentration of 50,000 cells in 50 μL fully supplemented media mixed with 150 μL Matrigel of reduced growth factor. The cells in CA scaffolds were cultured for up to 55 days with regular media changes.

10.2.4. Cell Proliferation Analysis

Proliferation of human PCa cells cultured on 2D wells, Matrigel matrix, and CA scaffolds was assessed with the alamarBlue assay following the manufacturer's protocol. Briefly, 1 mL of alamarBlue solution (10% alamarBlue reagent in fully supplemented RPMI 1640) was added to each well. The samples were incubated at 37°C for a predetermined time for each cell line (2.25 hours for LNCaP, 2.33 hours for C4-2, and 3 hours for C4-2B), then the alamarBlue solution was transferred to a 96-well plate to obtain fluorescence values using a microplate reader (Molecular Devices) at excitation wavelength of 570 nm and fluorescence emission read at 585 nm. The cell number was calculated based on previously created standard curves. Excess alamarBlue solution was aspirated and fresh fully supplemented media was added to each well.

10.2.5. Live Cell Imaging

TC2-RFP seeded Matrigel matrix and CA scaffold samples were transferred to 110-mm diameter Petri dishes customized for confocal microscopy (part of the dish bottom was removed and replaced with a coverslip). Media was added to the Petri dish to cover the substrate material and keep the cells viable. The samples were imaged with a confocal laser scanning microscope (Zeiss 510 META LSM, Carl Zeiss AG). The samples were imaged at 100× and 200× magnification with red fluorescence and DIC.

10.2.6. Human Peripheral Blood Lymphocytes (PBLs) Collection and Co-Culture

The study was carried out with the approval of the University of Washington Research Subjects Review Board and with informed signed consent. Blood samples were obtained from

healthy donors. Peripheral blood lymphocytes (PBLs) were separated from the whole blood by Ficoll gradient. Briefly, the blood sample was first diluted twice in sterile D-PBS and overlaid onto Ficoll-Paque PLUS (GE Healthcare), and soft spun at 2200 rpm for 20 minutes at room temperature without brake. PBLs were collected at the plasma/ficoll interface and washed once with D-PBS. Erythrocytes were lysed with ACK lysing buffer (BioWhittaker) and the remaining cells were washed twice with D-PBS in preparation for culture. The concentrated PBLs were resuspended in fresh RPMI media and added to Matrigel matrix or CA scaffold samples in a volume of 100 μL (2.5×10^5 PBLs per 100 μL). The PBLs were added to the samples after aspirating the culture media and were incubated for 1 hour before adding fresh fully supplemented RPMI media. The samples were cultured for 2 and 6 days and the media was changed regularly every second day.

10.2.7. SEM Imaging

Samples for scanning electron microscopy (SEM) analysis were fixed with 2.5% glutaraldehyde in fully supplemented media for 30 minutes at 37°C. The samples were then fixed in 2.5% glutaraldehyde in 0.1 M sodium cacodylate buffer overnight at 4°C. The samples were dehydrated in a series of ethanol washes (0%, 30%, 50%, 70%, 85%, 95%, 100%), with each wash performed twice. The samples were critical-point dried, sectioned, mounted, and sputter coated with platinum, then imaged with a JSM-7000F SEM (JEOL).

10.2.8. Immunohistochemical Staining

Samples were fixed in 4 w% formaldehyde, embedded in paraffin, and sectioned into 15-μm thick sections for immunohistochemical (IHC) staining. Sections were stained with: 1) anti-CD8 (rabbit IgG, 1:100; Neomarkers); 2) anti-CD45 antibody (rat IgG; 1:100; eBioscience); and 3) anti-mouse CD57 antibody (mouse IgM; 1:200; Neomarkers). A standard IHC staining procedure was used. Briefly, sections were deparaffinized, incubated for 10 minutes in 10 mM citrate buffer (pH 6.0) at 95°C for antigen retrieval. Endogenous peroxidase activity was quenched with 3% hydrogen peroxide. After quenching endogenous peroxidase activity and blocking nonspecific binding, slides were incubated with specific primary antibody overnight at

4°C followed by subsequent incubation with the appropriate biotinylated secondary antibody: goat anti–rabbit IgG (Vector); rabbit anti–mouse IgM and rabbit anti–rat IgG (Vector) at a 1:200 dilution for 30 minutes at RT. Immunoreactive antigens were detected using the Vectastain Elite ABC Immunoperoxidase Kit and DAB. All slides were counterstained with hematoxylin (Vector) and mounted with Permount (Fisher Scientific). The samples were imaged with optical microscopy at 400× magnification.

10.2.9. Flow Cytometry

Cells were recovered from PBL co-cultured samples after 6 days of culture. The cells were recovered from the CA scaffold samples through a scaffold degradation method whereby the CA scaffolds were incubated in 5 mL 30 mM sodium bicarbonate ($NaHCO_3$) and 5 mM HEPES solution at 37°C for 10 minutes, followed by the addition of 2 mL 10 mM EDTA and 20 mM HEPES solution, which was incubated at 37°C for an additional 5 minutes. The samples were then pipetted up and down with a 10-mL pipette several times to breakdown the CA scaffolds. After the scaffolds degraded into debris, the degradation solution of each scaffold sample was passed through a 70-μm cell strainer followed by a 40-μm cell strainer to separate the scaffold debris from the cells. After the cells were recovered, each sample was pelleted at 2250 rpm for 5 minutes, then washed once in washing buffer (5% FBS in D-PBS). The samples were blocked with staining buffer (10% human serum, 0.02% NaNO3, in D-PBS) for 15 minutes at room temperature and stained with antibodies for CD3 and CD56 (BD Biosciences) in staining buffer for 30 minutes in dark on ice. The samples were washed twice with washing buffer, and resuspended in 200 μL washing buffer. The samples were analyzed on a FACSCanto flow cytometer (BD Biosciences). The data were analyzed and plotted with the FlowJo software package (Tree Star Inc.).

10.2.10. Statistical Analysis

All the data were statistically analyzed to express the mean ± standard deviation (SD) of the mean.

10.3. Results and Discussion

10.3.1. CA Scaffolds for Supporting Prostate Tumor Growth

In vitro trials are widely used to elucidate the behavior of cancer cells, the mechanisms that control their behavior, and potential clinical treatments. Many of these trials are conducted with cells cultured on 2D surfaces (polystyrene tissue culture plates or wells), leading to discordant cell responses when applied to an *in vivo* system resulting from differences between 2D and 3D environments [11]. The use of 3D structures for *in vitro* trials allows for a more relevant model of the *in vivo* system and increases the chances of success in later, more costly stages of clinical trials. Biomaterial scaffolds (hydrogels or 3D porous scaffolds) are used to replicate the natural extracellular matrix in tissue engineering applications and have been demonstrated for tumor microenvironment applications [11, 95, 103, 104]. Here, CA scaffolds were evaluated as an *in vitro* culture model of PCa through cell proliferation and morphology assessment. The three human cell lines used are variants of the LNCaP line, with the C4-2 and C4-2B having increased metastatic potential and reduced androgen sensitivity, more closely resembling CRPC [191]. Human PCa cells were cultured in 2D culture wells (12-well plates), 3D Matrigel matrix, and 3D porous CA scaffold *in vitro* to examine the ability of CA scaffolds to support cell proliferation. Proliferation of the cells in each culture environment (2D, Matrigel, CA) was evaluated over 5, 10, and 15 days of *in vitro* culture using the alamarBlue assay (Figure 39). The 2D and Matrigel matrix samples had the greatest cell numbers in all cell lines, with both samples in each cell line having similar cell populations at 15 days. The CA scaffold samples demonstrated a lag in cell growth compared to other culture environments in all PCa cell lines as expected for 3D culture [103, 104, 192–194]. Studies have shown that the 3D microenvironment provided by porous scaffolds promotes greater malignancy of tumor cells than do Matrigel controls both *in vitro* and *in vivo* [101, 103, 104, 192–194]. This greater malignancy contributes to decreased proliferation, which more closely mimics the *in vivo* condition than the rapidly proliferating cells in standard 3D Matrigel culture [101, 103, 104, 192–194].

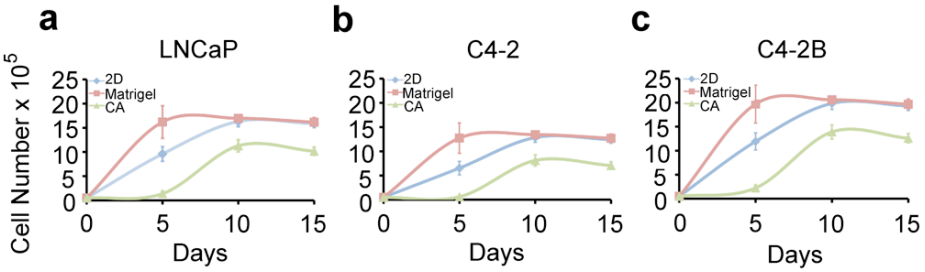

Figure 39. Proliferation PCa cells cultured on different substrates. The growth of (a) LNCaP, (b) C4-2, and (c) C4-2B human prostate cancer cells grown on 2D culture plates, Matrigel matrix, and CA scaffolds after 5, 10, and 15 days of culture was determined by the alamarBlue assay.

The PCa cell morphology in the three culture environments was observed with scanning electron microscopy (SEM). The SEM images (Figure 40) demonstrate the influence of culture environment on cell morphology. The 2D samples had flat layers of cells with little three-dimensional structure and did not form tumor spheroids. The Matrigel samples formed tumor spheroids within the gel matrix, while the cells on the plate surface (under the Matrigel matrix) had a linear and elongated morphology and formed dense, thick cell sheets in some regions. The CA scaffold samples demonstrated tumor spheroid formation within the scaffold pores. The cell morphology in these three culture environments indicates that the 3D environments promoted tumor spheroid formation, while the 2D surface did not. The ability of cells to form tumor spheroids in 3D culture environments provides a better replica of the *in vivo* tumor structure [11, 95, 103, 104]. This shows that the 3D environments should be better models for studying PBL interaction with tumor cells in vitro than 2D monolayer cultures.

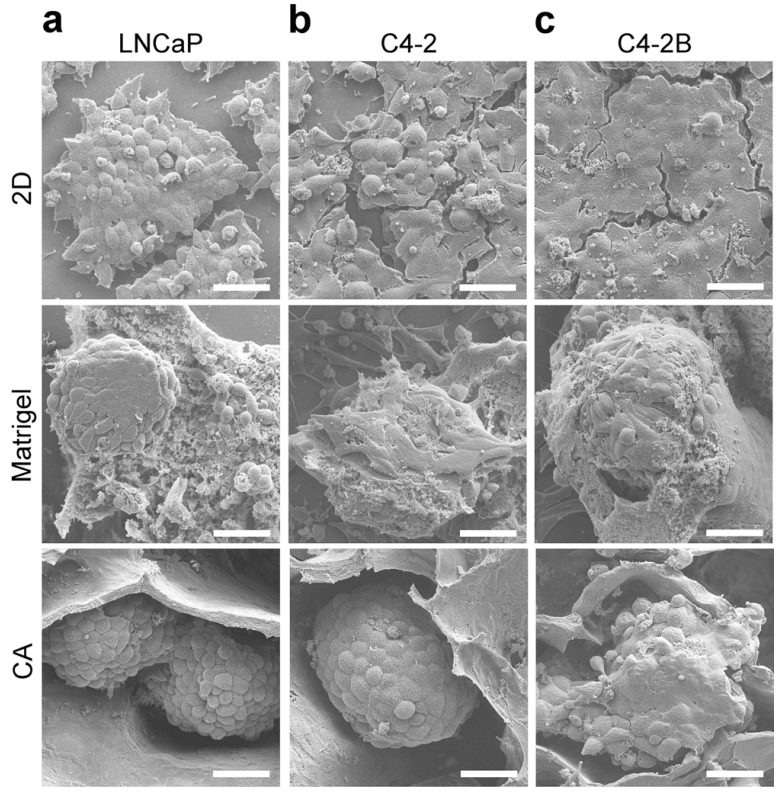

Figure 40. SEM images of PCa cells cultured on various substrates. (a) LNCaP, (b) C4-2, and (c) C4-2B human prostate cancer cells were grown on 2D culture plates, Matrigel matrix, and CA scaffolds for 15 days before analysis; scale bars are 40 μm.

10.3.2. Live Cell Tumor Monitoring

The CA scaffolds were further evaluated as an *in vitro* culture platform by demonstrating live-cell fluorescence imaging of cells cultured within the scaffolds. Mouse prostate tumor TRAMP-C2 (TC2) cells stably transfected with red fluorescent protein (TC2-RFP) were seeded in Matrigel matrix and CA scaffolds and were monitored with confocal microscopy at various times during culture (Figure 41). The Matrigel matrix and CA scaffold samples imaged one day after cell seeding (Figures 41a and 41b, respectively) showed a few cells within the matrices. CA scaffold samples at 14 days (Figure 41c) and 55 days (Figure 41d) after cell seeding showed the presence of large tumor spheroids within the CA scaffolds. The 55-day CA scaffold samples had several large tumor spheroids in the samples, which could be readily observed due to the stable RFP transfection. The Matrigel matrix became highly degraded after 7 days and could no longer

be imaged. This occurred in all Matrigel samples (n = 6), regardless of the ratio of Matrigel to cell solution (samples were cultured at 1:1 and 4:1 Matrigel:cell solution ratios). This matrix degradation is due to the high invasive nature of TC2 cells [95] and reveals the limitations of Matrigel for *in vitro* trials. Furthermore, Matrigel can commonly maintain *in vitro* culture for only 10 days [195]. The CA scaffolds supported cultures for longer periods (up to 55 days in this study), indicating they are more robust than Matrigel, allowing for prolonged analyses.

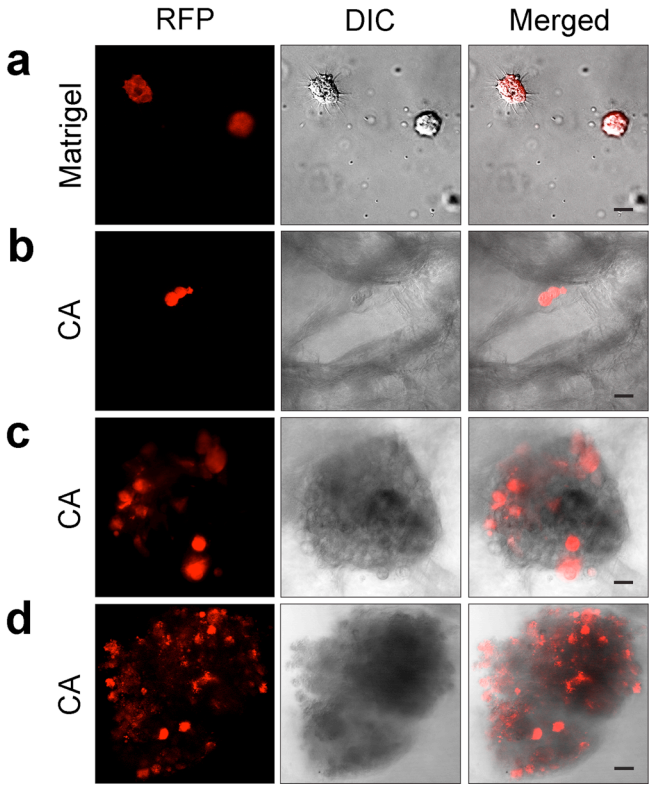

Figure 41. Live cell images of TC2-RFP cells grown on various substrates. Cells were grown for 1 day in (a) Matrigel matrix and (b) CA scaffolds. Cells were grown in CA scaffolds for (c) 14 days and (d) 55 days before imaging. Scale bars are 20 µm. Left: fluorescence; middle: differential interference contrast (DIC); right: overlay.

Figure 42 shows an expanded z-series confocal image illustrating an individual TC2-RFP tumor spheroid from cells cultured in CA scaffolds at day 55. The entire tumor spheroid was imaged with the z-stack at 5-µm intervals, which had a total height of 80 µm. The image labeled "Z-stack" is the projection of the individual RFP images comprising the entire z-series. The use of live-cell fluorescence imaging allows for real-time monitoring of the external surface of a

tumor spheroid and its interactions with the matrix and other cells. This could allow for real-time imaging of immune cell interaction and infiltration with tumor spheres within the 3D microenvironment with tracker dyes [196]. The ability to monitor specific cell–cell interactions can only be studied directly *in vitro*. The interplay between tumor cells and specific immune cells *in vivo* can be confounded by the presence of other stromal cells. Therefore, *in vitro* tests can be used to specifically dissect the interaction of immune cells with tumor cells and extrapolate tumor-specific elements that may inhibit immune-based therapies. CA scaffolds provide such an *in vitro* model, which is suitable for long-term trials and convenient for downstream analyses.

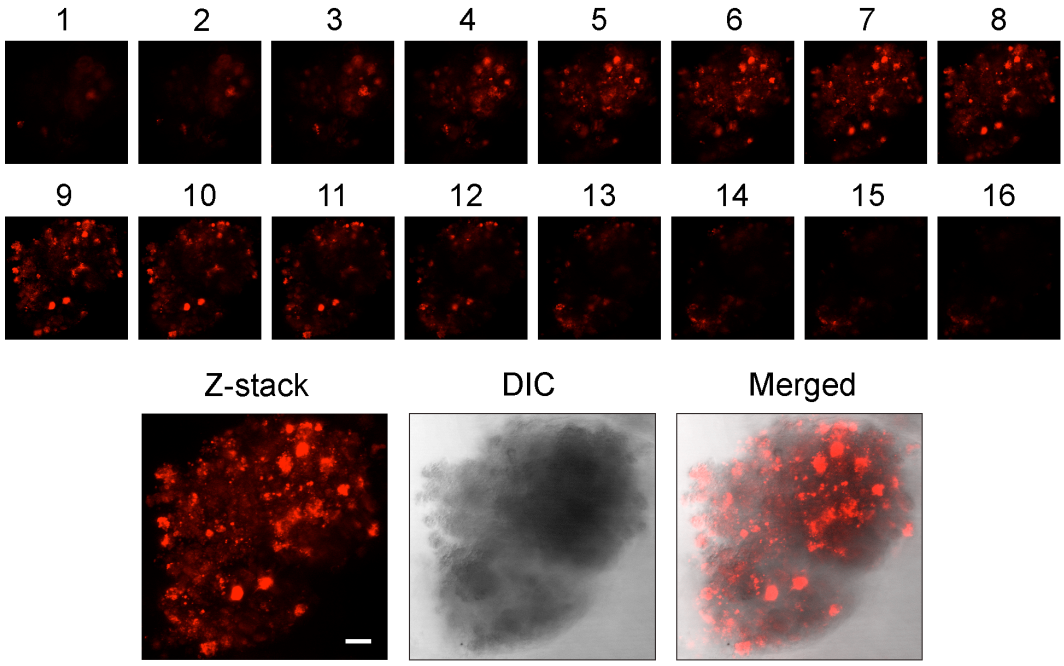

Figure 42. Z-series confocal imaging of a tumor sphere in CA scaffolds. Expanded live-cell confocal fluorescence z-stack images of 55-day *in vitro* culture CA scaffold samples, with each image of z-stack shown individually then combined in the z-stack projection. Total z-stack height is 80 µm with images at 5-µm increments. The DIC image is a representative image from the z-stack and the merged image is the combination of z-stack projection and DIC images. Scale bars are 20 µm.

10.3.3. Interaction of Human PBLs with In Vitro Tumors

10.3.3.1. SEM Imaging of PBLs Interacting with In Vitro Tumors

Human PCa cells (LNCaP, C4-2, and C4-2B) cultured in Matrigel matrix and CA scaffolds for 15 days to allow tumor spheroid formation were then co-cultured with human PBLs for 2 and 6 days to demonstrate the use of CA scaffolds for supporting interaction of primary lymphocytes with tumor cells *in vitro*. The cell–cell interactions were first analyzed with SEM imaging to determine the cell morphology. The SEM images indicated that PBLs could readily interact with *in vitro* tumors in both Matrigel and CA scaffold samples at the 2-day point (Figure 43). There is heterogeneity in the PBL population, so several different types of cells with different sizes were observed interacting with the tumors. In SEM images, these immune cells were distinguished from tumor cells by their morphology and size, and by comparing the SEM images of co-cultured samples (Figure 43) with the images of samples cultured with PCa cells only (Figure 40). The arrows in the high-magnification images indicate PBLs present on the surface of the PCa *in vitro* tumor spheroids. Physical interaction of PBLs with cancer cells in both the Matrigel matrix and CA scaffold samples was observed for all three cell lines. These images indicate that the *in vitro* culture of PCa cells in CA scaffolds is sufficient to allow immune cells to home to the tumor spheroids developed within the 3D structures. Both 3D structures supported interaction with immune cells; however, the CA scaffolds provided a more convenient model for SEM and IHC analyses (detailed in Section 10.3.3.2). Matrigel samples were challenging to analyze with SEM to determine cell morphology due to their fine 2-μm pore structure [11, 197], while the CA scaffolds provided an easily analyzed SEM sample in which the tumor spheroids could be imaged within the 100-μm pores.

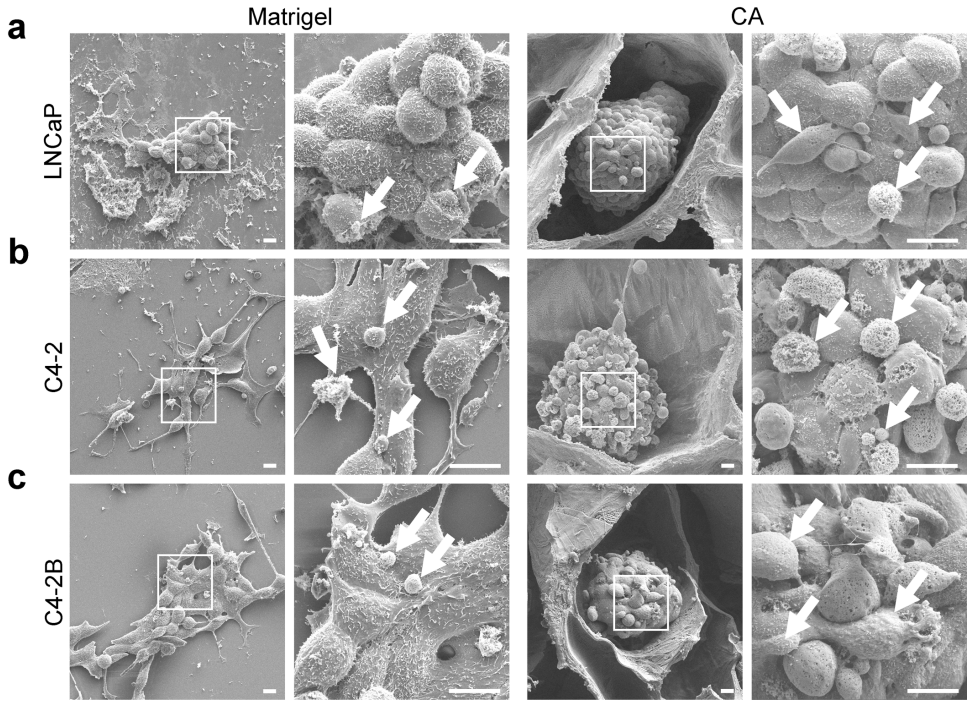

Figure 43. SEM images PCa cells grown on various substrates co-cultured with PBLs. (a) LNCaP, (b) C4-2, and (c) C4-2B human prostate cancer cells in Matrigel matrix and CA scaffolds were co-cultured with PBLs for 2 days. The boxes indicate the higher magnification region shown to the right and the arrows indicate PBLs. Scale bars are 10 μm.

10.3.3.2. Identification of PBLs Interacting with In Vitro Tumors

PBLs are comprised of T cells, B cells, and natural killer (NK) cells. T cells, the component of the adaptive immune system, are the major responders to vaccine-based therapies. NK cells are known to be the innate first defense against tumors. B cells are the component of the humoral immunity and also serve as antigen-presenting cells. To assess the specific types of PBLs that migrate and infiltrate to tumor spheroids and potentially interact with the human PCa in vitro tumors, we sectioned cultured scaffolds and analyzed them by IHC with antibodies to specific lymphocytes.

The localization of specific PBLs on the PCa-seeded scaffolds was first assessed through IHC analysis of CD45R staining. CD45R denotes B cells and activated T cells. CD45R+ cells were observed bound to the *in vitro* tumors in CA scaffolds at the 2-day point (Figure 44). Furthermore, the CD45R+ cells penetrated the tumor spheres after 6 days (Figure 44). The

number of CD45+ cells did not increase between 2 and 6 days, indicating these cells are likely B cells. T cells would start to become activated in the tumor microenvironment due to the presence of NK T cells, discussed below. This shows the ability of the *in vitro* tumors to promote the binding of PBLs.

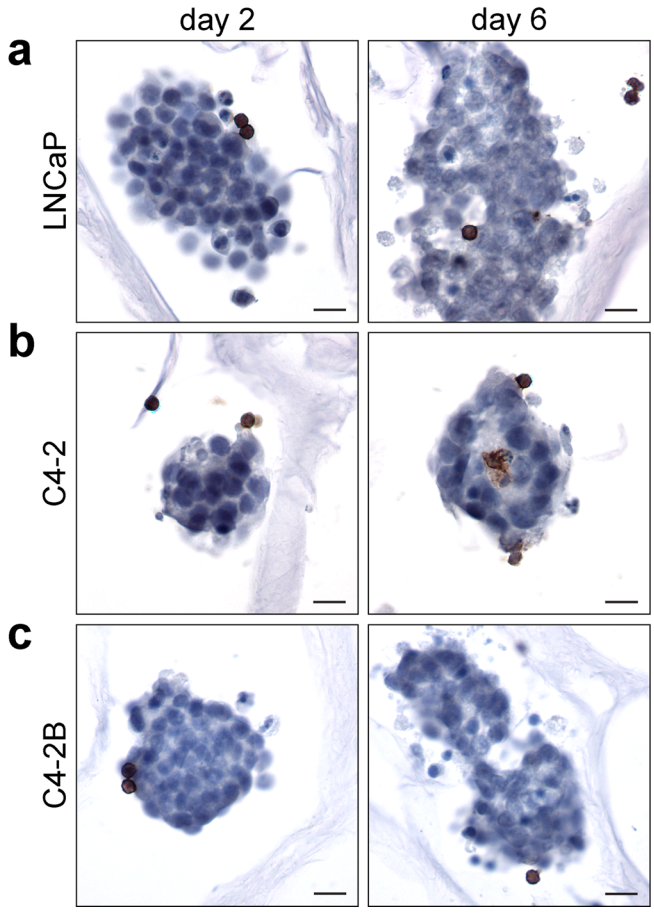

Figure 44. Immunohistochemical analysis of CD45R-expressing lymphocytes in CA scaffold co-cultured *in vitro* tumors. (a) LNCaP, (b) C4-2, and (c) C4-2B human prostate cancer cells in CA scaffolds were co-cultured with PBLs for 2 and 6 days; scale bars are 20 μm. The brown color denotes positive staining of B cells and the cell nuclei are counterstained blue.

Further characterization of PBLs on the PCa-seeded scaffolds was performed after 2-day co-culture through IHC staining of the CD8 and CD57 (Figure 45). Positive staining was observed for both CD8 and CD57, with significant CD57+ staining (Figure 45). In PBLs CD8 is present on T cells (30–40%), NK cells (30–40%), and more rarely (<5%) on monocytes and

neutrophils [198]. The observed interaction of CD8+ cells with the CA scaffold cultured *in vitro* tumors is intriguing and mimics the homing of CTLs observed in the *in vivo* setting [199]. CD57, or human natural killer-1 (HNK-1), is one of several markers used to denote NK cells with immunohistochemistry. NK cells are a type of lymphocyte that performs functions similar to both helper and cytotoxic T cells in that they both produce cytokines for immune activation and are directly involved in cell killing. Different from T cells, the recognition of tumor cells and activation of NK cells is through direct contact with tumor cells and does not require the participation of antigen-presenting cells. The CD57+ NK cells in the 2-day samples have penetrated the tumor spheres, indicating rapid migration into the *in vitro* tumors. This is especially apparent in the C4-2 and C4-2B *in vitro* tumors where the CD57+ cells can be observed in the light-colored areas of the tumor spheres, which likely corresponds to its necrotic center, a common phenomenon in tumor spheres and tumors *in vivo* [11]. High levels of NK cells were expected in the *in vitro* tumors since the cancer cells and PBLs are from different donors, and therefore have different major histocompatibility complex (MHC) class I markers.

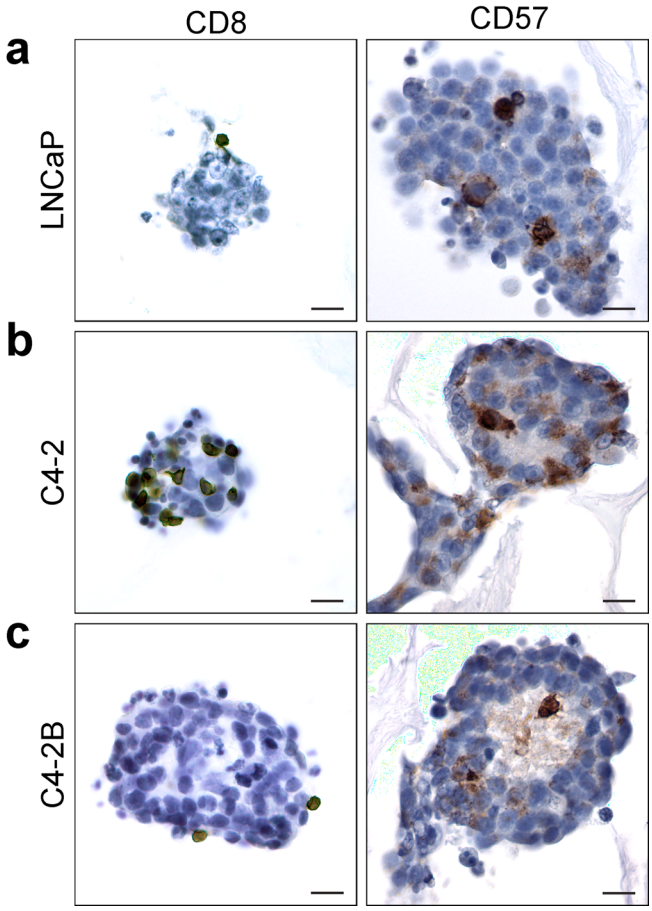

Figure 45. Immunohistochemical analysis of CD8 (T and NK cells), and CD57 (natural killer cells) in CA scaffold co-cultured *in vitro* tumors. (a) LNCaP, (b) C4-2, and (c) C4-2B human prostate cancer cells in CA scaffolds co-cultured with PBLs for 2 days; scale bars are 20 µm. The brown color denotes positive staining and the cell nuclei are counterstained blue.

10.3.3.3. Quantification of PBLs Interacting with In Vitro Tumors

The 6-day co-cultured CA scaffold human PCa samples were degraded, stained with CD3 (indicates T cells) and CD56, or neural cell adhesion molecule (NCAM, indicates NK cells), and analyzed with flow cytometry (Figure 46). The CA scaffold samples yielded a large number of tumor cells and PBLs; the gated regions denote the lymphocyte population, which was further analyzed for CD3 and CD56 positivity (Figure 46). Cell numbers required for accurate flow cytometry analysis could not be collected from Matrigel samples due to the difficulty in processing the gel matrix. CD3+CD56+ double-positive lymphocytes are defined as NK-T cells

(NKT), a subpopulation of T cells that have properties of NK cells [200, 201]. CD3-CD56- double-negative lymphocytes are likely B cells [202]. CD3-CD56+ lymphocytes are defined as NK cells and CD3+CD56- cells are T cells such as CTLs [203]. All CA scaffold samples had approximately 17% CD3-CD56+ NK cells (Figure 46), which confirms that NK cells were interacting with the tumor spheroids, as indicated in Figure 45 with CD57 IHC staining. Both CD56 and CD57 are NK cell-surface markers, with CD56 expressed in the majority of NK cells (> 95%), while CD57 is expressed in ~50 – 60% of NK cells [198]. Furthermore, CD3+CD56- T cells were observed at a similar level between the different tumor spheres, indicating similar tumor cell recognition regardless of malignancy. Interestingly, there was a positive correlation between the proportion of NKT cells incorporated with the tumor sphere and PCa cell malignancy. While the activity of NKT cells collected from PCa patients is compromised [200], NKT cells from healthy donors in this study showed highly effective recognition of malignant PCa. This suggests the NKT cell inactivation, which occurs in tumor evasion, is systemic rather than a result of the local tumor microenvironment, in agreement with previous studies [200, 204]; inactivation of NKT cells occurs in the blood rather than in the local tumor microenvironment. This highlights the utility of the CA scaffolds for studying tumor cell–lymphocyte interactions in PCa progression and therapy.

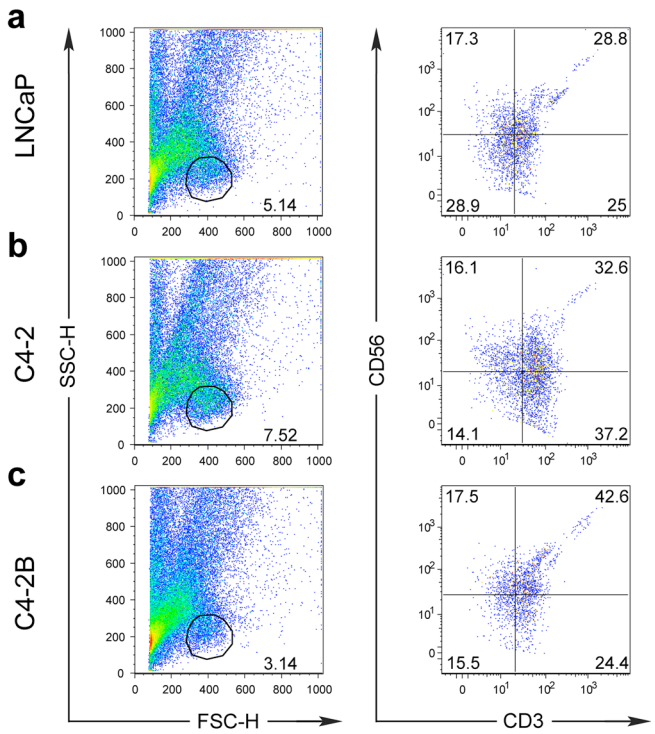

Figure 46. Flow cytometry analysis of CA scaffold co-cultured PCa cells and PBLs. (a) LNCaP, (b) C4-2, and (c) C4-2B human prostate cancer cells grown on CA scaffolds co-cultured with PBLs for 6 days were stained for CD3 and CD56. The left column shows the analyzed population and lymphocyte gates, while the right column shows the expression of CD3 and CD56 among lymphocytes. Population designations: CD3+CD56+, NKT cells; CD3-CD56-, B cells; CD3-CD56+, NK cells; CD3+CD56-, T cells.

These results indicate the ability to recover the co-cultured cells from CA scaffolds for analysis with flow cytometry. Flow cytometry is a valuable tool to investigate cell populations and could enable high-throughput screening and sorting of immunotherapies tested against cultures on the CA scaffolds. This flow cytometry analysis also demonstrates a use of the controlled degradation of the natural polymer CA scaffolds to allow for studying the functional interaction of co-cultured cells, as we have shown previously with embryonic stem cell cultures [134]. The use of an ionic scaffold degradation solution disrupts the polyelectrolyte complex formed between chitosan and alginate, leading to the separation of chitosan and alginate molecules and the degradation of the 3D porous CA scaffold and release of the cells. The EDTA in the scaffold degradation solution further helps break up the *in vitro* tumors into single cell suspensions.

The use of 3D biomaterial scaffolds for immunological or immunotherapy studies provide a more relevant model that should accelerate the successful translation of new immunotherapies into the clinic [179, 182, 183, 185, 196, 205, 206]. From current immunotherapy clinical trials it is clear that a better understanding of PBL interactions with PCa cells is required to develop more effective therapies [207]. These PCa tumors cultivated on CA scaffolds could be used as an *in vitro* platform for testing immunotherapies, potentially providing tumors that can be tested in a standard, high-throughput method, without relying on advanced CRPC patients.

10.4. Conclusions

We have demonstrated that CA scaffolds provide an *in vitro* culture environment for culture and study of PCa cells. Tumor spheroids formed in the CA scaffolds during 15 days of *in vitro* culture. Long-term culture (55 days) of PCa cells in CA scaffolds could be monitored *in situ* through fluorescence microscopy. Furthermore, the CA scaffolds supported the interaction of immune cells (including tumor-infiltrating B cells, T lymphocytes, and natural killer cells) with tumor cells and present a potential *in vitro* experimental model for screening immunotherapies to treat CRPC, and presumably other malignancies. The CA scaffolds also provided a more convenient platform than Matrigel or other hydrogels for subsequent analyses and supported prolonged culture. The enhanced *in vitro* tumor microenvironment model that the CA scaffold provides generates more clinically relevant responses as compared to 2D monolayer cultures due to the formation of tumor spheroids in the 3D cultures. The use of CA scaffolds as an *in vitro* tumor platform can be undoubtedly expanded to investigate the interaction between immune cells and other cancer cells, and will hopefully aid in the development of more effective therapies to treat various cancers.

11. Summary of Major Findings

This dissertation has demonstrated the use of 3D porous biomaterial scaffolds, primarily CA scaffolds, for bone tissue engineering and tumor microenvironment applications. These applications are relevant with the current progress in biomedical and cancer research. The use of alginate gel to enhance the cell seeding of porous ceramic scaffolds is the first use of a secondary phase polymer to enhance cell seeding of a ceramic scaffold. The alginate gel-seeded scaffolds had greater cell populations *in vitro* and greater osteogenesis *in vivo* compared to conventionally seeded scaffolds.

The work with the processing of CA scaffolds has demonstrated the ability to control the scaffold properties through control of the chitosan–alginate polyelectrolyte complex solution viscosity through pH, polymer concentration, and temperature. The CA scaffolds with the greatest polyelectrolyte complex formation had the highest mechanical properties and osteoblast population *in vitro*. The methods obtained from developing the processing control of the CA scaffolds were applied to produce CA scaffolds with different polymer concentrations from 2 to 10 wt% and pore sizes. The different pore size scaffolds were evaluated for mechanical properties and osteoblast culture, with the 4 wt% CA scaffold having a good balance of mechanical properties and pore size, leading to their use for the other applications. We then evaluated the CA scaffolds repair of rat calvarial defects, and found they enhanced defect closure and delivered other treatments to the defect site.

The 3D porous CA scaffolds were evaluated in tumor microenvironment applications where they were used for culture of glioblastoma and prostate cancer cells. The trials with glioblastoma cells demonstrated that the CA scaffolds enriched cancer stem cells in the seeded cell population during *in vitro* culture; their cancer stem cell properties were verified by functional studies of *in vivo* tumor formation. The prostate cancer trials demonstrated support of prostate cancer cell culture and success of co-culture with peripheral blood lymphocytes, indicating the possibility of using 3D porous CA scaffolds for an *in vitro* platform for screening immunotherapies. This was the first trial of a 3D porous scaffold for co-culture of immune cells

with cancer cells and demonstrates a platform with improved handling compared to 3D gels and greater biological properties than 2D tissue culture wells.

12. References

[1] Howden LM, Meyer JA. Age and Sex Composition: 2010. US Census Bureau 2011:1-16.
[2] Werner CA. The Older Population:2010. US Census Bureau 2011:1-19.
[3] Atala A. Engineering organs. Current Opinion in Biotechnology 2009;20(5):575-592.
[4] Badylak SF, Weiss DJ, Caplan A, Macchiarini P. Engineered whole organs and complex tissues. The Lancet 2012;379(9819):943-952.
[5] Orlando G, Wood KJ, Stratta RJ, Yoo JJ, Atala A, Soker S. Regenerative Medicine and Organ Transplantation: Past, Present, and Future. Transplantation 2011;91(12):1310-1317.
[6] Jemal A, Siegel R, Xu J, Ward E. Cancer statistics, 2010. CA: A Cancer Journal for Clinicians 2010;60(5):277-300.
[7] Ratner BD. A History of Biomaterials. In: Ratner BD, Hoffman AS, Schoen FJ, Lemons JE, editors. Biomaterials Science: An Introduction to Materials in Medicine. 2nd ed. Amsterdam: Elsevier, 2004. p. 10-19.
[8] Langer R, Tirrell DA. Designing materials for biology and medicine. Nature 2004;428(6982):487-492.
[9] Langer R, Vacanti JP. Tissue engineering. Science 1993;260(5110):920-926.
[10] Atala A. Regenerative medicine strategies. Journal of Pediatric Surgery 2012;47(1):17-28.
[11] Hutmacher DW, Loessner D, Rizzi S, Kaplan DL, Mooney DJ, Clements JA. Can tissue engineering concepts advance tumor biology research? Trends in Biotechnology 2010;28(3):125-133.
[12] Hutmacher DW, Schantz JT, Lam CXF, Tan KC, Lim TC. State of the art and future directions of scaffold-based bone engineering from a biomaterials perspective. Journal of Tissue Engineering and Regenerative Medicine 2007;1(4):245-260.
[13] Orkin SH, Morrison SJ. Stem-cell competition. Nature 2002;418(6893):25-27.
[14] Pittenger MF, Mackay AM, Beck SC, Jaiswal RK, Douglas R, Mosca JD, et al. Multilineage potential of adult human mesenchymal stem cells. Science 1999;284(5411):143-147.
[15] Reya T, Morrison SJ, Clarke MF, Weissman IL. Stem cells, cancer, and cancer stem cells. Nature 2001;414(6859):105-111.
[16] Zuk PA, Zhu M, Ashjian P, De Ugarte DA, Huang JI, Mizuno H, et al. Human adipose tissue is a source of multipotent stem cells. Molecular Biology of the Cell 2002;13(12):4279-4295.
[17] Hynes RO. The extracellular matrix: not just pretty fibrils. Science 2009;326(5957):1216-1219.
[18] Hynes RO, Naba A. Overview of the Matrisome--An Inventory of Extracellular Matrix Constituents and Functions. Cold Spring Harbor Perspectives in Biology 2012;4(1):a004903-a004903.
[19] Dado D, Levenberg S. Cell-scaffold mechanical interplay within engineered tissue. Seminars in Cell & Developmental Biology 2009;20(6):656-664.
[20] Meijer GJ, de Bruijn JD, Koole R, van Blitterswijk CA. Cell-based bone tissue engineering. PLoS Medicine 2007;4(2):e9.

[21] Hutmacher DW. Scaffolds in tissue engineering bone and cartilage. Biomaterials 2000;21(24):2529-2543.
[22] Fröhlich M, Grayson WL, Wan LQ, Marolt D, Drobnic M, Vunjak-Novakovic G. Tissue engineered bone grafts: biological requirements, tissue culture and clinical relevance. Current Stem Cell Research & Therapy 2008;3(4):254-264.
[23] Mano JF, Silva GA, Azevedo HS, Malafaya PB, Sousa RA, Silva SS, et al. Natural origin biodegradable systems in tissue engineering and regenerative medicine: present status and some moving trends. Journal of the Royal Society Interface 2007;4(17):999-1030.
[24] Seunarine K, Gadegaard N, Tormen M, Meredith DO, Riehle MO, Wilkinson CDW. 3D polymer scaffolds for tissue engineering. Nanomedicine 2006;1(3):281-296.
[25] Butscher A, Bohner M, Hofmann S, Gauckler L, Müller R. Structural and material approaches to bone tissue engineering in powder-based three-dimensional printing. Acta Biomaterialia 2011;7(3):907-920.
[26] Hollister SJ. Porous scaffold design for tissue engineering. Nature Materials 2005;4(7):518-524.
[27] Yeong W-Y, Chua C-K, Leong K-F, Chandrasekaran M. Rapid prototyping in tissue engineering: challenges and potential. Trends In Biotechnology 2004;22(12):643-652.
[28] Porter J, Ruckh T, Popat K. Bone tissue engineering: a review in bone biomimetics and drug delivery strategies. Biotechnology Progress 2009;25(6):1539-1560.
[29] LeGeros RZ. Calcium Phosphate-Based Osteoinductive Materials. Chemical Reviews 2008;108(11):4742-4753.
[30] Gorski JP. Is all bone the same? Distinctive distributions and properties of non-collagenous matrix proteins in lamellar vs. woven bone imply the existence of different underlying osteogenic mechanisms. Critical Reviews in Oral Biology & Medicine 1998;9(2):201-223.
[31] Gorski JP. Biomineralization of bone: a fresh view of the roles of non-collagenous proteins. Frontiers in Bioscience 2011;16:2598-2621.
[32] Mackie EJ. Osteoblasts: novel roles in orchestration of skeletal architecture. International Jouranl of Biochemistry & Cell Biology 2003;35(9):1301-1305.
[33] Matsuo K, Irie N. Osteoclast-osteoblast communication. Archives of Biochemistry and Biophysics 2008;473(2):201-209.
[34] Wei J, Ducy P. Co-dependence of bone and energy metabolisms. Archives of Biochemistry and Biophysics 2010;503(1):35-40.
[35] Datta HK, Ng WF, Walker JA, Tuck SP, Varanasi SS. The cell biology of bone metabolism. Journal of Clinical Pathology 2008;61(5):577-587.
[36] Pogoda P, Priemel M, Rueger JM, Amling M. Bone remodeling: new aspects of a key process that controls skeletal maintenance and repair. Osteoporosis International 2005;16:S18-24.
[37] Schindeler A, McDonald MM, Bokko P, Little DG. Bone remodeling during fracture repair: The cellular picture. Seminars in Cell & Developmental Biology 2008;19(5):459-466.
[38] Sims NA, Gooi JH. Bone remodeling: Multiple cellular interactions required for coupling of bone formation and resorption. Seminars in Cell & Developmental Biology 2008;19(5):444-451.

[39] Cooper GM, Mooney MP, Gosain AK, Campbell PG, Losee JE, Huard J. Testing the critical size in calvarial bone defects: revisiting the concept of a critical-size defect. Plastic and Reconstructive Surgery 2010;125(6):1685-1692.
[40] Schmitz JP, Hollinger JO. The critical size defect as an experimental model for craniomandibulofacial nonunions. Clinical Orthopaedics and Related Research 1986;(205):299-308.
[41] Cho YR, Gosain AK. Biomaterials in craniofacial reconstruction. Clinics in Plastic Surgery 2004;31(3):377-385.
[42] Kretlow JD, Young S, Klouda L, Wong M, Mikos AG. Injectable Biomaterials for Regenerating Complex Craniofacial Tissues. Advanced Materials 2009;21(32-33):3368-3393.
[43] Gross RH. The use of bone grafts and bone graft substitutes in pediatric orthopaedics: an overview. Journal of Pediatric Orthopedics 2012;32(1):100-105.
[44] Neovius E, Engstrand T. Craniofacial reconstruction with bone and biomaterials: Review over the last 11 years. Journal of Plastic, Reconstructive & Aesthetic Surgery 2010;63(10):1615-1623.
[45] Afifi AM, Gordon CR, Pryor LS, Sweeney W, Papay FA, Zins JE. Calcium Phosphate Cements in Skull Reconstruction: A Meta-Analysis. Plastic and Reconstructive Surgery 2010;126(4):1300-1309.
[46] Kretlow J, Young S, Klouda L, Wong M, Mikos A. Injectable Biomaterials for Regenerating Complex Craniofacial Tissues. Advanced Materials 2009;21(32-33):3368-3393.
[47] Lutolf MP, Weber F, Schmoekel HG, Schense JC, Kohler T, Müller R, et al. Repair of bone defects using synthetic mimetics of collagenous extracellular matrices. Nature Biotechnology 2003;21(5):513-518.
[48] Karageorgiou V, Kaplan D. Porosity of 3D biomaterial scaffolds and osteogenesis. Biomaterials 2005;26(27):5474-5491.
[49] Yuan H, Fernandes H, Habibovic P, de Boer J, Barradas AMC, de Ruiter A, et al. Osteoinductive ceramics as a synthetic alternative to autologous bone grafting. Proceedings of the National Academy of Sciences of the United States of America 2010;107(31):13614-13619.
[50] Seebach C, Schultheiss J, Wilhelm K, Frank J, Henrich D. Comparison of six bone-graft substitutes regarding to cell seeding efficiency, metabolism and growth behaviour of human mesenchymal stem cells (MSC) in vitro. Injury 2010;41(7):914-921.
[51] Ramay HR, Zhang M. Preparation of porous hydroxyapatite scaffolds by combination of the gel-casting and polymer sponge methods. Biomaterials 2003;24(19):3293-3302.
[52] Ramay HRR, Zhang M. Biphasic calcium phosphate nanocomposite porous scaffolds for load-bearing bone tissue engineering. Biomaterials 2004;25(21):5171-5180.
[53] Quarto R, Mastrogiacomo M, Cancedda R, Kutepov SM, Mukhachev V, Lavroukov A, et al. Repair of large bone defects with the use of autologous bone marrow stromal cells. The New England Journal of Medicine 2001;344(5):385-386.
[54] Marcacci M, Kon E, Moukhachev V, Lavroukov A, Kutepov S, Quarto R, et al. Stem cells associated with macroporous bioceramics for long bone repair: 6- to 7-year outcome of a pilot clinical study. Tissue Engineering 2007;13(5):947-955.

[55] Burdick JA, Frankel D, Dernell WS, Anseth KS. An initial investigation of photocurable three-dimensional lactic acid based scaffolds in a critical-sized cranial defect. Biomaterials 2003;24(9):1613-1620.
[56] Cowan CM, Shi Y-Y, Aalami OO, Chou Y-F, Mari C, Thomas R, et al. Adipose-derived adult stromal cells heal critical-size mouse calvarial defects. Nature Biotechnology 2004;22(5):560-567.
[57] Kasper FK, Young S, Tanahashi K, Barry MA, Tabata Y, Jansen J, et al. Evaluation of bone regeneration by DNA release from composites of oligo(poly(ethylene glycol) fumarate) and cationized gelatin microspheres in a critical-sized calvarial defect. Journal of Biomedical Materials Research Part A 2006;78(2):335-342.
[58] O'Brien FJ. Biomaterials & scaffolds for tissue engineering. Materials Today 2011;14(3):88-95.
[59] Rinaudo M. Main properties and current applications of some polysaccharides as biomaterials. Polymer International 2008;57:397-430.
[60] Kretlow JD, Mikos AG. From material to tissue: Biomaterial development, scaffold fabrication, and tissue engineering. AIChE Journal 2008;54(12):3048-3067.
[61] Ward B, Brown S, Krebsbach P. Bioengineering strategies for regeneration of craniofacial bone: a review of emerging technologies. Oral Diseases 2010;16(8):709-716.
[62] Rinaudo M. Properties and degradation of selected polysaccharides: hyaluronan and chitosan. Corrosion Engineering, Science and Technology 2007;42(4):324-334.
[63] MacIntosh AC, Kearns VR, Crawford A, Hatton PV. Skeletal tissue engineering using silk biomaterials. Journal of Tissue Engineering and Regenerative Medicine 2008;2(2-3):71-80.
[64] Muzzarelli RAA. Chitosan composites with inorganics, morphogenetic proteins and stem cells, for bone regeneration. Carbohydrate Polymers 2011;83(4):1433-1445.
[65] Donzelli E, Salvadè A, Mimo P, Viganò M, Morrone M, Papagna R, et al. Mesenchymal stem cells cultured on a collagen scaffold: In vitro osteogenic differentiation. Archives of Oral Biology 2007;52(1):64-73.
[66] Lode A, Bernhardt A, Gelinsky M. Cultivation of human bone marrow stromal cells on three-dimensional scaffolds of mineralized collagen: influence of seeding density on colonization, proliferation and osteogenic differentiation. Journal of Tissue Engineering and Regenerative Medicine 2008;2(7):400-407.
[67] Di Martino A, Sittinger M, Risbud MV. Chitosan: a versatile biopolymer for orthopaedic tissue-engineering. Biomaterials 2005;26(30):5983-5990.
[68] Muzzarelli RAA. Chitins and chitosans for the repair of wounded skin, nerve, cartilage and bone. Carbohydrate Polymers 2009;76(2):167-182.
[69] Martins AM, Alves CM, Kasper FK, Mikos AG, Reis RL. Responsive and in situ-forming chitosan scaffolds for bone tissue engineering applications: an overview of the last decade. Journal of Materials Chemistry 2010;20(9):1638.
[70] Oest ME, Dupont KM, Kong H-J, Mooney DJ, Guldberg RE. Quantitative assessment of scaffold and growth factor-mediated repair of critically sized bone defects. Journal of Orthopaedic Research 2007;25(7):941-950.
[71] Huang Z, Ren P-G, Ma T, Smith RL, Goodman SB. Modulating osteogenesis of mesenchymal stem cells by modifying growth factor availability. Cytokine 2010;51(3):305-310.

[72] Carofino BC, Lieberman JR. Gene therapy applications for fracture-healing. Journal of Bone & Joint Surgery Am 2008;90 Suppl 1:99-110.
[73] Bessa PC, Casal M, Reis RL. Bone morphogenetic proteins in tissue engineering: the road from the laboratory to the clinic, part I (basic concepts). Journal of Tissue Engineering and Regenerative Medicine 2008;2(1):1-13.
[74] Bessa PC, Casal M, Reis RL. Bone morphogenetic proteins in tissue engineering: the road from laboratory to clinic, part II (BMP delivery). Journal of Tissue Engineering and Regenerative Medicine 2008;2(2-3):81-96.
[75] Haidar ZS, Hamdy RC, Tabrizian M. Delivery of recombinant bone morphogenetic proteins for bone regeneration and repair. Part A: Current challenges in BMP delivery. Biotechnology Letters 2009;31(12):1817-1824.
[76] Peng H, Usas A, Olshanski A, Ho AM, Gearhart B, Cooper GM, et al. VEGF improves, whereas sFlt1 inhibits, BMP2-induced bone formation and bone healing through modulation of angiogenesis. Journal of Bone Mineral Research 2005;20(11):2017-2027.
[77] Miyazaki M, Sugiyama O, Tow B, Zou J, Morishita Y, Wei F, et al. The effects of lentiviral gene therapy with bone morphogenetic protein-2-producing bone marrow cells on spinal fusion in rats. Journal of Spinal Disorder Tech 2008;21(5):372-379.
[78] Miyazaki M, Sugiyama O, Zou J, Yoon SH, Wei F, Morishita Y, et al. Comparison of lentiviral and adenoviral gene therapy for spinal fusion in rats. Spine 2008;33(13):1410-1417.
[79] Lieberman JR, Daluiski A, Stevenson S, Wu L, McAllister P, Lee YP, et al. The effect of regional gene therapy with bone morphogenetic protein-2-producing bone-marrow cells on the repair of segmental femoral defects in rats. Journal of Bone & Joint Surgery Am 1999;81(7):905-917.
[80] Lieberman JR, Ghivizzani SC, Evans CH. Gene transfer approaches to the healing of bone and cartilage. Molecular Therapy 2002;6(2):141-147.
[81] Lieberman JR, Le LQ, Wu L, Finerman GA, Berk A, Witte ON, et al. Regional gene therapy with a BMP-2-producing murine stromal cell line induces heterotopic and orthotopic bone formation in rodents. Journal of Orthopaedic Research 1998;16(3):330-339.
[82] Hanahan D, Weinberg RA. The hallmarks of cancer. Cell 2000;100(1):57-70.
[83] Hanahan D, Weinberg RA. Hallmarks of cancer: the next generation. Cell 2011;144(5):646-674.
[84] Talmadge JE, Fidler IJ. AACR Centennial Series: The Biology of Cancer Metastasis: Historical Perspective. Cancer Research 2010;70(14):5649-5669.
[85] Langley RR, Fidler IJ. Tumor Cell-Organ Microenvironment Interactions in the Pathogenesis of Cancer Metastasis. Endocrine Reviews 2007;28(3):297-321.
[86] Fidler IJ. The pathogenesis of cancer metastasis: the 'seed and soil' hypothesis revisited. Nature Reviews Cancer 2003;3(6):453-458.
[87] Bissell M, Hines WC. Why don't we get more cancer? A proposed role of the microenvironment in restraining cancer progression. Nature Medicine 2011;17(3):320-329.
[88] Kimlin LC, Casagrande G, Virador VM. In vitro three-dimensional (3D) models in cancer research: An update. Molecular Carcinogenesis 2011:1-16.
[89] Schreiber RD, Old LJ, Smyth MJ. Cancer immunoediting: integrating immunity's roles in cancer suppression and promotion. Science 2011;331(6024):1565-1570.

[90] Hutmacher DW. Biomaterials offer cancer research the third dimension. Nature Materials 2010;9(2):90-93.
[91] Gottfried E, Kunz-Schughart LA, Andreesen R, Kreutz M. Brave little world: spheroids as an in vitro model to study tumor-immune-cell interactions. Cell Cycle 2006;5(7):691-695.
[92] Hirschhaeuser F, Menne H, Dittfeld C, West J, Mueller-Klieser W, Kunz-Schughart LA. Multicellular tumor spheroids: an underestimated tool is catching up again. Journal of Biotechnology 2010;148(1):3-15.
[93] Ong S-M, Zhao Z, Arooz T, Zhao D, Zhang S, Du T, et al. Engineering a scaffold-free 3D tumor model for in vitro drug penetration studies. Biomaterials 2010;31(6):1180-1190.
[94] Justice BA, Badr NA, Felder RA. 3D cell culture opens new dimensions in cell-based assays. Drug Discovery Today 2009;14(1-2):102-107.
[95] Benton G, Kleinman H, George J, Arnaoutova I. Multiple uses of basement membrane-like matrix (BME/Matrigel) in vitro and in vivo with cancer cells. International Journal of Cancer 2011;128(8):1751-1757.
[96] Kleinman HK, Martin GR. Matrigel: basement membrane matrix with biological activity. Seminars in Cancer Biology 2005;15(5):378-386.
[97] Dolznig H, Rupp C, Puri C, Haslinger C, Schweifer N, Wieser E, et al. Modeling Colon Adenocarcinomas in Vitro. The American Journal of Pathology 2011;179(1):487-501.
[98] Krause S, Maffini MV, Soto AM, Sonnenschein C. The microenvironment determines the breast cancer cells' phenotype: organization of MCF7 cells in 3D cultures. BMC Cancer 2010;10(1):263.
[99] Loessner D, Stok KS, Lutolf MP, Hutmacher DW, Clements JA, Rizzi SC. Bioengineered 3D platform to explore cell-ECM interactions and drug resistance of epithelial ovarian cancer cells. Biomaterials 2010;31(32):8494-8506.
[100] Fischbach C, Kong HJ, Hsiong SX, Evangelista MB, Yuen W, Mooney DJ. Cancer cell angiogenic capability is regulated by 3D culture and integrin engagement. Proceedings of the National Academy of Sciences of the United States of America 2009;106(2):399-404.
[101] Fischbach C, Chen R, Matsumoto T, Schmelzle T, Brugge JS, Polverini PJ, et al. Engineering tumors with 3D scaffolds. Nature Methods 2007;4(10):855-860.
[102] Sieh S, Lubik AA, Clements JA, Nelson CC, Hutmacher DW. Interactions between human osteoblasts and prostate cancer cells in a novel 3D in vitro model. Organogenesis 2010;6(3):181-188.
[103] Kievit F, Florczyk S, Leung MC, Veiseh O, Park JO, Disis M, et al. Chitosan-alginate 3D scaffolds as a mimic of the glioma tumor microenvironment. Biomaterials 2010;31(22):5903-5910.
[104] Leung M, Kievit F, Florczyk SJ, Veiseh O, Wu J, Park JO, et al. Chitosan-alginate scaffold culture system for hepatocellular carcinoma increases malignancy and drug resistance. Pharmaceutical Research 2010;27(9):1939-1948.
[105] Ho WJ, Pham EA, Kim JW, Ng CW, Kim JH, Kamei DT, et al. Incorporation of multicellular spheroids into 3-D polymeric scaffolds provides an improved tumor model for screening anticancer drugs. Cancer Science 2010;101(12):2637-2643.
[106] Huh D, Hamilton GA, Ingber DE. From 3D cell culture to organs-on-chips. Trends in Cell Biology 2011;21(12):745-754.

[107] Ellis LM, Fidler IJ. Finding the tumor copycat: Therapy fails, patients don't. Nature Medicine 2010;16(9):974-975.
[108] Willie BM, Petersen A, Schmidt-Bleek K, Cipitria A, Mehta M, Strube P, et al. Designing biomimetic scaffolds for bone regeneration: why aim for a copy of mature tissue properties if nature uses a different approach? Soft Matter 2010:1-12.
[109] Dorozhkin SV. Bioceramics of calcium orthophosphates. Biomaterials 2010;31(7):1465-1485.
[110] Hasegawa T, Miwa M, Sakai Y, Niikura T, Lee SY, Oe K, et al. Efficient cell-seeding into scaffolds improves bone formation. Journal of Dental Research 2010;89(8):854-859.
[111] Melchels FPW, Barradas AMC, Van Blitterswijk CA, de Boer J, Feijen J, Grijpma DW. Effects of the architecture of tissue engineering scaffolds on cell seeding and culturing. Acta Biomaterialia 2010;6(11):4208-4217.
[112] Godbey WT, Hindy SBS, Sherman ME, Atala A. A novel use of centrifugal force for cell seeding into porous scaffolds. Biomaterials 2004;25(14):2799-2805.
[113] Shahin K, Doran PM. Improved seeding of chondrocytes into polyglycolic acid scaffolds using semi-static and alginate loading methods. Biotechnology Progress 2011;27(1):191-200.
[114] Shimizu K, Ito A, Honda H. Mag-seeding of rat bone marrow stromal cells into porous hydroxyapatite scaffolds for bone tissue engineering. Journal of Bioscience and Bioengineering 2007;104(3):171-177.
[115] Eslaminejad MB, Mirzadeh H, Nickmahzar A, Mohamadi Y, Mivehchi H. Type I collagen gel in seeding medium improves murine mesencymal stem cell loading onto the scaffold, increases their subsequent proliferation, and enhances culture mineralization. Journal of Biomedical Materials Research Part B Applied Biomaterials 2009;90(2):659-667.
[116] Li Z, Gunn J, Chen M-H, Cooper A, Zhang M. On-site alginate gelation for enhanced cell proliferation and uniform distribution in porous scaffolds. Journal of Biomedical Materials Research Part A 2008;86(2):552-559.
[117] Lee S-H, Shin H. Matrices and scaffolds for delivery of bioactive molecules in bone and cartilage tissue engineering. Advanced Drug Delivery Reviews 2007;59(4-5):339-359.
[118] Tessmar JK, Gopferich AM. Matrices and scaffolds for protein delivery in tissue engineering. Advanced Drug Delivery Reviews 2007;59:274-291.
[119] Ziegler J, Anger D, Krummenauer F, Breitig D, Fickert S, Guenther K-P. Biological activity of recombinant human growth factors released from biocompatible bone implants. Journal of Biomedical Materials Research, Part A 2007;86A:89-97.
[120] Long S, Truong L, Bennett K, Phillips A, Wong-Staal F, Ma H. Expression, purification, and renaturation of bone morphogenetic protein-2 from Escherichia coli. Protein Expression and Purification 2006;46(2):374-378.
[121] Mauney JR, Nguyen T, Gillen K, Kirker-Head C, Gimble JM, Kaplan DL. Engineering adipose-like tissue in vitro and in vivo utilizing human bone marrow and adipose-derived mesenchymal stem cells with silk fibroin 3D scaffolds. Biomaterials 2007;28(35):5280-5290.
[122] Kim K, Dean D, Mikos AG, Fisher JP. Effect of initial cell seeding density on early osteogenic signal expression of rat bone marrow stromal cells cultured on cross-linked poly(propylene fumarate) disks. Biomacromolecules 2009;10(7):1810-1817.

[123] Laub M, Seul T, Schmachtenberg E, Jennissen H. Molecular Modelling of Bone Morphogeninc Protein-2 (BMP-2) by 3D-Rapid Prototyping. Mat-wiss u Werkstofftech 2001;32:926-930.
[124] Haidar ZS, Hamdy RC, Tabrizian M. Delivery of recombinant bone morphogenetic proteins for bone regeneration and repair. Part B: Delivery systems for BMPs in orthopaedic and craniofacial tissue engineering. Biotechnology Letters 2009;31(12):1825-1835.
[125] Cartmell S. Controlled release scaffolds for bone tissue engineering. Journal of Pharmaceutical Sciences 2009;98(2):430-441.
[126] Lutolf MP, Hubbell JA. Synthetic biomaterials as instructive extracellular microenvironments for morphogenesis in tissue engineering. Nature Biotechnology 2005;23(1):47-55.
[127] Santos MI, Reis RL. Vascularization in bone tissue engineering: physiology, current strategies, major hurdles and future challenges. Macromolecular Bioscience 2010;10(1):12-27.
[128] Geuze RE, Everts PA, Kruyt MC, Verbout AJ, Alblas J, Dhert WJA. Orthotopic location has limited benefit from allogeneic or autologous multipotent stromal cells seeded on ceramic scaffolds. Tissue Engineering Part A 2009;15(11):3231-3239.
[129] Han J, Zhou Z, Yin R, Yang D, Nie J. Alginate-chitosan/hydroxyapatite polyelectrolyte complex porous scaffolds: preparation and characterization. International Journal of Biological Macromolecules 2010;46(2):199-205.
[130] Lankalapalli S, Kolapalli VRM. Polyelectrolyte Complexes: A Review of their Applicability in Drug Delivery Technology. Indian Journal of Pharmaceutical Sciences 2009;71(5):481-487.
[131] Vauthier C, Bouchemal K. Methods for the preparation and manufacture of polymeric nanoparticles. Pharmaceutical Research 2009;26(5):1025-1058.
[132] Li Z, Zhang M. Chitosan-alginate as scaffolding material for cartilage tissue engineering. Journal of Biomedical Materials Research Part A 2005;75(2):485-493.
[133] Li Z, Ramay HR, Hauch KD, Xiao D, Zhang M. Chitosan-alginate hybrid scaffolds for bone tissue engineering. Biomaterials 2005;26(18):3919-3928.
[134] Li Z, Leung M, Hopper R, Ellenbogen R, Zhang M. Feeder-free self-renewal of human embryonic stem cells in 3D porous natural polymer scaffolds. Biomaterials 2010;31(3):404-412.
[135] Shapiro L, Cohen S. Novel alginate sponges for cell culture and transplantation. Biomaterials 1997;18(8):583-590.
[136] Chung TW, Yang J, Akaike T, Cho KY, Nah JW, Kim SI, et al. Preparation of alginate/galactosylated chitosan scaffold for hepatocyte attachment. Biomaterials 2002;23(14):2827-2834.
[137] Yin Y, Ye F, Cui J, Zhang F, Li X, Yao K. Preparation and characterization of macroporous chitosan-gelatin/beta-tricalcium phosphate composite scaffolds for bone tissue engineering. Journal of Biomedical Materials Research Part A 2003;67(3):844-855.
[138] Berger J, Reist M, Mayer JM, Felt O, Gurny R. Structure and interactions in chitosan hydrogels formed by complexation or aggregation for biomedical applications. European Journal of Pharmaceutics and Biopharmaceutics 2004;57(1):35-52.

[139] Drosse I, Volkmer E, Capanna R, De Biase P, Mutschler W, Schieker M. Tissue engineering for bone defect healing: an update on a multi-component approach. Injury 2008;39 Suppl 2:S9-20.
[140] Liu C, Xia Z, Czernuszka JT. Design and Development of Three-Dimensional Scaffolds for Tissue Engineering. Chemical Engineering Research and Design 2007;85(7):1051-1064.
[141] Neuendorf RE, Saiz E, Tomsia AP, Ritchie RO. Adhesion between biodegradable polymers and hydroxyapatite: Relevance to synthetic bone-like materials and tissue engineering scaffolds. Acta Biomaterialia 2008;4(5):1288-1296.
[142] Kim B-S, Park I-K, Hoshiba T, Jiang H-L, Choi Y-J, Akaike T, et al. Design of artificial extracellular matrices for tissue engineering. Progress in Polymer Science 2011;36(2):238-268.
[143] Puppi D, Chiellini F, Piras AM, Chiellini E. Polymeric materials for bone and cartilage repair. Progress in Polymer Science 2010;35(4):403-440.
[144] Sokolsky-Papkov M, Agashi K, Olaye A, Shakesheff K, Domb AJ. Polymer carriers for drug delivery in tissue engineering. Advanced Drug Delivery Reviews 2007;59(4-5):187-206.
[145] Smith LA, Liu X, Ma PX. Tissue Engineering with Nano-Fibrous Scaffolds. Soft Matter 2008;4(11):2144-2149.
[146] Florczyk SJ, Kim D-J, Wood DL, Zhang M. Influence of processing parameters on pore structure of 3D porous chitosan-alginate polyelectrolyte complex scaffolds. Journal of Biomedical Materials Research 2011;98A(4):614-620.
[147] Alman BA, Kelley SP, Nam D. Heal Thyself: Using Endogenous Regeneration to Repair Bone. Tissue Engineering Part B: Reviews 2011;17(6):431-436.
[148] Huang G-S, Dai L-G, Yen BL, Hsu S-H. Spheroid formation of mesenchymal stem cells on chitosan and chitosan-hyaluronan membranes. Biomaterials 2011;32(29):6929-6945.
[149] Wang W, Itaka K, Ohba S, Nishiyama N, Chung U-I, Yamasaki Y, et al. 3D spheroid culture system on micropatterned substrates for improved differentiation efficiency of multipotent mesenchymal stem cells. Biomaterials 2009;30(14):2705-2715.
[150] Cowan C, Aghaloo T, Chou Y, Walder B, Zhang X, Soo C, et al. MicroCT evaluation of three-dimensional mineralization in response to BMP-2 doses in vitro and in critical sized rat calvarial defects. Tissue Engineering 2007;13(3):501-512.
[151] Patel ZS, Young S, Tabata Y, Jansen J, Wong ME, Mikos A. Dual delivery of an angiogenic and an osteogenic growth factor for bone regeneration in a critical size defect model. Bone 2008;43(5):931-940.
[152] O'Brien CA, Kreso A, Jamieson CH. Cancer stem cells and self-renewal. Clinical Cancer Research 2010;16(12):3113-3120.
[153] Rosen JM, Jordan CT. The increasing complexity of the cancer stem cell paradigm. Science 2009;324(5935):1670-1673.
[154] Visvader JE, Lindeman GJ. Cancer stem cells in solid tumours: accumulating evidence and unresolved questions. Nature Reviews Cancer 2008;8(10):755-768.
[155] Zhou BBS, Zhang HY, Damelin M, Geles KG, Grindley JC, Dirks PB. Tumour-initiating cells: challenges and opportunities for anticancer drug discovery. Nature Reviews Drug Discovery 2009;8(10):806-823.

[156] Kelly SE, Di Benedetto A, Greco A, Howard CM, Sollars VE, Primerano DA, et al. Rapid selection and proliferation of CD133+ cells from cancer cell lines: chemotherapeutic implications. PLoS One 2010;5(4):e10035.
[157] Smith BH, Gazda LS, Conn BL, Jain K, Asina S, Levine DM, et al. Three-dimensional culture of mouse renal carcinoma cells in agarose macrobeads selects for a subpopulation of cells with cancer stem cell or cancer progenitor properties. Cancer Research 2011;71(3):716-724.
[158] Borovski T, De Sousa EMF, Vermeulen L, Medema JP. Cancer stem cell niche: the place to be. Cancer Research 2011;71(3):634-639.
[159] Fan X, Khaki L, Zhu TS, Soules ME, Talsma CE, Gul N, et al. NOTCH Pathway Blockade Depletes CD133-Positive Glioblastoma Cells and Inhibits Growth of Tumor Neurospheres and Xenografts. Stem Cells 2010;28(1):5-16.
[160] Ricci-Vitiani L, Pallini R, Biffoni M, Todaro M, Invernici G, Cenci T, et al. Tumour vascularization via endothelial differentiation of glioblastoma stem-like cells. Nature 2010;468(7325):824-828.
[161] Singh SK, Hawkins C, Clarke ID, Squire JA, Bayani J, Hide T, et al. Identification of human brain tumour initiating cells. Nature 2004;432(7015):396-401.
[162] Collins AT, Berry PA, Hyde C, Stower MJ, Maitland NJ. Prospective identification of tumorigenic prostate cancer stem cells. Cancer Research 2005;65(23):10946-10951.
[163] Ma S, Chan KW, Hu L, Lee TK, Wo JY, Ng IO, et al. Identification and characterization of tumorigenic liver cancer stem/progenitor cells. Gastroenterology 2007;132(7):2542-2556.
[164] Meyer MJ, Fleming JM, Lin AF, Hussnain SA, Ginsburg E, Vonderhaar BK. CD44posCD49fhiCD133/2hi defines xenograft-initiating cells in estrogen receptor-negative breast cancer. Cancer Research 2010;70(11):4624-4633.
[165] Miki J, Furusato B, Li H, Gu Y, Takahashi H, Egawa S, et al. Identification of putative stem cell markers, CD133 and CXCR4, in hTERT-immortalized primary nonmalignant and malignant tumor-derived human prostate epithelial cell lines and in prostate cancer specimens. Cancer Research 2007;67(7):3153-3161.
[166] Ben-Porath I, Thomson MW, Carey VJ, Ge R, Bell GW, Regev A, et al. An embryonic stem cell-like gene expression signature in poorly differentiated aggressive human tumors. Nature Genetics 2008;40(5):499-507.
[167] Bourguignon LYW, Peyrollier K, Xia WL, Gilad E. Hyaluronan-CD44 interaction activates stem cell marker Nanog, Stat-3-mediated MDR1 gene expression, and ankyrin-regulated multidrug efflux in breast and ovarian tumor cells. Journal of Biological Chemistry 2008;283(25):17635-17651.
[168] Westphal M, Lamszus K. The neurobiology of gliomas: from cell biology to the development of therapeutic approaches. Nature Reviews Neuroscience 2011;12(9):495-508.
[169] Clement V, Sanchez P, de Tribolet N, Radovanovic I, Ruiz i Altaba A. HEDGEHOG-GLI1 signaling regulates human glioma growth, cancer stem cell self-renewal, and tumorigenicity. Current Biology 2007;17(2):165-172.
[170] Ikushima H, Todo T, Ino Y, Takahashi M, Miyazawa K, Miyazono K. Autocrine TGF-beta signaling maintains tumorigenicity of glioma-initiating cells through Sry-related HMG-box factors. Cell Stem Cell 2009;5(5):504-514.

[171] Jin X, Jeon HY, Joo KM, Kim JK, Jin J, Kim SH, et al. Frizzled 4 regulates stemness and invasiveness of migrating glioma cells established by serial intracranial transplantation. Cancer Research 2011;71(8):3066-3075.
[172] Rizzo P, Miao H, D'Souza G, Osipo C, Song LL, Yun J, et al. Cross-talk between notch and the estrogen receptor in breast cancer suggests novel therapeutic approaches. Cancer Research 2008;68(13):5226-5235.
[173] Mani SA, Guo W, Liao MJ, Eaton EN, Ayyanan A, Zhou AY, et al. The epithelial-mesenchymal transition generates cells with properties of stem cells. Cell 2008;133(4):704-715.
[174] Mikheeva S, Mikheev A, Petit A, Beyer R, Oxford R, Khorasani L, et al. TWIST1 promotes invasion through mesenchymal change in human glioblastoma. Molecular Cancer 2010;9(1):194.
[175] Ouyang G, Wang Z, Fang X, Liu J, Yang CJ. Molecular signaling of the epithelial to mesenchymal transition in generating and maintaining cancer stem cells. Cell and Molecular Life Science 2010;67(15):2605-2618.
[176] Misra S, Heldin P, Hascall VC, Karamanos NK, Skandalis SS, Markwald RR, et al. Hyaluronan-CD44 interactions as potential targets for cancer therapy. FEBS Journal 2011;278(9):1429-1443.
[177] Toole BP. Hyaluronan-CD44 Interactions in Cancer: Paradoxes and Possibilities. Clinical Cancer Research 2009;15(24):7462-7468.
[178] Beltran H, Beer TM, Carducci MA, de Bono J, Gleave M, Hussain M, et al. New therapies for castration-resistant prostate cancer: efficacy and safety. European Urology 2011;60(2):279-290.
[179] Feder-Mengus C, Ghosh S, Reschner A, Martin I, Spagnoli GC. New dimensions in tumor immunology: what does 3D culture reveal? Trends in Molecular Medicine 2008;14(8):333-340.
[180] Vesely M, Kershaw M, Schreiber RD, Smyth MJ. Natural innate and adaptive immunity to cancer. Annual Review of Immunology 2011;29:235-271.
[181] Romero P, Cerottini JC, Speiser DE. Monitoring tumor antigen specific T-cell responses in cancer patients and phase I clinical trials of peptide-based vaccination. Cancer Immunology Immunotherapy 2004;53(3):249-255.
[182] Dangles-Marie V, Richon S, El Behi M, Echchakir H, Dorothee G, Thiery J, et al. A Three-Dimensional Tumor Cell Defect in Activating Autologous CTLs Is Associated with Inefficient Antigen Presentation Correlated with Heat Shock Protein-70 Down-Regulation. Cancer Research 2003;63:3682-3687.
[183] Gattinoni L, Powell DJ, Rosenberg SA, Restifo NP. Adoptive immunotherapy for cancer: building on success. Nature Reviews Immunology 2006;6(5):383-393.
[184] Cheever MA, Higano CS. PROVENGE (Sipuleucel-T) in prostate cancer: the first FDA-approved therapeutic cancer vaccine. Clinical Cancer Research 2011;17(11):3520-3526.
[185] Dangles V, Validire P, Wertheimer M, Richon S, Bovin C, Zeliszewski D, et al. Impact of human bladder cancer cell architecture on autologous T-lymphocyte activation. International journal of cancer Journal international du cancer 2002;98(1):51-56.
[186] Feder-Mengus C, Ghosh S, Weber WP, Wyler S, Zajac P, Terracciano L, et al. Multiple mechanisms underlie defective recognition of melanoma cells cultured in three-dimensional

architectures by antigen-specific cytotoxic T lymphocytes. British Journal of Cancer 2007;96(7):1072-1082.
[187] Fischer K, Hoffmann P, Voelkl S, Meidenbauer N, Ammer J, Edinger M, et al. Inhibitory effect of tumor cell-derived lactic acid on human T cells. Blood 2007;109(9):3812-3819.
[188] Ghosh S, Rosenthal R, Zajac P, Weber WP, Oertli D, Heberer M, et al. Culture of Melanoma Cells in 3-Dimensional Architectures Results in Impaired Immunorecognition by Cytotoxic T Lymphocytes Specific for Melan-A/MART-1 Tumor-Associated Antigen. Annals of Surgery 2005;242(6):851-858.
[189] Lin SL, Chang D, Ying SY. Hyaluronan stimulates transformation of androgen-independent prostate cancer. Carcinogenesis 2007;28(2):310-320.
[190] Josefsson A, Adamo H, Hammarsten P, Granfors T, Stattin P, Egevad L, et al. Prostate cancer increases hyaluronan in surrounding nonmalignant stroma, and this response is associated with tumor growth and an unfavorable outcome. American Journal of Pathology 2011;179(4):1961-1968.
[191] Sobel RE, Sadar MD. Cell lines used in prostate cancer research: a compendium of old and new lines--part 1. Journal of Urology 2005;173(2):342-359.
[192] Chignola R, Schenetti A, Andrighetto G, Chiesa E, Foroni R, Sartoris S, et al. Forecasting the growth of multicell tumour spheroids: implications for the dynamic growth of solid tumours. Cell Proliferation 2000;33(4):219-229.
[193] Gorlach A, Herter P, Hentschel H, Frosch PJ, Acker H. Effects of NIFN beta and RIFN gamma on grwoth and morpholog of 2 human-melanoma cell-lines - comparison between 2-dimensional and 3-dimensional culture. International Journal of Cancer 1994;56(2):249-254.
[194] Marusic M, Bajzer Z, Freyer JP, Vukpavlovic S. Analysis of growth of multicellular tumor spheroids by mathematical-models. Cell Prolifation 1994;27(2):73-94.
[195] Lee GY, Kenny PA, Lee EH, Bissell MJ. Three-dimensional culture models of normal and malignant breast epithelial cells. Nature Methods 2007;4(4):359-365.
[196] Weigelin B, Friedl P. A three-dimensional organotypic assay to measure target cell killing by cytotoxic T lymphocytes. Biochemical Pharmacology 2010;80(12):2087-2091.
[197] Zaman MH, Trapani LM, Sieminski AL, Siemeski A, Mackellar D, Gong H, et al. Migration of tumor cells in 3D matrices is governed by matrix stiffness along with cell-matrix adhesion and proteolysis. Proceedings of the National Academy of Sciences of the United States of America 2006;103(29):10889-10894.
[198] Robertson MJ, Ritz J. Biology and Clinical Relevance of Human Natural Killer Cells. Blood 1990;76(12):2421-2438.
[199] Olson B, Mcneel D. CD8+ T cells specific for the androgen receptor are common in patients with prostate cancer and are able to lyse prostate tumor cells. Cancer Immunology Immunotherapy 2011;60(6):781-792.
[200] Wang HM, Yang D, Xu WY, Wang YQ, Ruan ZH, Zhao TT, et al. Tumor-derived soluble MICs impair CD3(+)CD56(+) NKT-like cell cytotoxicity in cancer patients. Immunology Letters 2008;120(1-2):65-71.
[201] Pievani A, Borleri G, Pende D, Moretta L, Rambaldi A, Golay J, et al. Dual-functional capability of CD3(+)CD56(+) CIK cells, a T-cell subset that acquires NK function and retains TCR-mediated specific cytotoxicity. Blood 2011;118(12):3301-3310.

[202] Mendes R, Bromelow KV, Westby M, Galea-Lauri J, Smith IE, O'Brien ME, et al. Flow cytometric visualisation of cytokine production by CD3-CD56+ NK cells and CD3+CD56+ NK-T cells in whole blood. Cytometry 2000;39(1):72-78.
[203] Doherty DG, Norris S, Madrigal-Estebas L, McEntee G, Traynor O, Hegarty JE, et al. The human liver contains multiple populations of NK cells, T cells, and CD3+CD56+ natural T cells with distinct cytotoxic activities and Th1, Th2, and Th0 cytokine secretion patterns. Journal of Immunology 1999;163(4):2314-2321.
[204] Wu JD, Higgins LM, Steinle A, Cosman D, Haugk K, Plymate SR. Prevalent expression of the immunostimulatory MHC class I chain-related molecule is counteracted by shedding in prostate cancer. Journal of Clinical Investigation 2004;114(4):560-568.
[205] Berencsi K, Rani P, Zhang T, Gross L, Mastrangelo M, Meropol NJ, et al. In vitro migration of cytotoxic T lymphocyte derived from a colon carcinoma patient is dependent on CCL2 and CCR2. Journal of Translational Medicine 2011;9(1):33.
[206] Budhu S, Loike JD, Pandolfi A, Han S, Catalano G, Constantinescu A, et al. CD8+ T cell concentration determines their efficiency in killing cognate antigen-expressing syngeneic mammalian cells in vitro and in mouse tissues. Journal of Experimental Medicine 2010;207(1):223-235.
[207] Gulley J, Drake CG. Immunotherapy for prostate cancer: recent advances, lessons learned, and areas for further research. Clinical Cancer Research 2011;17(12):3884-3891.

12. Curriculum Vitae

EDUCATION

University of Washington, Seattle, WA

Ph.D in Materials Science and Engineering, expected 2012

Alfred University, Alfred, NY

Masters of Science in Biomedical Materials Engineering Science, July 2006

Alfred University, Alfred, NY

Bachelors of Science in Ceramic Engineering, May 2004

HONORS AND AWARDS

[1] Outstanding Graduate Student Lecture, Senior Category, Materials Science and Engineering Department, University of Washington, December 2009.
[2] Graduate School Fund for Excellence and Innovation Award, Materials Science and Engineering Department, University of Washington, September 2006.
[3] First place, Graduate Student Presentation, 3rd International Conference on Ethical Issues in Biomedical Engineering, Rochester, NY, June 4 – 6, 2005.
[4] Honorable mention, Glass Manufacturer Industry Council (GMIC) 50x Stronger Glass Contest, June 2005.
[5] Graduate Student Presentation Award, Scientific Conference of The Society for Physical Regulation in Biology and Medicine, South Lake Tahoe, CA, Jan. 2005.

FUNDING

COE Egtvedt Fellowship, 09/2011 – 06/2012

PUBLICATIONS

Research papers

[1] **Stephen J. Florczyk**, Forrest Kievit, Matthew C. Leung, Jennifer D. Wu, John R. Silber, and Miqin Zhang, *Rapid enrichment of the cancer stem cell population in glioblastoma cell lines grown on 3D chitosan-alginate scaffolds*. **In preparation**.

[2] Anna Galperin, Rachael A. Oldinski, **Stephen J. Florczyk**, James D. Bryers, Miqin Zhang, and Buddy D. Ratner, *Integrated bi-layer scaffold for osteochondral tissue engineering*. **In preparation**.

[3] Vy Phan-Lai, Kui Wang, **Stephen J. Florczyk**, Forrest Kievit, Mary L. Disis, and Miqin Zhang, *Combined expression of IFN-g and CCL-21 in a 3-dimensional breast tumor enhances tumor specific T cell activation.* **In preparation**.

[4] Vy Phan-Lai, **Stephen J. Florczyk**, Ekram Gad, Mary L. Disis, and Miqin Zhang, *Suppression of antigen specific T cells by cancer-associated fibroblast in a 3D breast tumor model*. **In preparation**.

[5] **Stephen J. Florczyk**, Matthew Leung, Zhensheng Li, Jerry I. Huang, Richard A. Hopper, and Miqin Zhang, *Evaluation of 3D porous chitosan-alginate scaffolds in rat calvarial defects for bone regeneration applications.* Journal of Biomedical Materials Research, Part A, **submitted**.

[6] **Stephen J. Florczyk**, Matthew Leung, Soumen Jana, Zhensheng Li, Narayan Bhattarai, Jerry I. Huang, Richard A. Hopper, and Miqin Zhang, *Enhanced bone tissue formation by alginate gel-assisted cell seeding in porous ceramic scaffolds*. Journal of Biomedical Materials Research, Part A, **accepted**.

[7] **Stephen J. Florczy**k, Gang Liu, Forrest M. Kievit, Allison M. Lewis, Jennifer D. Wu, and Miqin Zhang, *3D porous chitosan-alginate scaffolds: New matrix for studying prostate cancer cell-lymphocyte interaction in vitro*. Advanced Healthcare Materials, **accepted**.

[8] Soumen Jana, **Stephen J. Florczyk**, Matthew Leung, and Miqin Zhang, *High-strength pristine porous chitosan scaffolds for tissue engineering*. Journal of Materials Chemistry, **22;** 6291-6299 (2012).

[9] **Stephen J. Florczyk**, Dae-Joon Kim, David L. Wood, and Miqin Zhang, *Influence of processing parameters on pore structure of 3D porous chitosan-alginate polyelectrolyte complex scaffolds*. Journal of Biomedical Materials Research, Part A, **98A**(4); 614-620 (2011).

[10] Matthew Leung, Forrest Kievit, **Stephen J. Florczyk**, Omid Veiseh, Jennifer Wu, James Park, and Miqin Zhang, *Chitosan-alginate scaffold culture system for hepatocellular carcinoma increases malignancy and drug resistance*. Pharmaceutical Research, **27**(9); 1939-1948 (2010).

[11] Forrest Kievit, **Stephen J. Florczyk**, Matthew Leung, Omid Veiseh, James Park, Mary Disis, and Miqin Zhang, *Chitosan-alginate 3D scaffolds as a mimic of the glioma tumor microenvironment*. Biomaterials, **31**(22); 5903-5910 (2010).

[12] **Stephen J. Florczyk** and Subrata Saha, *Manufacture of nanoparticles from bone: a preliminary study*. J. Long Term Eff Med Implants, **19**(4); 323-9 (2009).

[13] **Stephen J. Florczyk** and Subrata Saha, *Ethical Issues in Nanotechnology*, J. Long Term Eff Med Implants, **17**(3); 271-280 (2007).

Book Chapters

[1] **Stephen J. Florczyk** and Subrata Saha, Ethical Issues in Biomedical Research, in *Wiley Encyclopaedia of Biomedical Engineering*, Ed. M. Akay, John Wiley & Sons, Inc., Hoboken, NJ, (2006).

Presentations

[1] **Florczyk, SJ,** Leung, M, Jana, S, Li, Z, Bhattarai, N, Huang, JI, Hopper, RA, and Zhang, M. Enhanced bone tissue formation by alginate gel-assisted cell seeding in porous ceramic scaffolds, Podium and Poster presentation at the Society for Biomaterials Annual Meeting, April 2010.
[2] **Florczyk**, **SJ**, Leung, M, Li, Z, Huang, JI, Hopper, RA, and Zhang, M. Evaluation of 3D porous chitosan-alginate scaffolds in rat calvarial defects for bone regeneration applications, Podium presentation at Fellow's Research Day, April 22, 2009.
[3] **Florczyk, S.J.** and Flick, L.M., Exploring the crosstalk between p38 MAPK and canonical Wnt signaling pathways, Poster Presentation at American Association of Immunologists Meeting, Miami FL, May 18-22, 2007.
[4] **Florczyk, S.J.** and Hall, M.M., Nanoparticle Hydroxyapatite Derived from Bovine Bone as a Remediation Agent, Poster Presentation at Material Research Society Fall 2005 Meeting, Boston, MA, November 28 – December 2, 2005.
[5] **Florczyk, S.J.** and Saha, S., Ethical Issues in Nanotechnology, Podium presentation at Third International Conference on Ethical Issues in Biomedical Engineering, Rochester, NY, June 4-6, 2005.
[6] **Florczyk, S.J.** and Saha, S., Manufacture of Nanoparticles from Bone, Poster Presentation at Orthopaedic Research Society 51st Annual Meeting, Washington, D.C., February 2005.
[7] **Florczyk, S.J.** and Saha, S., Manufacture of Nanoparticles from Bone, Podium presentation at 23rd Scientific Conference of The Society for Physical Regulation in Biology and Medicine, South Lake Tahoe, CA, Jan. 2005.
[8] **Florczyk, S.J.** and Saha, S., Manufacture of Nanoparticles from Bone, Poster presentation at Biomedical Engineering with Glasses and Ceramics, The Hulbert Conference, Buffalo, NY, August 2004.
[9] **Florczyk, S.J.** and Saha, S., Manufacture of Nanoparticles from Bone, Podium presentation at Bioengineering in New York Conference, Alfred, NY, October 31 – November 2, 2003.